International Journal on Communications Antenna and Propagation (IRECAP)

Contents

Computation of Near-Field and Far-Field Radiation Characteristics of Acoustic Transducers for Underwater Acoustic Imaging by Praveen L. S., Govind R. Kadambi, S. Malathi, Preetham Shankapal	145
Dual-Band Circularly Polarized Millimeter-Wave Antenna for 5G-WiGig Applications by Nada Abd El-Latif, Hany M. Zamel, Ahmed M. Attiya, Amr Al-Awamery	154
Visibility Modeling and Prediction for Free Space Optical Communication Systems for South Africa by Olabamidele O. Kolawole, Modisa Mosalaosi, Thomas J. O. Afullo	161
Modeling Environmental Effects on Electromagnetic Signal Propagation Using Multi-Layer Perceptron Artificial Neural Network by Virginia C. Ebhota, Viranjay M. Srivastava	175
Reduction of Mutual Coupling in Compact Antenna Array Using Meander Line Slot EBG Structure by Mahesh Kadu, Neela Rayavarapu	183
Network Lifetime Evaluation in Heterogeneous WSN with Different Node Placement Distributions by Yousef Jaradat, Mohammad Masoud, Dema Zeidan	192
A Comparative Study of Wireless Sensor Network Using Cooperative Protocol by Raed S. M. Daraghma	199
Detecting the Online Shopping Factors Using the Arab Tweets on Media Technology by M. B. Yassein, O. Alomari	206



International Journal on Communications Antenna and Propagation (IRECAP)

Editor-In-Chief:

Masood Ur Rehman

James Watt School of Engineering, University of Glasgow, 205, 76 Oakfield Avenue, Glasgow G12 8QQ

Editorial Board:

Qammer H. Abbasi	(U.K.)	Rongxing Lu	(Canada)
Kamran Arshad	(E.A.U.)	Marta Martínez Vázquez	(Germany)
Nauman Aslam	(Canada)	Mustafa M. Matalgah	(U.S.A.)
C. Faouzi Bader	(France)	Natarajan Meghanatan	(U.S.A.)
Marcus Brunner	(Germany)	Mittal Neeraj	(U.S.A.)
Shu-Ching Chen	(U.S.A.)	Jose Neuman Souza	(Brazil)
Zhizhang (David) Chen	(Canada)	Mairtin O'Droma	(Ireland)
José A. Encinar	(Spain)	Mauro Parise	(Italy)
Adolf Finger	(Germany)	Hung-Min Sun	(Taiwan)
Ismail Khalil	(Austria)	Mehmet Ulema	(U.S.A.)
Abdelmajid Khelil	(Germany)	Luis Javier García Villalba	(Spain)
Shiban Koul	(India)	Kiyotoshi Yasumoto	(Japan)
Polychronis Koutsakis	(Greece)	Chen Zhi Ning	(Singapore)

The International Journal on Communications Antenna and Propagation (IRECAP) is a publication of the Praise Worthy Prize S.r.l..

The Review is published bimonthly, appearing on the last day of February, April, June, August, October, December.

Published and Printed in Italy by Praise Worthy Prize S.r.l., Naples, June 30, 2020.

Copyright © 2020 Praise Worthy Prize S.r.l. - All rights reserved.

This journal and the individual contributions contained in it are protected under copyright by **Praise Worthy Prize S.r.l.** and the following terms and conditions apply to their use:

Single photocopies of single articles may be made for personal use as allowed by national copyright laws.

Permission of the Publisher and payment of a fee is required for all other photocopying, including multiple or systematic copying for advertising or promotional purposes, resale and all forms of document delivery. Permission may be sought directly from **Praise Worthy Prize S.r.l.** at the e-mail address:

administration@praiseworthyprize.com

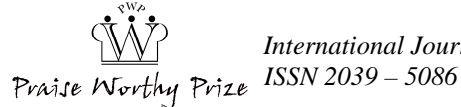
Permission of the Publisher is required to store or use electronically any material contained in this journal, including any article or part of an article. Except as outlined above, no part of this publication may be reproduced, stored in a retrieval system or transmitted in any form or by any means, electronic, mechanical, photocopying, recording or otherwise, without prior written permission of the Publisher. E-mail address permission request:

administration@praiseworthyprize.com

Responsibility for the contents rests upon the authors and not upon the Praise Worthy Prize S.r.l..

Statement and opinions expressed in the articles and communications are those of the individual contributors and not the statements and opinions of **Praise Worthy Prize S.r.l.** assumes no responsibility or liability for any damage or injury to persons or property arising out of the use of any materials, instructions, methods or ideas contained herein.

Praise Worthy Prize S.r.l. expressly disclaims any implied warranties of merchantability or fitness for a particular purpose. If expert assistance is required, the service of a competent professional person should be sought.



Computation of Near-Field and Far-Field Radiation Characteristics of Acoustic Transducers for Underwater Acoustic Imaging

Praveen L. S., Govind R. Kadambi, S. Malathi, Preetham Shankapal

Abstract – This paper proposes a novel approach through analytical formulation for the determination of the radiation pattern of acoustic transducers at any arbitrary observation distance which covers both the near-field as well as the far-field. The proposed near-field/far-field analysis is generic and can be applied to a wide variety of acoustic apertures. The radiation pattern of the acoustic transducer at any arbitrary point of observation (both the near-field and far-field) is obtained by the vector summation of the fields radiated by the array of point sources located on the aperture of the acoustic transducer. The validity and novelty of the proposed approach have been proved by treating the far-field as a special case of near-field with the relevant distance criterion. The simulation studies show that near-field radiation patterns of the acoustic transducer exhibit changes in the profile of the amplitude patterns when the distance of observation is varied. The formation of a well-defined main beam of the radiation pattern occurs only after a distance of separation of about $R=D^2/\lambda$ from the radiating aperture. The presented analytical formulation has an attribute of wider generality because of its applicability to a variety of geometrical configurations of the aperture of an acoustic transducer. Copyright © 2020 Praise Worthy Prize S.r.l. - All rights reserved.

Keywords: Aperture, Far Field, Near Field, Point Source, Radiation Pattern, Underwater Acoustic Imaging

Nomenclature

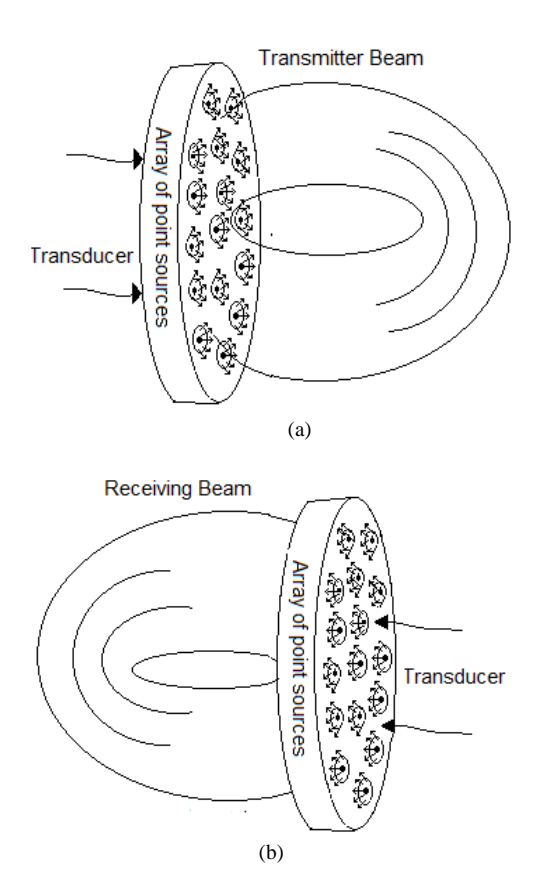
FF Far-field **ISAS** Inverse Synthetic Aperture Sonar NF Near field SAS Synthetic Aperture Sonar **SONAR** Sound Navigation and Ranging **UAI** Underwater Acoustic Imaging λ Wavelength θ Elevation angle Azimuth angle φ Radius of the circular aperture aDiameter of the circular aperture d Largest dimension of a transducer DWavenumber k $L \times W$ Length and Width of rectangular aperture Pressure field distribution on aperture P_o Pressure field distribution on point source P_f Pressure field at the observation point Pressure field at the point source Radius of point sources Distance between the observation point to the point sources R Range, Distance between the observation point and center of the transducer x, y and z coordinates of observation (x_f, y_f, z_f) x, y and z coordinates of point sources (x_{sm},y_{sm},z_{sm})

I. Introduction

Underwater Acoustic Imaging (UAI) is the study of the propagation of sound waves in water. It provides underwater observation and inspection capabilities wherever optical systems cannot. In UAI, Sound Navigation and Ranging (SONAR) is used to detect and classify objects in underwater using acoustic waves. UAI is a cross-disciplinary domain that involves acoustic transducer, waveform design, beamforming, motion compensation, and image processing among others. UAI system is similar to other forms of acoustic imaging such as medical and non-destructive testing where it provides two-dimensional images of objects using sound waves. UAI is used for various applications like navigation, surveillance, reconnaissance, and ranging. Some of the commercial applications of UAI comprise planning communication links for discovering underwater mining resources. UAI finds utility in military applications such as locating submarines and mines. Modern applications of UAI involve developing autonomous underwater vehicles equipped with acoustic imaging devices to monitor and explore the seafloor. The operating frequency of underwater acoustics ranges from 10 Hz to 1 MHz [1]. Lower frequencies (<1 MHz) offer a longer range with poor resolution while higher frequencies facilitate better resolution but a shorter range.

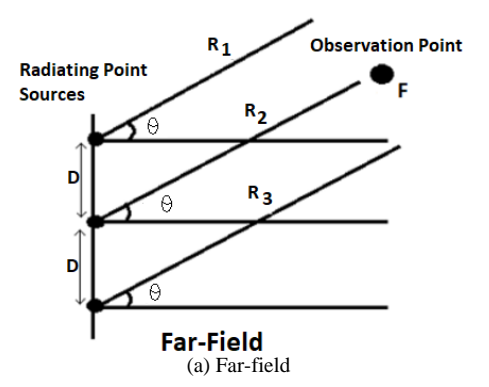
Hence for UAI systems, the operating frequency will be typically in the range of 10 kHz to 300 kHz with a

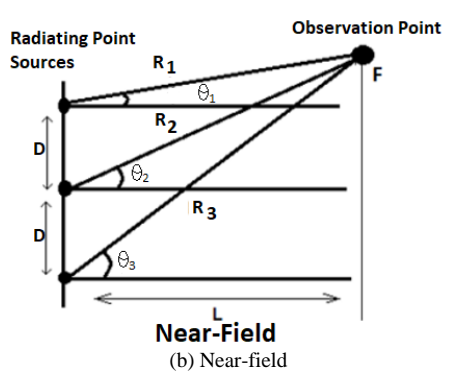
bandwidth of 30 kHz and wavelength 14.80 cm to 0.49 cm [2]. SONAR is used for exploring and mapping the underwater scenario because sound wave travels long distances in the water compared to the light waves. There are many efficient approaches used in UAI like the Synthetic Aperture Sonar (SAS) and Inverse Synthetic Aperture Sonar (ISAS) [3], [4]. But they both have their own merits and demerits in computing efficiency, hardware requirement, and development of highresolution images. SAS suffers from a slow mapping rate. The difficulty in maintaining phase coherence throughout the entire synthesized aperture results in significant image degradation [5]. Both SAS and ISAS imaging require relative motion between the target and the radiating system. Without the above mentioned relative motion, the image does not form [6]. Both SAS and ISAS methods use different beamforming techniques to illuminate the targets in underwater using the acoustic transceiver. Beamforming is a signal processing technology used to control the directionality of signal transmission (or) reception. Beamforming has been in use for many years in the field of SONARs in which both amplitude and phase shift (weights) at each acoustic transducer are varied to control the directionality of the transmitted or received beam as shown in Figs. 1. In farfield, the acoustic rays incident on different point sources located on the aperture of the acoustic transducer are parallel (Fig. 2(a)). Whereas in the near-field, rays impinging on the acoustic aperture are not assumed to be parallel.



Figs. 1. The Array of Point Sources on Acoustic Transducer [7]

Copyright © 2020 Praise Worthy Prize S.r.l. - All rights reserved





Figs. 2. Pictorial Representation of Far-Field and Near-Field Beamforming [8]

In the near-field, the distance between the source of the acoustic field and the receiver is small (Fig. 2(b)) [8].

Well established far-field methods for measuring radiation patterns of an acoustic transducer in the underwater scenario cannot be used in many cases due to the large aperture size of the acoustic transducers. The radiating far-field distance may be too long (or) impractical to move the acoustic transducer from its operating environment to the desired range. Radiating acoustic power (pressure) decreases as the square of the distance from the transmitter resulting in poor image quality.

For a given observation point, the near field beamforming array exhibits differing radiation patterns in terms of both amplitude and phase. Therefore, the computation of near-field radiation patterns of the acoustic transducer which forms an element of a beamforming array becomes an important step in the simulation of near-field beamforming. Selfridge (1980) [9] discusses the analysis of the far-field radiation pattern of the narrow-strip acoustic transducer for underwater imaging. Rongrong (2014) [10] illustrates measurement of far-field radiation patterns for dipole acoustic transducers. Hayden (2003) [11] describes the mathematical modeling of the SAS system, offering improved Fourier based image reconstruction by analyzing the far-field beamformer for seafloor detection.

Stepanishen (2005) [12] has presented a computation method for the far-field radiation pattern from cylindrical pistons.

The author has also described a method for computing the interacting forces and mutual radiation impedance.

From the succinct literature review cited above, it is evident that literature is abundant in the far-field techniques of UAI. However, the reported research on near-field analysis of UAI appears to be rather limited in the open literature.

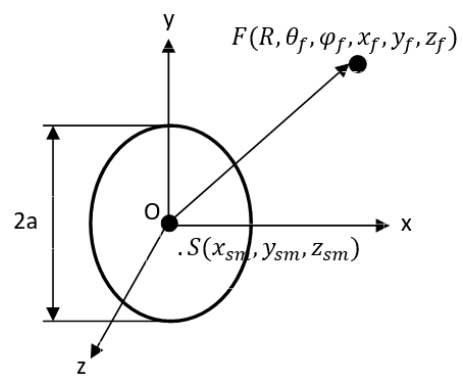
From the literature, it is observed that for the far-field radiation pattern of the acoustic transducer, each of the analysis had been specifically developed for the specific geometric configuration of an acoustic aperture. Also, none of the existing formulations of far-field can be extended to treat near-field analysis or to other geometric configurations of acoustic aperture.

On the contrary, this paper proposes a novel technique which is valid for computing the radiation pattern at any arbitrary distance (near-field and far-field) from the transducer. Additionally, the presented analytical formulation has an attribute of wider generality given its applicability to a variety of geometrical configurations of the aperture of the acoustic transducer.

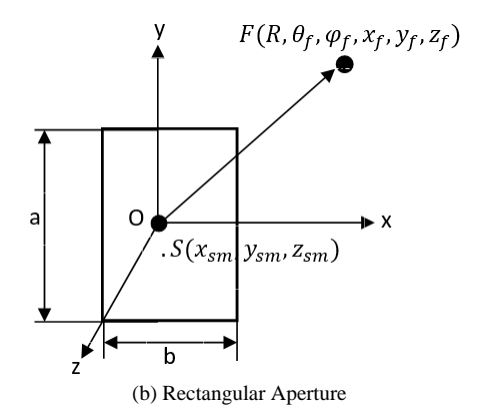
The paper is organized as follows. Section II presents the generalized procedure to compute the near-field radiation pattern of the acoustic transducer using mathematical formulations. This section also discusses the pressure field distribution on a point source of the acoustic transducer. Section III presents the results of near-field and far-field radiation patterns of the acoustic transducer for both circular and rectangular apertures using the formulation presented in this paper. Finally, Section IV presents the conclusions and avenues for future research as a continuation of the main theme of this paper.

II. Analytical Formulation for Near Field Radiation Pattern of Acoustic Transducer

This section presents a generalized procedure for computing the near-field radiation pattern of an acoustic transducer. In the proposed method of determination of the near-field, the radiating aperture of an acoustic transducer is replaced by an array of point sources whose pressure strength is determined by the pressure distribution at the respective locations of point sources on the acoustic transducer [13]. The proposed method which is versatile and more generic applies to any geometric shape of the aperture of the transducer. This paper considers the circular and rectangular apertures for the analysis of near-field radiation pattern of acoustic transducers. The circular and rectangular apertures associated with Cartesian coordinate system for the analysis of the near-field radiation pattern are shown in Figs. 3. The radiating aperture of the circular and rectangular acoustic transducer is assumed to coincide with Z=0 plane and the observation point of interest F is in the near-field range from the transducer. As shown in Fig. 3(a), the diameter of a circular aperture is d=2awhere a is radius of an aperture. For the rectangular aperture, the Length (L=a) and the Width (W=b) of the aperture are as shown in Fig. 3(b).



(a) Circular Aperture



Figs. 3. Coordinate System for Near-Field Analysis with Aperture in Z=0 Plane

The criterion for the definition of far-field distance R is $R \ge 2D^2/\lambda$, where D is the largest dimension of the transducer aperture and " λ " is the wavelength. A distance of observation with R, $R < 2D^2/\lambda$, is termed as near-field. The near-field, in turn is divided into two more regions as stated in [14]:

- a. Reactive near-field: $R < 0.62\sqrt{D^3/\lambda}$;
- b. Radiating near-field: $0.62\sqrt{D^3/\lambda} < R < 2D^2/\lambda$.

The computation of the near-field radiation pattern of an acoustic transducer is carried out satisfying the criterion $0.62\sqrt{D^3/\lambda} < R < 2D^2/\lambda$. In the far-field region $(R \ge 2D^2/\lambda)$, the normalized radiation pattern is independent of the observation distance from the acoustic transducer [15]. This paper proposes a generic method that is valid for the computation of the radiation pattern of the acoustic transducer irrespective of whether the observation point is in the near-field or far-field region.

II.1. Pressure Distribution at Various Point Sources on Acoustic Aperture

In the analysis proposed in this paper, the radiating surface (aperture) of the acoustic transducer is considered to be comprised of several infinitesimally small point sources (elements). Each of the point sources has an infinitesimally small area *ds* as shown in Fig. 4. Each point source with a diameter much smaller than the wavelength of operation transmits spherical waves in all directions [16].

 $\textit{Copyright} © \textit{2020 Praise Worthy Prize S.r.l.} \cdot \textit{All rights reserved}$

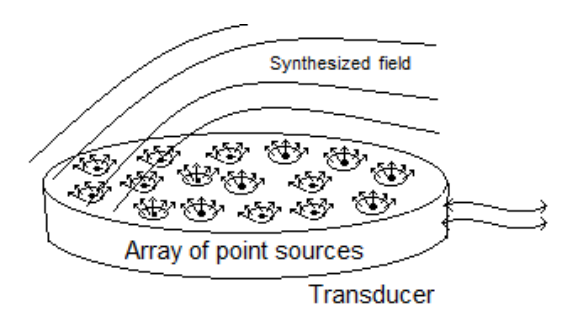


Fig. 4. Field Distribution from an Array of Point Sources

Wave propagation from a point source is illustrated in Fig. 5, where r_0 is the radius of the simple source; P_0 denotes the pressure at the surface. The pressure at a radial distance r is denoted as P_r .

The point source emits spherical waves of acoustic radiation in an ideal uniform medium. In a point source, the pulsating sphere diameter is smaller than the wavelength of the radiated waves. The radiating waves originating from a point source spread uniformly over a spherical surface with the source located at the center of the sphere. The pressure P_r over the spherical surface is inversely proportional to radius r and hence the amplitude (of pressure) of the waves decreases as their distance from the point source increases [13]. Hence, the far-field radiation pattern of a point source is given by:

$$P_m(r_m) = A_m \frac{e^{-jk_m r_m}}{r_m} ds \tag{1}$$

where $P_m(r_m)$ is the corresponding amplitude of pressure of point source at a distance r_m from the source.

The constant A_m defines the reference amplitude at the reference distance r_m ; k_m is the wavenumber and $j = \sqrt{(-1)}$ [17]. The velocity of the acoustic source V_m at a point F due to the m^{th} point source is illustrated in Figs. 6. The characteristics of the radiation pattern of acoustic aperture are determined significantly by the size and shape of the acoustic transducer (radiating element), the distance of the radiating element to the observation point, and the frequency of operation.

The most commonly used radiating aperture in acoustic engineering is either rectangular or circular. The following section discusses the computation of the radiation pattern of acoustic transducers with circular and rectangular apertures.

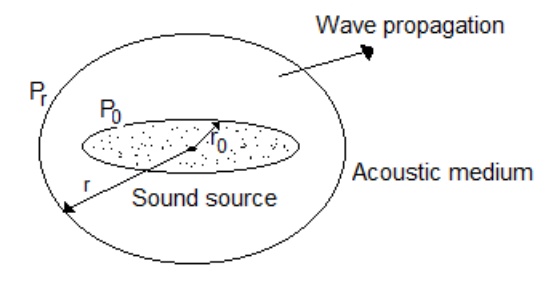
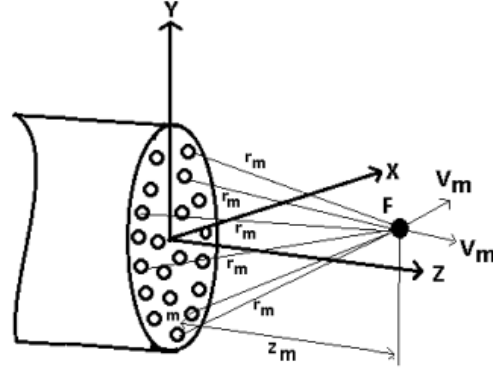
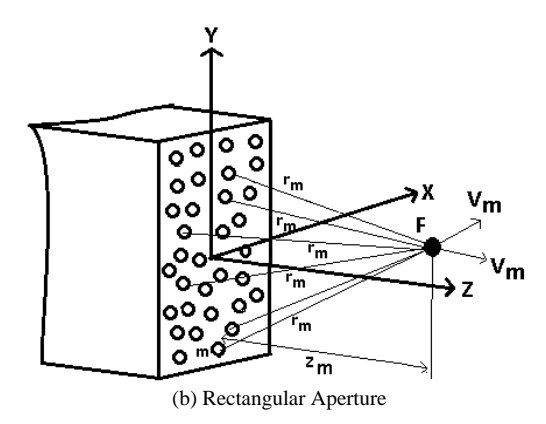


Fig. 5. A Point Source Transmitting a Spherical Wave with Reference Pressure P_0 at a Reference Distance r_0



(a) Circular Aperture



Figs. 6. Field (Pressure) Distribution at Observation Point F due to Radiation from \mathbf{m}^{th} Point Source with Velocity V_m

II.2. Computation of Near Field Radiation Pattern of Circular Acoustic Aperture

For the computation of radiation pattern, the Cartesian coordinates of point sources on circular aperture and the observation point F located at a distance R from the center of the circular aperture are shown in Fig. 7. The circular radiating aperture consists of a number of point sources with an infinitesimally small area ds at distance ρ from the center of the aperture. Each point source on the acoustic aperture generates spherical waves in all directions.

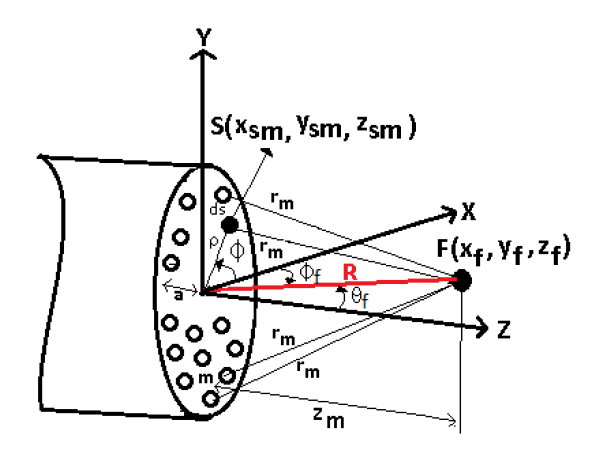


Fig. 7. Coordinate System of Circular Aperture for Analysis of Radiation Pattern

 $Copyright © 2020 \ Praise \ Worthy \ Prize \ S.r.l. \ - All \ rights \ reserved$

The pressure field distribution $P_f(x_f, y_f, z_f)$ at an observation point $F(x_f, y_f, z_f)$ due to radiation from "m" point sources located at points $S(x_{sm}, y_{sm}, z_{sm})$ on circular aperture is given by:

$$P_f(x_f, y_f, z_f) = \iint_{surface} P_m(x_{sm}, y_{sm}, z_{sm}) ds \qquad (2-a)$$

$$P_{f}(x_{f}, y_{f}, z_{f}) = A_{0} \int_{\rho=0}^{a} \int_{\phi=0}^{2\pi} \frac{e^{-jkr_{m}}}{r_{m}} \rho \ d\rho \ d\phi \qquad (2-b)$$

In Eq. (2-a), " P_m " indicates the pressure field of a point source on the acoustic aperture. In Eq. (2-b), a is the radius of a circular aperture, r_m is the distance between the location of m^{th} point source S' on the aperture and the observation point F and k is the wavenumber [18]:

$$r_m = \sqrt{(x_f - x_{sm})^2 + (y_f - y_{sm})^2 + (z_f - z_{sm})^2}$$
 (3)

 (x_{sm}, y_{sm}, z_{sm}) and (x_f, y_f, z_f) denote the coordinates of a point source on the acoustic aperture and the observation point respectively:

$$x_f = R \sin \theta_f \cos \varphi_f \tag{4}$$

$$y_f = R \sin \theta_f \sin \varphi_f \tag{5}$$

$$z_f = R\cos\theta_f \tag{6}$$

where θ_f =-90° to +90°, φ_f =0 to 360°, R is the distance between the center of acoustic aperture O(0,0,0) and the observation (field) point $F(x_6y_6z_f)$.

The locations of point sources on the circular aperture are given by:

$$x_{sm} = \rho \cos \varphi \tag{7}$$

$$y_{sm} = \rho \sin \varphi \tag{8}$$

$$z_{sm} = 0 (9)$$

where $\rho=0$ to a, $\varphi=0$ to 360° .

II.3. Computation of Near Field Radiation Pattern of Rectangular Acoustic Aperture

Although the circular radiating aperture is a classic example of an acoustic transducer, a rectangular aperture shown in Fig. 8 is also the most widely used acoustic radiating aperture element. As in the case with the circular radiating aperture, the rectangular aperture is also considered to be consisting of point sources with an infinitesimally small area "ds" at distance " ρ " from the center of the rectangular aperture.

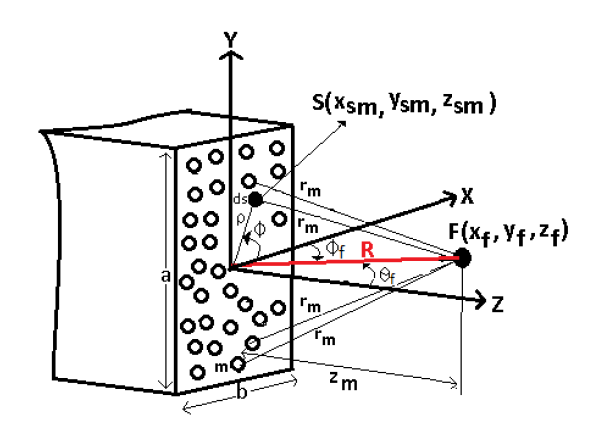


Fig. 8. Coordinate System of Rectangular Aperture for Analysis of Radiation Pattern

The expression for the radiation pattern of an acoustic transducer with a rectangular aperture is given by:

$$P_f(x_f, y_f, z_f) = \iint_{surface} P_m(x_{sm}, y_{sm}, z_{sm}) ds \quad (10-a)$$

$$P_f(x_f, y_f, z_f) = A_0 \int_{x=-a/2}^{a/2} \int_{y=-b/2}^{b/2} \frac{e^{-jkr_m}}{r_m} dx dy$$
 (10-b)

In Eq. (10-a), P_m indicates the pressure field of a point source on the rectangular aperture. In Eq. (10-b), a is the length and b is the width of the rectangular aperture, r_m is the distance between the location of m^t point source S on the acoustic aperture and the observation point F. k is the wavenumber.

The observation point F is in the near-field range of the transducer. It is relevant to emphasize that the formulation for the radiation pattern of an acoustic transducer presented in this paper is uniformly valid irrespective of whether the observation point is in the near-field or far-field region.

III. Results and Discussion

This section presents a discussion on the simulation results of radiation patterns of circular and rectangular acoustic apertures obtained through the formulations presented in the earlier sections.

The results include the surface contour plots of pressure distribution over the radiating aperture, near and far-field radiation patterns of both the circular and rectangular apertures. The discussion in this section also covers the validation studies of far-field results obtained through the proposed near-field analysis of acoustic transducer.

For the simulation, the chosen operating frequency for both the apertures is 30 kHz which is well within the SONAR operating frequency range of 10 kHz to 300 kHz [19]

For an acoustic transducer of circular aperture with a

Copyright © 2020 Praise Worthy Prize S.r.l. - All rights reserved

radius of (a=2 cm; d=4 cm), at a frequency of 30 kHz (λ =4.9 cm, c=1480 m/s), the near-field distance has to be less than 2D²/ λ (<6.54 cm).

When the radial distance of observation R is $>2D^2/\lambda$, it satisfies the far-field distance criterion. For an acoustic transducer with a rectangular aperture, length a=2.89 cm and width b=4.34 cm. 36 point sources along the radial (ρ) and 36 point sources along with azimuthal (φ) directions are considered on the radiating circular aperture. Similarly, the number of point sources on the radiating rectangular aperture is 36×36 implying 36 point sources along the X-axis and 36 point sources along the Y-axis of rectangular apertures. The pressure field distributions over circular and rectangular apertures are shown in Figs. 9(a) and (b) respectively through contour image.

Figs. 10 illustrate the comparison of the results obtained from the far-field analysis of existing methods and the far-field as a special case of the near-field analysis proposed in this paper. Fig. 10(a) shows the comparison of the far-field radiation pattern of the circular aperture obtained from the proposed analysis and the results of the method proposed in [7].

Similarly, Fig. 10(b) shows the comparison of results of the far-field radiation pattern of acoustic rectangular aperture obtained through the proposed analysis and the results through the analysis in [20]. The results of Figs. 10 show an excellent correlation between the proposed near-field/far-field method and existing far-field techniques.

The results of Figs. 10 also show that the main beam of the circular and rectangular apertures is almost identical.

This is because the area of circular and rectangular apertures is chosen to be the same for the simulation studies.

It is pertinent to emphasize that the formulations presented in [7] and [20] are applicable only for far-field analysis and are not valid for near-field analysis. After validating the simulated results on far-field radiation patterns of circular and rectangular apertures, the

computations of near-field radiation (amplitude and phase) patterns were carried out using the proposed analysis with the radial observation distance of $R=D^2/\lambda$ (where, R is the range, D is the largest dimension of the transducer and λ is the wavelength of acoustic waves) at a frequency of 30 kHz.

Figs. 11(a) and (b) show the comparison of the amplitude patterns of a circular and rectangular aperture at $R=D^2/\lambda$ (Near-Field) and $R=2D^2/\lambda$ (Far-Field). Figs. 12(a) and (b) show the phase patterns of circular aperture at $R=D^2/\lambda$ and $R=2D^2/\lambda$.

The analysis of near field radiation patterns was carried out with an incremental increase in the radial distance of observation. Simulations were carried out to obtain the near-field patterns of circular and rectangular apertures at distances of $0.2D^2/\lambda$, $0.4D^2/\lambda$, $0.6D^2/\lambda$, $0.8D^2/\lambda$, $1.2D^2/\lambda$, $1.6D^2/\lambda$, $2D^2/\lambda$, $4D^2/\lambda$.

Fig. 13 shows the radiation patterns of circular aperture for the above-mentioned radial distances of observation.

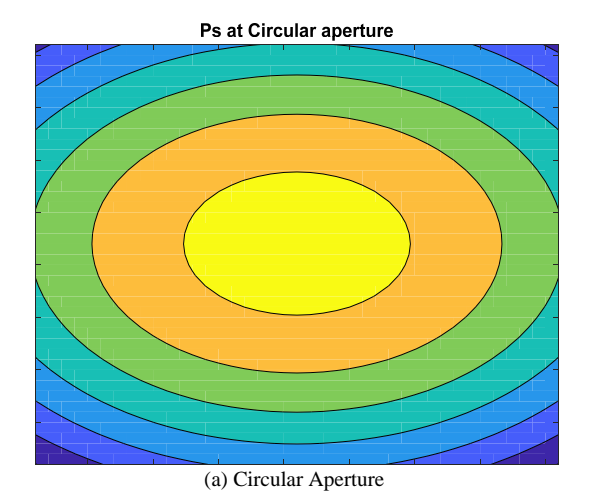
The analogous results for a rectangular aperture are shown in Fig. 14.

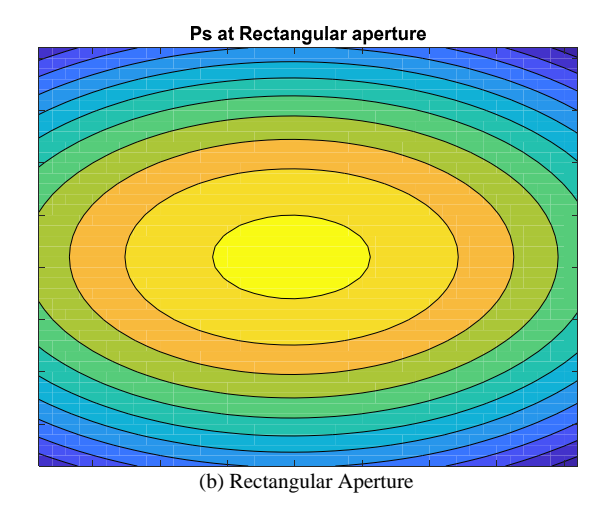
Simulation results of Figs. 13 and 14 indicate that, when the distance between the observation point and the aperture is small, no formation or no clear formation of the main beam is evident. As the distance between the aperture and observation point increases, the progression in the formation of the main beam is seen. Figs. 15(a) and (b) illustrate the radiation patterns of circular and rectangular aperture for different frequencies from low to high (10 kHz to 300 kHz) with $R=D^2/\lambda$.

In the results of Figs. 15, the absolute value of R varies since λ also changes with frequency.

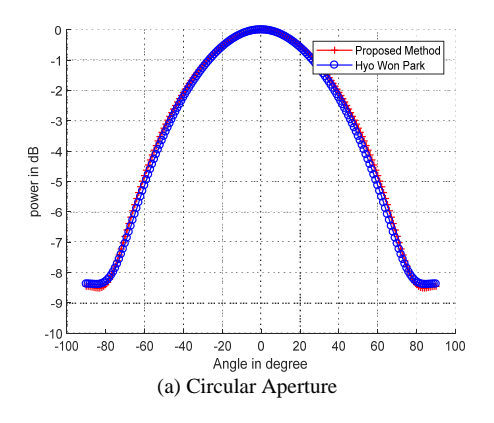
Figs. 16(a) and (b) illustrate the radiation patterns of circular and rectangular apertures for different frequencies from low to high (10 kHz to 300 kHz) when range R is fixed to near-field region $(R=D^2/\lambda)$ at frequency f=30 kHz; R=3.24 cm.

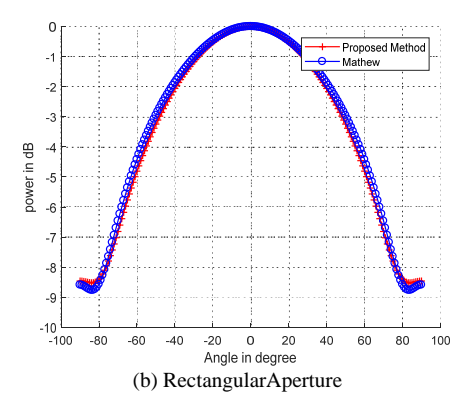
The results of Figs. 16(a) and (b) reveal that as the frequency increases, the profile of the radiation patterns shows a lot more rapid variations (fluctuations).



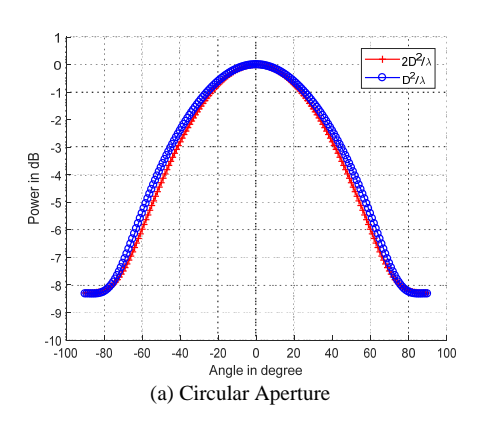


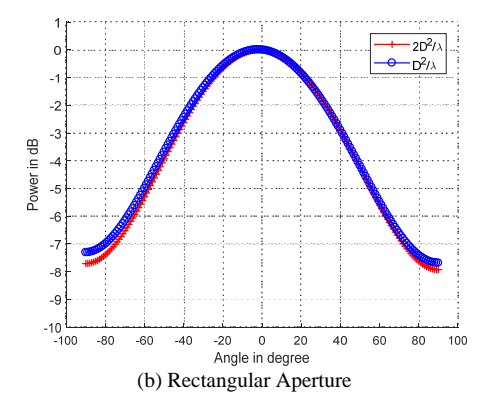
Figs. 9. Pressure Distribution over Aperture of Acoustic Transducer



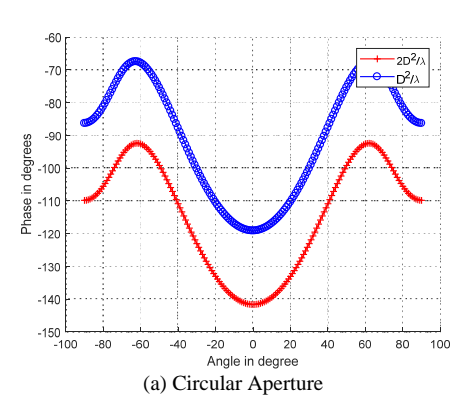


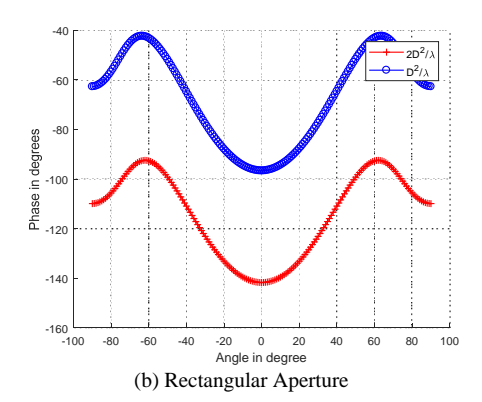
Figs. 10. Comparison of Far-Field Radiation Patterns of Acoustic Transducers



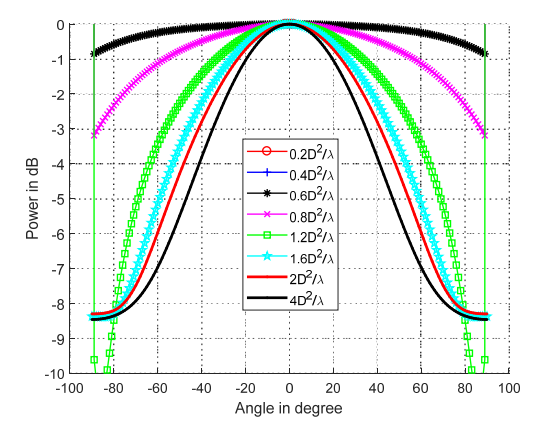


Figs. 11. Comparison of Amplitude Radiation Patterns of Acoustic Transducer at $R=D^2/\lambda(NF)$ and $R=2D^2/\lambda(FF)$





Figs. 12. Comparison of Phase Radiation Patterns of the Acoustic Transducer at $R=D^2/\lambda$ (NF) and $R=2D^2/\lambda$ (FF)



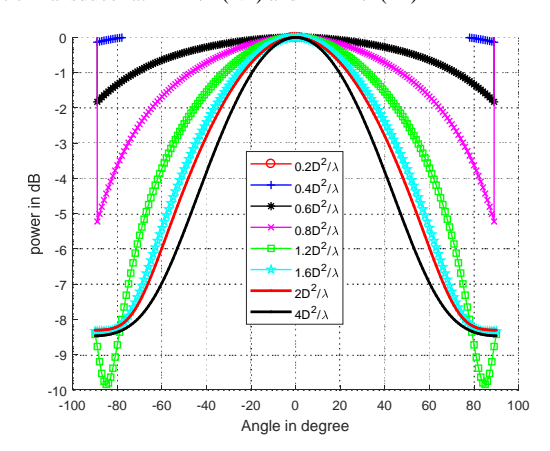
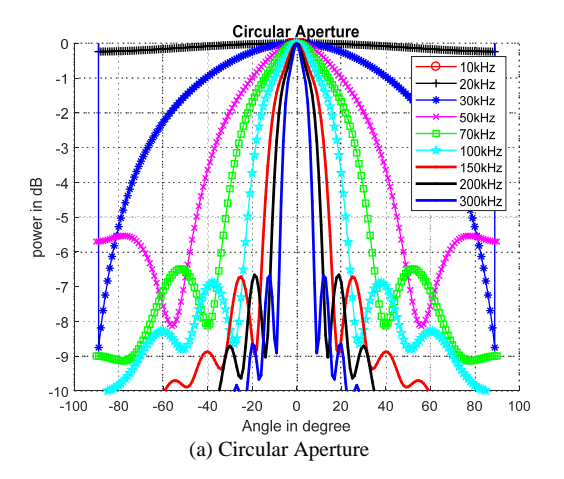
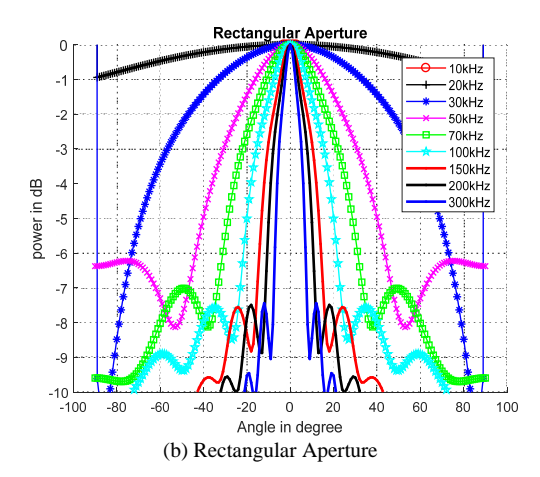


Fig. 13. Radiation Pattern of Circular Aperture for Different Radial Distances of Observation

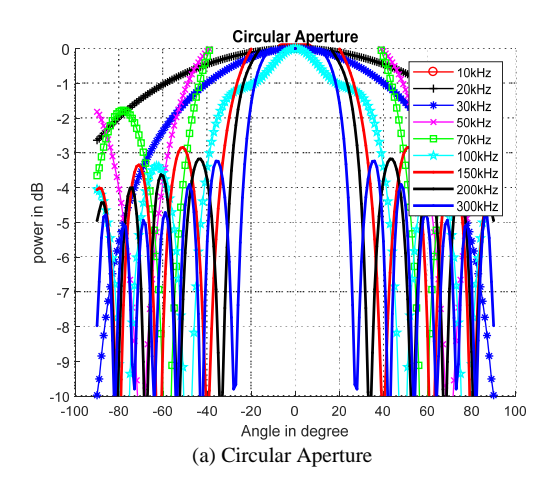
Fig. 14. Radiation Pattern of Rectangular Aperture for Different Radial Distances of Observation

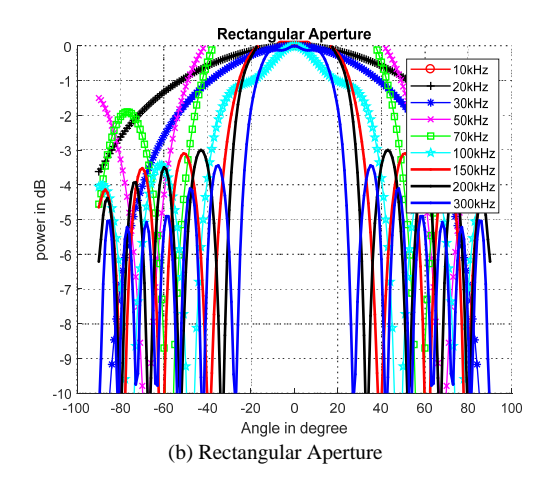
Copyright © 2020 Praise Worthy Prize S.r.l. - All rights reserved





Figs. 15. Comparison of Radiation Pattern of Acoustic Transducer for Different Frequencies (10 kHz to 300 kHz) when range " $R = D^2/\lambda$ " is Varying





Figs. 16. Comparison of Radiation Pattern of Acoustic Transducer for Different Frequencies (10 kHz to 300 kHz) when Range "R = 3.24cm" is Fixed

IV. Conclusion

This section summarizes the derived conclusions which are based on the analysis and simulation results presented in this paper. The proposed formulation for computing the radiation pattern of the acoustic transducer is valid for both the near-field and far-field regions. The proposed near-field analysis is valid for a wide variety of aperture geometries of acoustic transducer. The radiation pattern of the acoustic transducer at any arbitrary point of observation (both the near-field and far-field) is obtained by the vector summation of the fields radiated by the array of point sources located on the aperture of the acoustic transducer. By treating the fa-field as a special case of near-field with the appropriate distance criterion, the validity of the proposed approach for computing the radiation pattern of the acoustic transducer is substantiated by correlating the obtained far-field results with those obtained through existing far-field techniques.

Unlike the proposed analysis, the other existing techniques [7] and [20] are meant only for the far-field radiation pattern and they cannot be applied to the near-field scenario. The simulation studies show that the near-field radiation patterns of the acoustic transducer exhibit changes in the profile of the amplitude patterns when the distance of observation is varied. The formation of the

well-defined main beam is evident only when R, the distance of observation from the radiating aperture is \geq D^2/λ . The presented analytical formulation has an attribute of wider generality given its applicability to a variety of geometric configurations of the aperture of the acoustic transducer. The analytical formulation for the radiation pattern of the acoustic transducer which is valid for an arbitrary distance of observation will be of significant relevance to near-field beamforming array, which is a topic of current interest of the authors. The proposed formulation for the near field radiation pattern of acoustic transducer involves a two-dimensional integration over the aperture of the transducer. The results presented in this paper were obtained with the numerical integration techniques. To improve the computational efficiency and speed of computation of the near field radiation pattern, it will be a noteworthy contribution if the associated two-dimensional integral is simplified to a closed-form expression. An analytical formulation that transforms the proposed formulation to even a one-dimensional integration will also be of significant contribution, since it facilitates a considerable reduction in the computational burden in determination of near field radiation pattern of acoustic transducers.

Copyright © 2020 Praise Worthy Prize S.r.l. - All rights reserved

References

- [1] Khairul A. Ahmad, A.B.D. Manaf, M.F.A. Rahman, Design of polyimide based piezoelectric micro-machined ultrasonic transducer for underwater imaging application, *Proceedings of the International Conference on Imaging, Signal Processing and Communication*, pp. 63-66, Penang, Malaysia, 2017.
- [2] Eric Westman, Underwater Localization and Mapping with Imaging Sonar, Ph.D. Thesis, Carnegie Mellon University, Pittsburgh, PA, 2019.
- [3] Xuebo Zhang, Biao Fang, Synthetic aperture image formation for multi-receiver synthetic aperture sonar, *IEEE International Conference on Computer and Communications*, pp.2060-2064, Dec 2017.
- [4] Sibo Sun, Yingchun Chen, LonghaoQiu, Guangpu Zhang, and Chunhui Zhao, Inverse Synthetic Aperture Sonar Imaging of Underwater Vehicles Utilizing 3-D Rotations, *IEEE Journal of Oceanic Engineering*, Vol. 45, Issue 2,2020.
- [5] Simone Sternini, Albert Y Liang and Francesco Lanza di Scalea, Ultrasonic synthetic aperture imaging with interposed transducer medium coupling path, *Sage Journals, Structural Health Monitoring*, Vol. 18, Issue: 5-6, pp. 1543-1556, 2018.
- [6] Herlambang, T., Subchan, S., Nurhadi, H., Design of Motion Control Using Proportional Integral Derivative for UNUSAITS AUV, (2018) *International Review of Mechanical Engineering* (IREME), 12 (11), pp. 928-938. doi: https://doi.org/10.15866/ireme.v12i11.15758
- [7] Hyo Won Park, Modeling and Simulation of Acoustic Pressure Field for Ultrasonic Tactile Displays, Master thesis, Lehigh University, Pennsylvania, USA, 2017.
- [8] Chater, N., Mazri, T., Benbrahim, M., Study, Simulation and Optimization of an 8×1 Array Antenna for Electronic Scanning Radar Application, (2018) International Journal on Communications Antenna and Propagation (IRECAP), 8 (6), pp. 469-476. doi: https://doi.org/10.15866/irecap.v8i6.14336
- [9] A. R. Selfridge, G. S. Kino, and B. T. Khuri-Yakub, A theory for the radiation of a narrow-strip acoustic transducer, *Journal for Applied Physics Letters*, Volume 37, (Issue-1), 1980, pages 35-36.
- [10] Rongrong Lu, Rama Rao, and Nafi Toksoz, Measured radiation patterns of the scale model dipole tool, Master of Science Thesis. Massachusetts Institute of Technology, Cambridge, MA, 2014.
- [11] Hayden J. Callow, Signal processing for synthetic aperture sonar image enhancement, Ph.D. Thesis. University of Canterbury, Christchurch, New Zealand, 2003.
- [12] Peter R. Stepanishen, Transient radiation from pistons in an infinite planar baffle, *The Journal of the Acoustical Society of America*, vol. 49, 2005, pages 1629-1971.
- [13] Haim Azhari, Basics of biomedical ultrasounds for engineers, 1stEdition, (John Wiley and Sons, 2010, pp. 153-185).
- [14] Brett T. Walkenhorst, Test Environments for 5G Millimeter-Wave Devices, IEEE European Conference on Antennas and Propagation. Poland. 2019.
- [15] Abdul Malek, N., Mat Ramli, N., Abdullah, K., Null Positioning of Dipole Antenna Array Considering Coupling Effect, (2017) International Journal on Communications Antenna and Propagation (IRECAP), 7 (5), pp. 370-377. doi: https://doi.org/10.15866/irecap.v7i5.11718
- [16] Constantine A. Balanis (1997), Antenna Theory: Analysis and Design, (@John wiley & Sons, Inc., 1997, pp. 25-105).
- [17] Douglas A. Abraham, Underwater Acoustic Signal Processing: Modeling, Detection, and Estimation, (© Springer Nature Switzerland, 2019, pp. 3-196).
- [18] Lawrence J. Ziomek, An Introduction to Sonar Systems Engineering, (© Taylor& Francis Groups, 2017, pp. 1-200).
- [19] Daniel A. Cook, Daniel C. Brown, Synthetic Aperture Sonar Image Contrast Prediction, *IEEE Journal of Oceanic Engineering*, Vol. 43, Issue: 2, pp.523-535, 2018.
- [20] Jasmine Mathew, Acoustic Radiation and Scattering from Cylindrical Bodies and Analysis of Transducer Arrays. Ph.D. thesis. Naval Physical and Oceanographic Laboratory, DRDO 2011.

Authors' information



Praveen L. S. is an Assistant Professor at M. S. Ramaiah University of Applied Sciences, Bangalore.He graduated from Visvesvaraya Technological University with a B.E. degree in Medical Electronics and was awarded M. Sc. [Engg.] degree in Signal Processing and Communication Engineering. Currently, he is pursuing his Ph.D.degree with a focus on UAI.



Govind R. Kadambi is Pro Vice-chancellor of M. S. Ramaiah University of Applied Sciences, Bangalore. He graduated from Mysore University with a B.E. degree in Electronics and Communication Engineering. He holds M.S. and Ph.D. degrees from IIT, Madras with specialization in Antennas.



S. Malathi is an Associate Professor at M. S. Ramaiah University of Applied Sciences, Bangalore. She graduated from Madras University with a B.E degree in Electronics and Communication Engineering. She has M.E. degree in Microwave and Optical Engineering, Madurai Kamaraj University and holds Ph.D. degree from IISc, Bangalore.



Preetham Shankapal is a Data Scientist in GE Healthcare, Bangalore. She graduated from Visvesvaraya Technological University with a B.E. degree in Medical Electronics. Preetham pursued her M.Sc.[Engg.] degree in Biomedical Engineering, University of Warwick and she holds Ph.D. degree from Coventry University.



Dual-Band Circularly Polarized Millimeter-Wave Antenna for 5G-WiGig Applications

Nada Abd El-Latif¹, Hany M. Zamel¹, Ahmed M. Attiya¹, Amr Al-Awamery²

Abstract – In this paper, a dual band dual circularly polarized microstrip antenna for 28/60 GHz applications is presented. This antenna is designed to be used in hand-held devices for both 5G and WiGig applications simultaneously. The circular polarization in this case represents an important advantage to avoid polarization mismatch at different orientations. The proposed antenna consists of two parts: an annular ring around a circular patch with slot perturbations in both of them. The two parts of the proposed antenna are resonant at different frequencies. The inner circular patch is designed to be resonant around the 60 GHz band while the annular ring is designed to be resonant around the 28 GHz band. These two parts are simultaneously excited by an arc-shaped strip. Each part of this antenna structure operates as a single band circularly polarized radiator. The circular polarization is obtained by exciting orthogonal modes in each part of this antenna configuration with equal amplitudes and 90° phase shift. These orthogonal modes are obtained by introducing perturbations in both the inner circular disk and the outer annular ring. These perturbations are shifted by 45° from the location of the feeding arc. However, these perturbations affect the matching properties of designed antenna. Thus, a meander line stub is connected to the annular ring to adjust the matching of the designed antenna. The characteristics of the proposed antenna are designed and simulated by using full-wave EM simulator CST Microwave Studio and High Frequency Structural Simulator (HFSS). Copyright © 2020 Praise Worthy Prize S.r.l. - All rights reserved.

Keywords: Circular Ring, 5G, Millimeter Wave, Dual Circularly Polarized Microstrip Antenna

Nomenclature W_{s2} Width of slot perturbation in the annular slot a, bLengths of the sections of the matching ϕ_1 Angle of the feeding arc [°] meander line stub [µm] Relative Permittivity of the substrate ε_r cSpeed of light [m/s] Effective dielectric constant ϵ_{eff} Resonant frequency of the fundamental f_0 Guided wave length [m] λ_{g} mode of the annular ring [GHz] The first zero of the derivative of the first χ_{11} Second resonance frequency [GHz] f_{r2} kind Bessel function of order 1 Substrate thickness [mm] h 5G Fifth Generation Length of slot perturbation in the circular L_{s1} Computer Simulation Technology **CST** disk [µm] **GSM** Global System for Mobile Communications Length of slot perturbation in the annular L_{s2} **HDTV** High Definition television ring [µm] High frequency structure simulator **HFSS** Correction factor Left Hand Circular Polarization **LHCP** R_1 Radius of the circular disk patch [µm] **RHCP** Right Hand Circular Polarization R_2 Inner radius of the feeding arc [um] **UHDV** Ultra-High Definition Video R_3 Outer radius of the feeding arc [µm] WiFi Wireless Fidelity Inner radius of the annular ring [µm] R_4 Worldwide Interoperability for Microwave WiMax R_5 Outer radius of the annular ring [µm] Access Average radius of the annular ring [µm] WiGig Wireless Gigabit Radius of inner circular slot inside the **WLAN** Wireless Local Area Network circular disk [µm] Loss tangent of the substrate tanδ I. Introduction Width of the matching meander line stub Recent advances in 5G mobile communication and Width of slot perturbation in the circular disk W_{s1} multi-gigabit communication systems are mainly based $[\mu m]$

on using mm-wave signals. Multi-gigabit communication systems have a significant importance in developing High Definition Television (HDTV) and Ultra-High Definition Video (UHDV), [1], [2]. The expected bands for cellular access at 5G mobile communications are 28 and 38 GHz bands [3]-[5]. On the other hand, WiGig system is based on 60 GHz band [6] [7]. To integrate 5G and WiGig applications in the same device, it would be required to develop a multi-band antenna to cover both 5G and Wi-Gig bands. This was the motivation for different researchers to develop mm-wave multi-band antennas for 5G-WiGig antennas [8]. Similar multiband antenna configurations were also developed for lower frequency bands of WiFi, GSM, WLAN and WiMAX applications [9]-[11]. In addition, circular polarization has the advantage that the transmitting and the receiving antennas should not be aligned at specific orientations as in the case of linear polarizations [12], [13]. This property simplifies the connections between the transmitter and the receiver at any orientation. This is the motivation in this paper to develop an mm-wave multiband circularly polarized antenna for 5G-WiGig printed antenna structure. The circular polarization in the present case represents the new advantage compared to the previously published similar antennas. polarization can be obtained in general be generating two orthogonal fields of equal amplitudes and phase shift $\pm 90^{\circ}$ [14]-[16]. Generally, these conditions can be satisfied at narrow bands. These conditions can be satisfied for simple printed antennas by using symmetric shape patches like square or circular patches with dual feeding system of equal amplitudes and phase shift ±90°.

These conditions can also be satisfied by using a single feeding point for a slightly asymmetric shape like elliptical shape [10] or by adding diagonal perturbations on the patch [17]. These perturbations can be small slots or small strips. The area of this perturbation compared to the area of the patch represents a main parameter in controlling the condition of circular polarization [18]-[20]. To develop these conditions at multi-band antenna, it would be required to construct an antenna of different parts which are used to generate circular polarizations at different frequencies. Different configurations of multiband circularly polarized antennas are presented in [21]-[25]. These configurations include circular disk with capacitive feeding structure to increase the operating bandwidth [21]. The circular polarization in this case is obtained by adding linear and curved slots at the circular patch. By adjusting the lengths of these slots and the location of the capacitive feeding structure, dual band circular polarization could be obtained around 2.4 and 3.8 GHz. Another configuration based on a square slot antenna fed by a microstrip line is presented in [22]. The orthogonal modes in this case are obtained in a band by adding two rectangular perturbations at opposite corners of this square slot. In addition, other two opposite split ring resonators are used to introduce other orthogonal modes in a higher frequency band to introduce another circular polarization band. This configuration is used to

develop a dual band circularly polarized antenna at frequency bands around 3.1 and 4.7 GHz. Another configuration based on two eccentric rings is proposed in [23]. In this case, the offset positions of the centers for the different rings control the orthogonality of the radiated field components while the values of the radii control the operating frequency band. The antenna in [23] was designed to be operating in the frequency bands around 2.1 and 3.6 GHz. In [25], the antenna is composed of a circular patch antenna with an elliptical slot. The antenna is feed by simple microstrip line and the elliptical slot is located on the other end along the extension of the same line of the feeding point. By controlling the size of the elliptical slot, it was possible to introduce circular polarization at two bands around 28 and 45 GHz. In this paper, we develop a new circularly polarized antenna for multi-band mm-wave applications in the frequency ranges 28 and 60 GHz. The proposed antenna is a combination between a circular patch and an annular ring structure. The circular patch is tuned on 60 GHz while the annular ring is tuned on 28 GHz. The two structures are simultaneously fed by an arc strip patch fed by a probe. To obtain the circular polarization, perturbations are added to both the circular disc and the ring. The proposed perturbations are rectangular slots located at an angle 45° w.r.t. the feeding point to introduce the required two orthogonal modes. These perturbations have an effect on the matching properties of the original circular disk and annular ring. Thus, an additional matching meander stub is used to improve the matching of the antenna after adding the perturbations which are required to introduce the circular polarization.

The organization of the paper is as follows. In Section II, the design of multi-band linearly polarized circular patch antenna at 60 GHz is presented. Then, another annular ring is added to the circular disk to operate around 28 GHz. In Section III, the two parts are combined to introduce the multi-band circularly polarized antenna. Section IV presents verification of results and discussions of the radiation patterns. Finally, the conclusion is presented. The present analysis is based on using Ansoft HFSS simulation and is verified by using CST Microwave Studio.

II. Design and Analysis of Multi-band Linearly Polarized Antenna

The proposed antenna is designed on a low loss substrate Rogers RT/duroid 5880 with a substrate thickness h=0.381 mm and a dielectric constant of ε_r =2.2.

The loss tangent of the substrate is tanδ=0.0009. The design of the antenna structure starts with a circular disk antenna coupled to an arc strip which is connected to a coaxial probe as shown in Fig. 1. The initial value for the radius of the circular disk is determined by using cavity model as follows [19]:

$$R_1 = \frac{c}{2\pi\sqrt{\varepsilon_r}} \frac{\chi'_{11}}{f_{r2}} \tag{1}$$

Copyright © 2020 Praise Worthy Prize S.r.l. - All rights reserved

where $\chi'_{11} = 1.8412$ and $f_{r2} = 60$ GHz. This initial value is nearly 987 μ m. This value is optimized to be about 800 μ m to improve the matching with the feeding arc strip. The feeding arc has an inner radius R_2 =830 μ m and an outer radius R_3 =1000 μ m. The feeding arc is limited by an angle ϕ_1 =60°. Fig. 2 shows the resulting reflection coefficient in the upper frequency band from 59 to 61 GHz. The next step in the design of the proposed antenna is to add another annular ring to operate around 28 GHz as shown in Fig. 3. For a circular annular ring, the fundamental resonant mode (TM₁₁ mode) of this annular ring occurs at a frequency f_0 , given by [9]-[16]:

$$f_0 = \frac{c}{\pi (R_1 + R_2) \sqrt{\varepsilon_{eff}}}$$
 (2)

where c is the speed of light in free space and ε_{eff} is the effective dielectric constant given by:

$$\varepsilon_{eff} = 1 + q (\varepsilon_r - 1)$$
 (3)

q is the correction factor, which is about 0.702, and $\pi(R_1+R_2)$ is the mean circumference of the annular ring.

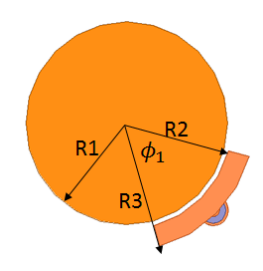


Fig. 1. Initial circular disk antenna fed by an arc-shaped strip

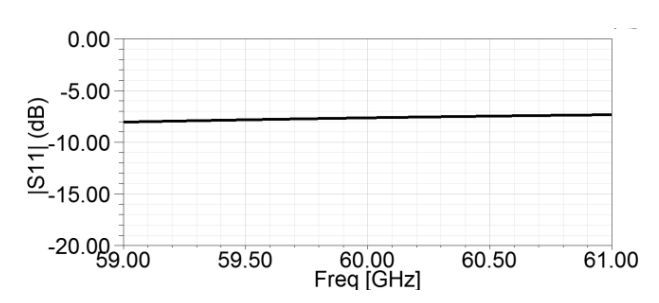


Fig. 2. Reflection coefficient of the circular disk antenna shown in Fig. 1 around 60 GHz

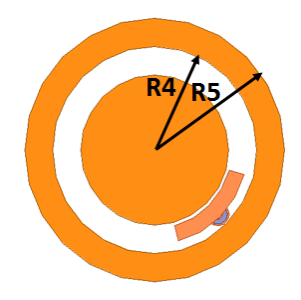
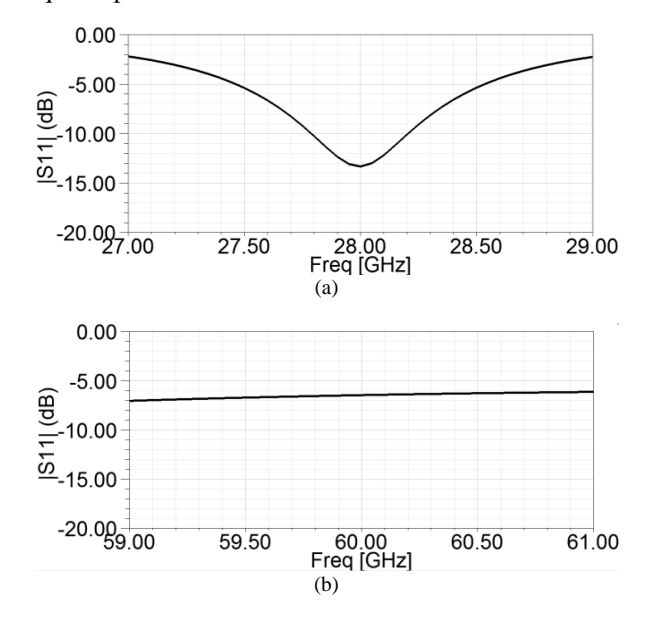


Fig. 3. Combined annular ring with a circular disk antenna fed by an arc strip

This annular ring has an inner radius R_4 =1100 µm and an outer radius R_5 =1420 µm. The average radius of this annular ring is $R_{avg} = \frac{R_4 + R_5}{2} = 1260$ µm. The circumference of this average radius equals nearly the guided wavelength λ_g on this annular ring at frequency 28 GHz. Thus, this annular ring represent a simple loop antenna which is resonant at 28 GHz. Figs. 4 show the reflection coefficients of this combined antenna structure at both lower and upper frequency bands. It can be noted that the presence of this outer annular ring reduces the matching at the upper frequency band.

III. Design and Analysis of Multi-Band Circularly Polarized Antenna

To adjust the reflection coefficient at the upper frequency band in addition to convert the radiation from the circular disk to be circular polarization, two rectangular slots perturbations are extracted from the inner disk and also a small circular slot is extracted from its center as shown in Fig. 5. The details of using a perturbation in a symmetric geometry like a circular patch or an annular ring to introduce circular polarization are discussed in [27, Sec. 4-2]. These perturbations are added to introduce two modes along the antenna structure. One of these two modes is oriented along the line connecting the two perturbation and the other is oriented normal to this line. By adjusting the ratio of the area of the perturbation to the total area of the antenna structure, it would be possible to introduce a phase shift $\pi/2$ between the two generated modes. In this case, the radiated field would be circular polarization. This ratio is a function of the quality factor of original antenna structure without a perturbation. In the present case, two symmetric rectangular slots are extracted from the circular patch as shown in Fig. 5 to introduce the required perturbation.



Figs. 4. Reflection coefficients of the antenna at Fig. 3; (a) Lower frequency band, (b) Upper frequency band

Copyright © 2020 Praise Worthy Prize S.r.l. - All rights reserved

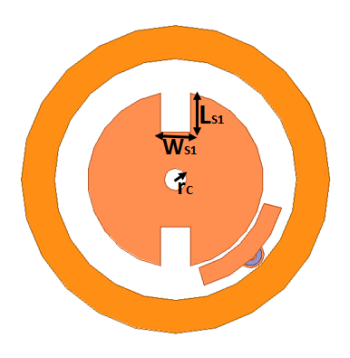


Fig. 5. Combined antenna structure with extracting slots from the inner disk

These slots have a length $L_{\rm s1}$ =354 µm and a width $W_{\rm s1}$ =268 µm. The inner circular slot has a radius r_c =100 µm. Fig. 6 shows the reflection coefficient at the upper frequency band after adding these slots in the inner disk.

It can be noted that the matching in this case has a significant improvement. On the other hand, Fig. 7 shows the corresponding axial ratio at the upper frequency band. It can be noted that the obtained axial ratio in this case is below 3 dB in the frequency range from 59.5 to 61 GHz. In a similar way, to introduce circular polarization in the lower frequency band, other two symmetric rectangular slots with a length L_{s2} =60 μ m and a width $W_{s2}=200 \mu m$, are extracted from the annular slot as shown in Fig. 8. However, in this case, the obtained resonance is shifted at a slightly lower frequency than 28 GHz while the obtained circular polarization is obtained at a slightly higher frequency than 28 GHz as shown in Figs. 9(a) and 10(a) respectively. To compensate this effect, an additional short circuited stub is added to the outer ring as shown in Fig. 11.

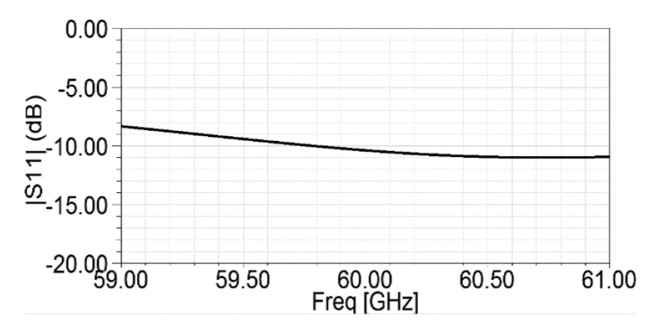


Fig. 6. Reflection coefficient of the modified antenna structure in Fig. 5 in the upper frequency band

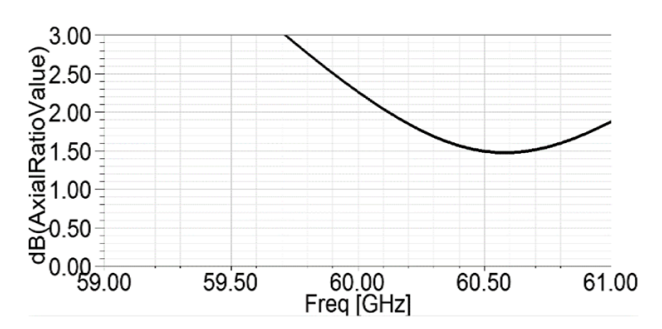


Fig. 7. Axial ratio of the modified antenna structure in Fig. 5 in the upper frequency band

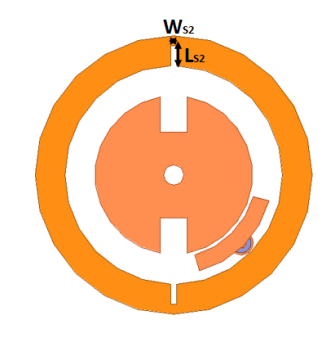
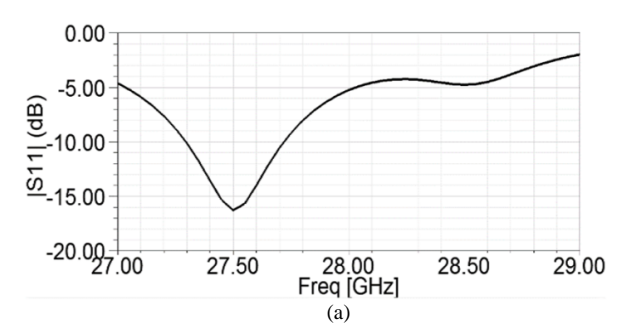
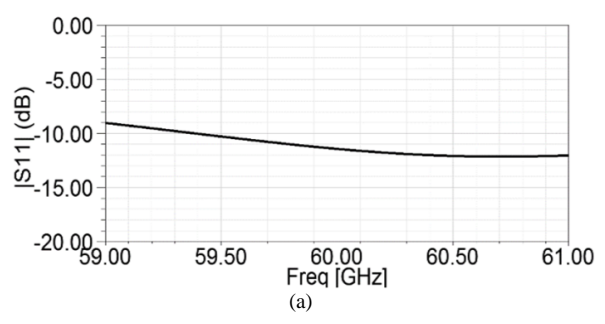
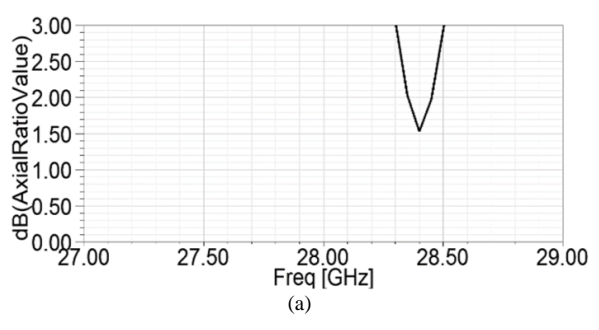


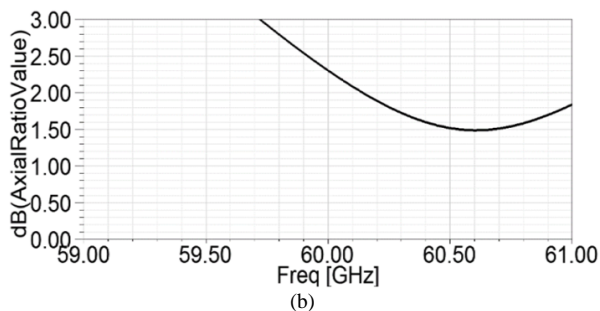
Fig. 8. Combined antenna structure with extracting slots from the inner disk and the annular ring





Figs. 9. Reflection coefficients of the antenna at Fig. 8; (a)Lower frequency band, (b) Upper frequency band





Figs. 10. Axial ratio of the modified antenna structure in Fig. 8; (a) Lower frequency band, (b) Upper frequency band

Copyright © 2020 Praise Worthy Prize S.r.l. - All rights reserved



Fig. 11. Modified antenna structure with adding slots in the inner disk and the annular ring and a matching meander at the outer ring. The dimension of the mender are a=245 μ m, b=313 μ m and the mender width w=54 μ m

Fig. 12 shows the simulated reflection coefficient of the modified antenna with the meander matching stub and the antenna without the matching stub. It can be noted that the matching in the case of the antenna with the stub has a significant improvement at the two design frequencies 28 GHz and 60 GHz. This can be explained due to that the feeding mechanism of this antenna configuration is mainly capacitive. Thus, adding the short circuited meander line to the annular ring introduces an inductive effect which compensates the capacitive effect of the feeding structure. It should be noted that this meander line was originally designed as a short circuited transmission line stub. Then, it is converted into a meander shape to reduce the total dimension of the complete antenna structure. The total dimensions of the complete antenna and the sections of the matching meander line are presented in Table I.

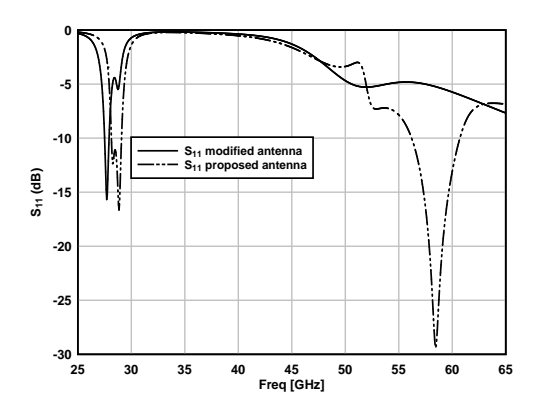


Fig. 12. Simulated S_{11} of the modified antenna with the matching stub and proposed antenna without the matching stub

T	ABLE I
Dimension	Value (mm)
Н	0.381
R_1	0.8
R_2	0.83
R_3	1
R_4	1.1
R_5	1.42
r_c	0.1
L_{S1}	0.354
W_{S1}	0.268
L_{S2}	0.06
W_{S2}	0.2
a	0.245
b	0.313
w	0.054

IV. Verifications of Results and Discussions

Fig. 13 shows the simulated reflection coefficient after adding the matching stub. The simulation in this case is obtained by using HFSS and verified by CST. It can be noted that there is a good agreement between the simulated results of reflection coefficients by using the two simulators. On the other hand, Fig. 14 shows the simulated results of the axial ratio at the two frequency bands. The simulation is also obtained by using HFSS and verified by CST Microwave Studio. It can be noted that the axial ratio in the two design bands is below 3 dB.

Figures 15 and 16 show the obtained RHCP/LHCP radiation patterns at the two frequency bands, 28 and 60 GHz, in the planes ϕ =0° and 90°. It can be noted that the RHCP component is the dominant component in the radiation pattern in both cases.

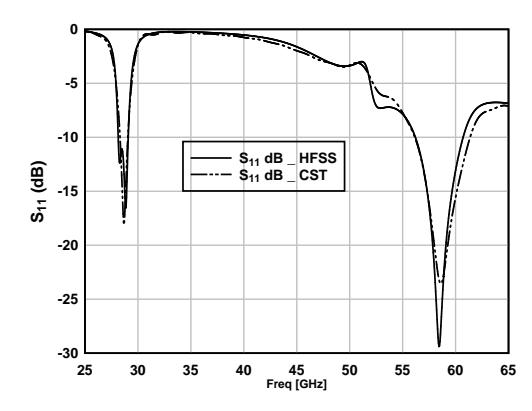


Fig. 13. Verification of Reflection coefficient of the designed antenna

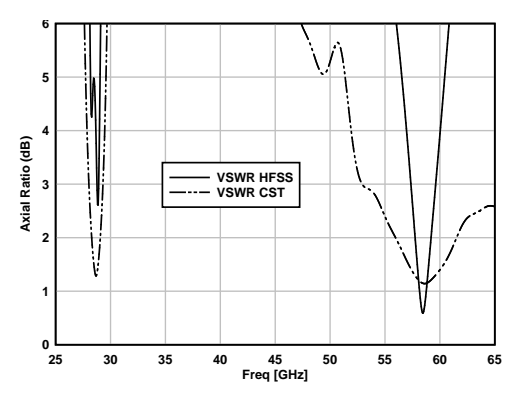


Fig. 14. Verification of Axial ratio of the designed antenna

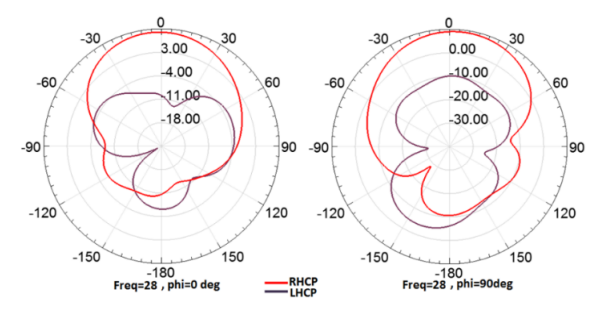


Fig. 15. Radiation pattern of the designed antenna for LHCP, RHCP at 28GHz for ϕ =0° and 90°

 $Copyright © 2020 \ Praise \ Worthy \ Prize \ S.r.l. \ - All \ rights \ reserved$

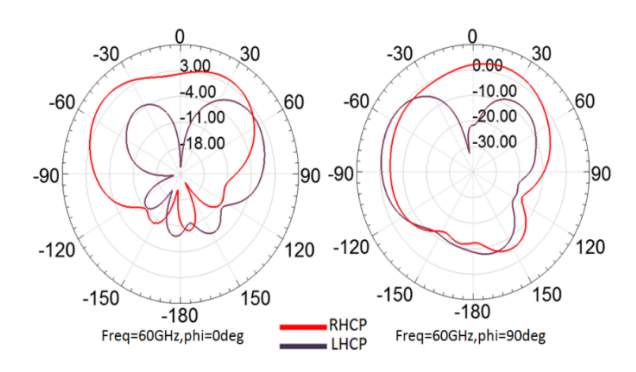


Fig. 16. Radiation pattern of the designed antenna for LHCP, RHCP at 60 GHz for φ =0° and 90°

V. Conclusion

A dual band RHCP microstrip antenna is designed for 5G and WiGig applications in the frequency bands around 28 and 60 GHz respectively. The antenna consists of combination of a circular disk and an annular ring.

The two parts of the antenna are fed simultaneously by an arc-shaped strip fed by a coaxial connector. Slots are added to both the circular disk and the annular ring to obtain circular polarization at the proposed frequency bands. A matching short circuited mender line is added to the outer annular ring to match the antenna at the lower frequency band. The proposed antenna is designed by using HFSS and the obtained results are verified by using CST. The obtained results show that the reflection coefficient of the excitation port at the proposed frequency bands is less than -10 dB and the corresponding axial ratio of the radiated fields is below 3 dB. The designed antenna can be a good candidate for the applications combining 5G and WiGig. It is proposed to study a combination of this antenna on a single substrate having the size of a handheld device to study the possibility of using this antenna structure for Multiinput multi-output application in 5G communications.

Also, it proposed to study the specific absorption rate of this antenna structure and check the possibility of reducing it by adding a surrounding printed electromagnetic bandgap structure.

References

- S. Hakimi, S. K. A. Rahim, Millimeter-wave microstrip bent line grid array antenna for 5G mobile communication networks, *Asia-Pacific Microwave Conference (APMC)*, Nov. 2014, Pages 622–624.
- [2] N. Ojaroudiparchin, M. Shen, G. F. Pedersen, A 28GHz FR-4 compatible phased array antenna for 5G mobile phone applications, IEEE International Symposium Antennas and Propagation (ISAP), Pages 1–4, IEEE, November 2015.
- [3] A. Kumar, M. Gupta, A review on activities of fifth generation mobile communication system, *Alexandria Engineering Journal*, Vol. 57, No. 2, June 2018, Pages 1125–1135.
- [4] M. I. Khattak, A. Sohaill, U. Khan, G. Witjaksono, Elliptical Slot Circular Patch Antenna Array with Dual Band Behavior for Future 5G Mobile Communication Networks, *Prog. In Elec. Res.* (*PIER*) C, Vol. 89, 2019.
- [5] Y. Niu, Y. Li, D. Jin, et al., A Survey of Millimeter Wave (mmWave) Communications for 5G: Opportunities and

- Challenge, Wireless Networks, Vol. 21, No. 8, 2015, Pages 2657-2676.
- [6] C. Hansen, WiGiG: Multi-gigabit wireless communications in the 60 GHz band, *IEEE Wireless Communications*, Vol. 18, No. 6, 2011, Pages 6-7.
- [7] Kumar, P., Antennas and Arrays for 60 GHz High Data Rate Wireless Applications, (2019) International Journal on Communications Antenna and Propagation (IRECAP), 9 (4), pp. 255-262. doi: https://doi.org/10.15866/irecap.v9i4.14473
- [8] D. Wang and C. H. Chan, Multiband Antenna for WiFi and WiGig Communications, *IEEE Antennas and Wireless Propagation Letters*, vol. 15, 2016, Pages 309-312.
- [9] Kueathaweekun, T., A Study of Dual/Triple-Band Microstrip-Fed Slot Antenna Design for WLAN/WiMAX Communication Systems, (2017) International Journal on Communications Antenna and Propagation (IRECAP), 7 (2), pp. 95-103. doi: https://doi.org/10.15866/irecap.v7i2.11654
- [10] Singh, V., Mishra, B., Pandey, A., Patel, A., Yadav, S., Singh, R., Triple Band CPW Fed Monopole Leaf Shaped Patch Antenna, (2017) International Journal on Communications Antenna and Propagation (IRECAP), 7 (2), pp. 135-141. doi: https://doi.org/10.15866/irecap.v7i2.11842
- [11] Mahmood, Z., Nasret, A., Awed, A., Design of New Multiband Slot Antennas for Wi-Fi Devices, (2019) *International Journal on Communications Antenna and Propagation (IRECAP)*, 9 (5), pp. 334-342. doi: https://doi.org/10.15866/irecap.v9i5.16754
- [12] Al-Muttairi, A., Farhan, M., Circular Polarization Reconfigurable Antenna Based on Defect Ground Structure for Mid-Band 5G Applications, (2020) International Journal on Communications Antenna and Propagation (IRECAP), 10 (2), pp. 114-121. doi: https://doi.org/10.15866/irecap.v10i2.18427
- [13] Ibrahim, M., 2×2 Circularly Polarized MIMO Antenna at Ka-band for Fifth Generation Applications, (2019) *International Journal* on Communications Antenna and Propagation (IRECAP), 9 (2), pp. 100-109. doi: https://doi.org/10.15866/irecap.v9i2.16051
- [14] Row and Lin, Design of an annular-ring microstrip antenna for circular polarization, *Micro. And opt. Tech. Lett.*, Vol. 42, No. 2, July 2004, Pages 156-157.
- [15] Lin, Chen and Lin, A New coupling mechanism for circularly polarized annular ring patch antenna, *IEEE Trans. on Ant. And Prop.*, Vol. 56, No. 1, Jan. 2008, Pages 11-16.
- [16] S. Gao, Q. Luo and F. Zhu, Circularly Polarized Antennas (John Wiley & Sons, 2014).
- [17] Ahmed, S., Zakaria, Z., Husain, M., Alhegazi, A., A Novel Design of Circularly Polarized Aperture-Coupled Antenna with Harmonic Rejection for Rectenna Application, (2018) International Journal on Communications Antenna and Propagation (IRECAP), 8 (4), pp. 288-293. doi: https://doi.org/10.15866/irecap.v8i4.12805
- [18] Y. F. Lin, Y. C. Kao, S. C. Pan, H. M. Chen, Bidirectional Radiated Circularly Polarized Annular-Ring Slot Antenna for Portable RFID Reader, ACES Jour., Vol. 25, No. 3, March 2010.
- [19] Y. Cheng, H. Liu, A Novel Concentric Annular-Ring Slot Dual-Band Circularly Polarized Microstrip Antenna, *International Journal of Antennas and Propagation*, Hindawi, Vol. 2018.
- [20] M. Rahman, E. Nishiyama, I. Toyoda, A Polarization Reconfigurable Microstrip Antenna Employing Dual-Perturbation Technique, *Progress In Electromagnetics Research* M, Vol. 69, 2018.
- [21] Q. Li, F. Zhang, G. Zhang, B. Wang, M. Liang, A Single-feed Dual - Band Dual - Sense Circularly Polarized Microstrip Antenna, Progress In Electromagnetics Research C, vol. 51,2014.
- [22] K. Kandasamy, B. Majumder, J. Mukherjee, K. Ray, Dual-Band Circularly Polarized Split Ring Resonators Loaded Square Slot Antenna, *IEEE Transactions on Antennas and Propagation*, Vol. 64, No. 8, 2016. Pages 3640-3645.
- [23] Z. X. Liang, D. C. Yang, X. C. Wei, E. P. Li, Dual-Band Dual Circularly Polarized Microstrip Antenna With Two Eccentric Rings and an Arc-Shaped Conducting Strip, *IEEE Ant. and Wireless Prop. Lett*, Vol. 15, 2016. Pages 834-837.
- [24] K. Mahmoud, A. Montaser, Performance of Tri-band Multi-

Copyright © 2020 Praise Worthy Prize S.r.l. - All rights reserved

- Polarized Array Antenna for 5G Mobile Base Station Adopting Polarization and Directivity Control, *IEEE Access*, Vol. 6, 2018. Pages 8682-8694.
- [25] M. I. Khattak, A. Sohail, U. Khan, Z. Barki, G. Witjaksono, Elliptical Slot Circular Patch Antenna Array with Dual Band Behavior for Future 5G Mobile Communication Networks, *Prog. In Elec. Res. (PIER) C*, Vol. 89, 2019.
- [26] C. Balanis, Antenna Theory Analysis and Design, 2nd Ed., (John Wiley & Sons, 1997).
- [27] J. R. James, P. Hall, eds. Handbook of microstrip antennas. (IET, 1989).

Authors' information

¹Electronics Research Institute, Microwave Engineering Dept. – Cairo - Egypt.

²Faculty of Engineering, Benha University – Benha - Egypt.



Nada Abd El-Latif graduated from El-Obuor High Institute of Engineering and Technology – Electronics and Communication Dept. at 2014. She joined to Electronics Research Institute (ERI) in Egypt at 2016. She is a postgraduate student at Faculty of Engineering – Banha University. This work is a part of here M.Sc. research.



Hany M. Zamel received the B.S. degree in communication and electronics engineering from Faculty of Engineering, Zagazig University, the M.S. degree from Faculty of Engineering, Cairo University, and the Ph.D. degree in communication and electronics engineering from Faculty of Engineering, Ain Shams University in 1999, 2007, and 2014,

respectively. He joined Electronics Research Institute as a Researcher Assistant in 2001. He is currently a researcher at Microwave Engineering department. His research interests includes microstrip antennas, millimeter wave antennas, Metamaterials and RCS reduction.



Ahmed M. Attiya M.Sc. and Ph.D. Electronics and Electrical Communications, Faculty of Engineering, Cairo University at 1996 and 2001 respectively. He joined Electronics Research Institute as a Researcher Assistant in 1991. In the period from 2002 to 2004 he was a Postdoc in Bradley Department of Electrical and Computer Engineering at Virginia Tech. In the

period from 2004 to 2005 he was a Visiting Scholar in Electrical Engineering Dept. in University of Mississippi. In the period from 2008 to 2012 he was a Visiting Teaching Member in King Saud University. He is currently Full Professor and the Head of Microwave Engineering Dept. in Electronics Research Institute. He is also the Founder of Nanotechnology Lab. in Electronics Research Institute. His research interests include Electromagnetic waves, antennas and wave propagations, microwave passive circuits and systems, microstrip and planar circuits and antennas, antenna measurement techniques, microwave measurement techniques, UWB and short pulse signals, numerical techniques in electromagnetics, analytical techniques in electromagnetics, periodic structures, artificial electromagnetic materials, nanotechnology, carbon nanotubes, graphene, plasmonics and non-linear optics. Attiya is an Editor-in-Chief of "Open Journal of Antennas and Propagation". In 2008, Attiya was awarded the Encouragement Award in Engineering Science from Egyptian Scientific and Research Academy.



Amr A. Al-Awamery Lecturer in Benha Faculty of Engineering. Ph.D. 2012 in Antenna and Microwave devices from Saint Petersburg Electro technical University.



Visibility Modeling and Prediction for Free Space Optical Communication Systems for South Africa

Olabamidele O. Kolawole¹, Modisa Mosalaosi², Thomas J. O. Afullo¹

Abstract – Due to the cost and complexity in the measurement of Free Space Optical (FSO) visibility, this paper presents regression models based on meteorological factors to reliably estimate atmospheric visibility. The meteorological factors used are relative humidity, temperature, fractional sunshine, atmospheric pressure and wind speed for Cape Town, South Africa. Initially, Simple Linear Regression (SLR) models are developed and presented. To improve the performance of the regression, the SLR model is extended to a Multiple Linear Regression model (MLR) where three of the meteorological factors are taken into consideration simultaneously. It was found that by implementing MLR, the model performance improves considerably. However, it was also found that the model had effects of multicollinearity due to some of the predictor variables being highly correlated. To mitigate the effects of multicollinearity, two approaches are proposed, 1) removing the problematic terms from the regression model and 2) introducing interaction terms. Both approaches are seen to have little impact on the overall performance of the MLR model while the estimated model coefficients are significant at 5% significant level. In general, it is found through application of standard statistical tests that both SLR and MLR models can be used adequately to determine visibility at a location. Copyright © 2020 Praise Worthy Prize S.r.l. - All rights reserved.

Keywords: Free Space Optics, Visibility, Regression, Correlation Matrix, Multicollinearity, Variance Inflation Factor

	Nomenclature	β_{WS}	Regression coefficient of the WS
			independent variable
AP	Atmospheric pressure [mb]	$corr(M_i, M_j)$	Correlation matrix
b_0	Estimate of β_0	CI	Confidence interval
b_1	Estimate of β_1	e_i	Residual terms
b_{j}	Estimate of β_i	€	Error term in vectorized form
b_m	Estimate of β_m	\in_i	Error terms
b_{FSH}	Estimate of β_{FSH}	E	Mean of a variable
b_{RH}	Estimate of β_{RH}	FSH	Fractional sunshine
b_{WS}	Estimate of β_{WS}	FSO	Free Space Optics
β	Regression coefficient of an MLR	GPR	Gaussian Process Regression
	model in vectorized form	GRNN	Generalized Regression Neural
β_0	Intercept		Network
β_1	Regression coefficient of the only	H_0	Null hypothesis
	independent variable in the SLR	H_1	Alternative hypothesis
0	model	I	Signal intensity [cd]
β_{FSH}	Regression coefficient of the FSH	I_0	Transmitted signal intensity [cd]
0	independent variable	iBurst	High Capacity Spatial Division
β_I	Regression coefficient of interaction		Multiple Access
0	terms	IEEE	Institute of Electrical and Electronics
β_j	Regression coefficients of the		Engineers
	independent variables in the	IoT	Internet of Things
0	regression model	IR	Infra-red
β_m	m th slope parameter or the m th	IV	Independent Variable
	regression coefficient in an MLR	L	Link distance [km]
0	model	L_b	Lower bound term
β_{RH}	Regression coefficient of the <i>RH</i>	M-MIMO	Massive Multiple-Input Multiple-
	independent variable		Output

MBE	Mean Bias Error	VSB_{ALL}	Estimated visibility using the MLR
MLR	Multiple Linear Regression	VSD _{ALL}	model containing the <i>RH</i> , <i>FSH</i> and
MLR_{ALL}	Multiple Linear Regression model		WS predictor variables [km]
	containing the RH, FSH and WS	VSB_{AP}	Estimated visibility from the AP
	predictor variables		predictor variable [km]
MLP	Multi-Layer Perceptron Neural	VSB_{BLOEM}	Estimated visibility using the best
MDE	Network	VCD	MLR model for Bloemfontein [km]
MPE	Mean Percentage Error Millimetre wave	VSB_{DBN}	Estimated visibility using the best SLR model for Durban [km]
mm n	Actual amount of sunshine hours in a	VSB_{FSH}	Estimated visibility from the <i>FSH</i>
Ti.	day	VSDFSH	predictor variable [km]
N	Maximum possible amount of	$VSB_{FSH imes WS}$	Estimated visibility using the MLR
	daylight hours	1 311	model containing interaction terms
N	Normal distribution		$FSH \times WS$ and the RH predictor
NGN	Next-Generation Network		variable [km]
Ns	Number of samples	VSB_{JHB}	Estimated visibility using the best
OWC	Optical Wireless Communication	VCD	MLR model for Johannesburg [km]
<i>p</i> -value <i>R</i>	Probability value Correlation coefficient	VSB_{KIM}	Estimated visibility using the best MLR model for Kimberley [km]
R^2	Coefficient of Determination	VSB_{M}	Measured visibility [km]
R_m^2	Coefficient of determination (R ²)	VSB_{MPU}	Estimated visibility using the best
κ_m	obtained by regressing the m^{th}	· ~ - MI U	MLR model for Mpumalanga [km]
	predictor on the remaining predictors	VSB_{PE}	Estimated visibility using the best
	in an MLR model		SLR model for Port Elizabeth [km]
R_{FSH}^2	Coefficient of determination obtained	VSB_{POL}	Estimated visibility using the best
	by regressing FSH on the RH and WS	Lian	MLR model for Polokwane [km]
2	independent variables Coefficient of determination obtained	VSB_{RH}	Estimated visibility from the <i>RH</i>
R_{RH}^2	by regressing <i>RH</i> on the <i>FSH</i> and <i>WS</i>	$VSB_{RH\&FSH}$	predictor variable [km] Estimated visibility using the MLR
	independent variables	V SD _{RH&FSH}	model containing the <i>RH</i> and <i>FSH</i>
R_{WS}^2	Coefficient of determination obtained		predictor variables [km]
KWS	by regressing WS on the RH and FSH	VSB_{RH+WS}	Estimated visibility using the MLR
	independent variables		model containing interaction terms
RF	Radio Frequency		RH+WS and the FSH predictor
RH	Relative humidity [%]	LIGD	variable [km]
RMSE	Root Mean Square Error	VSB_{RH-WS}	Estimated visibility using the MLR
SAWS SE	South African Weather Service Standard Error		model containing interaction terms <i>RH-WS</i> and the <i>FSH</i> predictor
SLR	Simple Linear Regression		variable [km]
tStat	t-statistic	VSB_{Temp}	Estimated visibility from the <i>Temp</i>
Тетр	Temperature [°C]	Temp	predictor variable [km]
U_b	Upper bound term	VSB_{WS}	Estimated visibility from the WS
UWB	Ultra-Wide Band	2	predictor variable [km]
VIF	Variance Inflation Factor	σ^2	Variance
VIF_{FSH}	Variance inflation factor obtained by	Wi-Fi	Wireless fidelity
	regressing FSH (output) on RH and WS	WiMAX	Worldwide Interoperability for Microwave Access
VIF_{RH}	Variance inflation factor obtained by	WS	Wind speed [m/s]
VII KH	regressing <i>RH</i> (output) on <i>FSH</i> and	x_i	Independent variable
	WS	x_{im}	m th Independent variable of an MLR
VIF_{RH+WS}	Variance inflation factor obtained by		model
	regressing RH+WS (output) on FSH	\overline{x}	Sample means of random variable X
VIF_{RH-WS}	Variance inflation factor obtained by	X	Independent variable of an MLR
· · · · · · · · · · · · · · · · · · ·	regressing <i>RH-WS</i> (output) on <i>FSH</i>		model in vectorized form
VIF_{WS}	Variance inflation factor obtained by	y_i	Output/dependent variable
	regressing WS (output) on RH and FSH	$\frac{\hat{y}_i}{\overline{y}}$	Estimate of y_i
$VIF_{FSH imes WS}$	Variance inflation factor obtained by	\overline{y}	Sample means of random variable \mathbf{Y}
rsH×W5	regressing $FSH \times WS$ (output) on RH	Y	Output/dependent variable of an
	5 6		MLR model in vectorized form

3G Third generation
4G Fourth generation
5G Fifth generation

I. Introduction

The ever-increasing variety of bandwidth-intensive mobile applications has led to an unprecedented rapid growth of the internet. This kind of growth may especially be attributed to the Internet of Things (IoT) technologies that have revolutionized the extent to which a massive number of devices are connected in a network. Through a unique addressing scheme, these devices are capable of interacting as well as cooperating amongst themselves to accomplish intended tasks [1]. The number of connected devices to the internet is expected to continue to surge upwards over time. Currently, promising solutions to support such growing demand in connectivity is through the fifth generation (5G) wireless communication systems where millimetre wave (mmwave) as well as Massive Multiple-Input Multiple-Output (M-MIMO) antenna technologies are to be integrated. However, due to strict regulations in the usage of the Radio Frequency (RF) spectrum, the transmission rates for mobile technologies operating in the RF spectrum are limited by the available RF spectrum. Some of the operational standards include Wi-Fi (IEEE 802.11), UWB (IEEE 802.15), WiMAX (IEEE 802.16), iBurst (IEEE 802.20), and the cellular based 3G and 4G [2]. To date, the capability to support numerous service requirements in order to realize elastic and ubiquitous connectivity remains a major challenge [3]. Ideally, a convergent, cost-effective, and pervasive network penetration for the Next-Generation Network (NGN) is required. However, Optical Wireless Communication (OWC) systems may be deployed as an alternative solution to the spectrum limitation [23]. OWC is an attractive broadband access technology that offers high data rates as well as improved capacity. Therefore, OWC can attend to some of the bandwidth requirements of numerous applications and services of the NGNs cost effectively [2], [4].

A terrestrial OWC system, as is with any communication system, consists of the transmitter, the channel, and receiver. The focus of this work will only be on the free space as a channel. The performance of a communication system is highly dependent on the channel condition, and the effective design of the communication system depends on the understanding of that channel. The optical field produced at the transmitter is radiated through the atmospheric channel to the receiving end. Due to the resultant effects of scattering and absorption (wavelength-dependent) introduced by the molecular structure and atmospheric aerosols along the transmission path, transmission loss occurs. In this light, this paper aims to utilize meteorological parameters to estimate meteorological visibility of a radiated optical field. Visibility is a key parameter in determining the attenuation of optical signals. By definition, it is perhaps

logical to precede with an intuitive analogy of visibility in terms of eyesight. In this way, it is defined as the meteorological optical range defining how far away objects may be seen under certain conditions (snow, fog, rain etc.). In other words, there is a certain contrast ratio threshold below which an observer cannot discern the difference between light and dark objects. In the case of free space optical receivers, the threshold contrast ratio is analogous to receiver sensitivity i.e. how long can the optical beam travel before it is "invisible" to the optical receiver. Generally, visibility is measured in airports at visible wavelengths over long periods of time. Even though commercial FSO systems use Infra-Red (IR) wavelengths, their propagation is quite similar to those of visible wavelength with an added advantage that they have improved penetration. The significance of this assertion lies in the fact that available visibility data are measured at visible wavelengths, therefore predictions made off of this data cannot in anyway undermine the effects of atmospheric conditions on optical propagation.

Atmospheric visibility studies are common in the environmental sciences fraternity (global warming, climatology etc.), with its greater application in the aviation industry and to some extent in generating automated warnings for motorists during adverse weather conditions [5]. It has been found in several research work [6], [7] that visibility has a strong relationship with numerous meteorological factors such as temperature, relative humidity and fractional sunshine. These relationships are typically obtained through simple linear regression analysis. In [8], however, they have extended the simple regression models to incorporate several parameters in one regression analysis to obtain a multiple regression model. Throughout these works, the focus of [8]-[13] were on the performance of the models which in turn informed their choice of best or acceptable models.

This was done through standard statistical tests such as the coefficient of determination, R^2 , root mean square error, RMSE, mean bias error, MBE and mean percentage error, MPE. In this paper, a thorough regression analysis is presented suitable for free space optical communications. In our view, prior research work available in literature is not suitable for optical communication system design as it lacks statistical value.

Firstly, as mentioned before, the focus of the modeling technique in previous works is on the accuracy of the model instead of its statistical power. The risk of such an approach lies in the fact that a model can perform well for a given sample of a population, but may not do so if a different sample is selected. In this work, this deficit is addressed by testing the significance of model parameter coefficients before a conclusion is made about its suitability. Secondly, in the multiple regression model, there is a strong evidence of multicollinearity observable from the results of [8]-[13]. In the presence of multicollinearity, the statistical power of the model is lost making it difficult to specify the correct model. In this work, multicollinearity is investigated and mitigated for it to improve the usefulness of the model. The

performance of each model is then assessed and some conclusions drawn.

The rest of the paper is organized as follows. Section II presents the methodological approach used in model validation and acknowledges the data source. The regression analysis and modeling is introduced in Section III with simple linear regression and its extension to multiple linear regression discussed in Section IV.

Visibility is estimated in Section V using MLR and its performance is compared to those of SLR. The evident effects of multicollinearity are assessed in Section VI and quantified through the variance inflation factor which are then mitigated for in Section VII. The general findings are presented in Section VIII through the discussion of results while Section IX provides the conclusion.

II. Data and Methodology

This research work is a case study of a warm-summer Mediterranean climatic region of Cape Town, South Africa. Its climatic profile is characterized by warm and dry summers with mean monthly temperatures not exceeding 22 °C during the warmest month. During the coldest month, average temperatures range between -3 °C and 18 °C with mild to chilly rainy weather experienced in winter, sometimes accompanied by snowfall. Similar climatic conditions are prevalent in Spain, Portugal, western Washington, central Chile, southern Australia etc. Mediterranean climatic regions experience between 2650 to 3400 hours of sunshine annually with a yearly average solar radiation of up to 3200 kWh/m² [14]-[17].

The average monthly visibility for an eight year period starting from January 2010 to December 2017 for Cape Town were provided by the South African Weather Services (SAWS). The same source provided data for other meteorological parameters used in this work i.e. relative humidity, temperature, sunshine hours, atmospheric pressure and wind speed spanning the same time period as well. The measured data is populated as monthly averages over the measurement period and used in the modeling process. The relationship between visibility and the aforementioned meteorological parameters is described using linear regression models.

The statistical significance of the regression model coefficients is tested by means of the t-test for zero-slope correlation coefficients coefficients. All appropriately tested by computing the coefficient of determination, R^2 . Moreover, the extent to which multicollinearity is present was tested through Variance Inflation Factors (VIF). As a rule of thumb, a VIF more than 5 is considered a strong indication of multicollinearity and a reason for concern. To show the significance/uncertainty of the regression coefficients, a 5% significance level was used as a benchmark against the *p*-values of the estimated model coefficients.

III. Simple Linear Regression (SLR) Model

Simple linear regression is a statistical technique

through which a relationship between two quantitative variables can be studied and summarized. In its structure, one variable is the outcome (dependent) while the other is the independent (predictor) variable. The adjective "simple" is derived from the fact that the model is only concerned with a single independent variable (IV). The extension of this treatment to two or more IVs is referred to as multiple linear regression, which will be discussed later in the paper. In a Simple Linear Regression model (SLR), the relationship between an output variable *y* and an independent variable *x* can be illustrated based on the regression equation of the form

$$y_{i} = \beta_{0} + \beta_{1} x_{i} + \epsilon_{i}$$

$$i = 1, 2, 3, ..., n$$
(1)

where β_0 is the intercept and β_1 is the slope parameter. By applying the least squares technique, the line of best fit can be determined by minimizing the sum of the squares of the difference between the observed data points and the corresponding fitted data values provided by the model. In general, the actual observation y_i is predicted by the best fit line as follows:

$$\hat{\mathbf{y}}_i = b_0 + b_1 \mathbf{x}_i \tag{2}$$

where b_0 and b_1 are the estimates of β_0 and β_1 , respectively. Before application of the SLR model to a dataset, it is necessary to evaluate its appropriateness.

The suitability of the model relies on considering several underlying assumptions about the population prediction errors as being reasonable. Under these assumptions, all subsequent tests, confidence intervals, and hypothesis tests that arise in the regression analysis assume that the model is appropriate. Without a proper validity of the model correctness, all the formulas and methodologies used going forward are of little use in the prediction process and model consistency. The application of SLR models assumes the following:

- The mean of the response variable, $E(y_i)$, for each value of the IV, x_i , is a linear function of x_i ;
- The errors, \in_i , are independent;
- The errors, ∈_i, for each value of the IV, x_i, are normally distributed;
- The errors, \in_i , for each value of the IV, x_i , have equal variances.

The conditions stated above may collectively be summarized to describe the errors as independent, normal random variables with zero mean, $E(\in_i) = 0$ and constant variance, σ^2 . The unknown actual error terms, $\in_i = y_i - E(y_i)$ may be estimated through the residual terms, $e_i = y_i - \hat{y}_i$, which is simply the difference between the observed data point y_i and the corresponding estimated value \hat{y}_i . In this work, meteorological data measured in Cape Town is used to estimate visibility in

Copyright © 2020 Praise Worthy Prize S.r.l. - All rights reserved

FSO communication systems that may be deployed at the location. The atmospheric parameters available for this study are temperature, relative humidity, atmospheric pressure, wind speed and fraction of sunshine hours. The latter simply describes the ratio between the actual amount of sunshine hours in a day (n) and the maximum possible amount of daylight hours (N). By regressing the measured visibility on these five parameters, linear relationships are developed with varied degrees of linearity and significance of coefficients, β_0 and β_1 . The fitted models for each IV are obtained as follows:

$$VSB_{RH} = 76.3846 - 0.7178 \times (RH) \tag{3}$$

$$VSB_{Temp} = 11.7201 + 0.7965 \times (Temp)$$
 (4)

$$VSB_{FSH} = 0.3530 + 35.8031 \times (FSH)$$
 (5)

$$VSB_{AP} = 878.7786 - 0.8435 \times (AP)$$
 (6)

$$VSB_{WS} = 10.0958 + 2.9664 \times (WS) \tag{7}$$

where RH is the relative humidity in %, Temp is the temperature in °C, FSH is the fractional sunshine hours (n/N), AP is the atmospheric pressure in mb and WS is the wind speed in m/s. VSB_{RH} , VSB_{Temp} , VSB_{FSH} , VSB_{AP} , and VSB_{WS} are estimated visibilities in km from each of the SLR models with IVs: RH, Temp, FSH, AP and WS respectively. In order to assess the normality of the actual error terms, the residuals $\left(y_i - \hat{y}_i\right)$ are obtained and their probability plotted. The idea is to visually assess whether the residuals come from a population with a normal distribution. If the residuals have a normal distribution, then it is expected that they will appear along a reference line with little to no indication of curvatures in the plot.

The probability of residuals obtained from all the five models are plotted in Fig. 1. In all the five cases, there is visually no indication for concern in terms of normality as the residuals satisfactorily hugs the reference line. The other condition required for the application of SLR models is that the error terms have a uniform variance, σ^2 . By plotting the error bars alongside the predicted model, the error variance can be observed along the best fit line as shown in Fig. 2. It is observed, in all five models, that there are data points whose error variance differs significantly from others (at most three data points), e.g. \in_3 , \in_5 of the Temp-based model. However, this is not enough to suggest that the error variance in general is not uniform since most of the data points exhibit relatively constant error variance. performance of each model is shown in Table I through V in terms of the Root Mean Square Error (RMSE), correlation coefficient (R) and p-value. The p-value gives indication on the hypothesis that the model is significant or otherwise at a specific % confidence level. Perhaps more important than the accuracy of the model is the significance of the model parameters used in the prediction process.

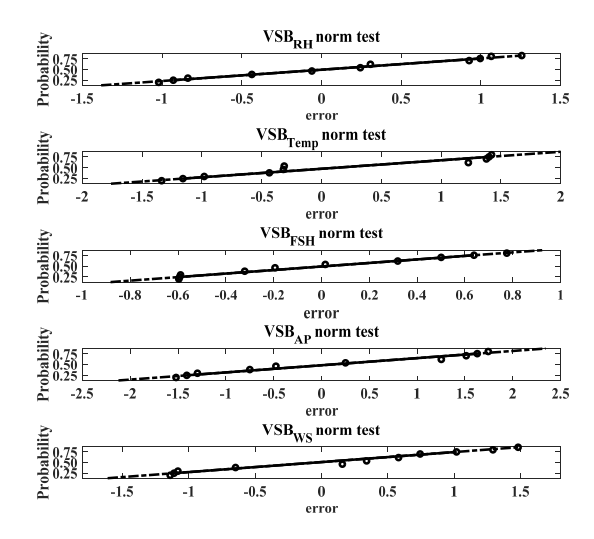


Fig. 1. Normality test for all the IVs

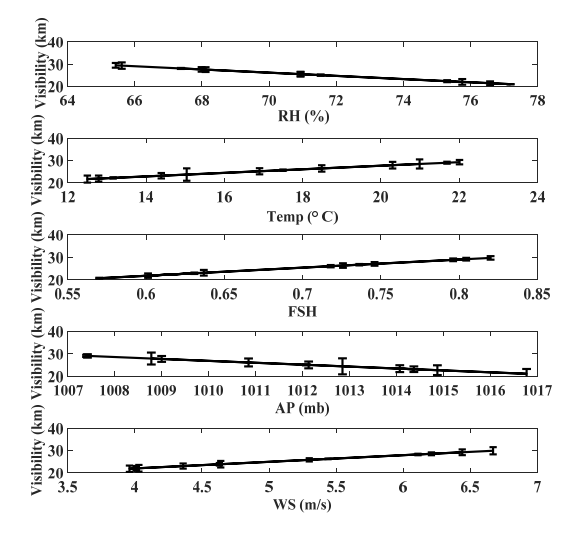


Fig. 2. Error bars for variance test for all the IVs

In general, for linear regression models, it is often useful to determine the t-statistic in order to make sound inferences with regards to the regression coefficients. A hypothesis test is performed on each coefficient j for the null hypothesis that it is equal to zero i.e. the corresponding model term is insignificant - against the alternative that it is different from zero. By definition, a hypothesis test on coefficient j, with $H_0:B_j=0$ and $H_1:\beta_j\neq 0$, the t-statistic is given by:

$$tStat = \frac{b_j}{SE(b_j)}$$
 (8)

where $SE(b_j)$ is the standard error of the estimated coefficient b_j . It can be seen from Tables I-V that tStat=Estimate/SE for all estimated coefficients. Since each model consists of two terms, the independent variable and the constant, the t-statistic tests for the significance of each term in the presence of the other.

Considering the model derived from FSH, the intercept term is not significant at 5% significant level as

Copyright © 2020 Praise Worthy Prize S.r.l. - All rights reserved

indicated by its p-value of 0.8542 which is greater than 0.05. However, both terms of the models derived from RH, Temp, AP and WS are significant at 5% significant level. In terms of model performance, the FSH-based model easily outperforms the other four having the highest correlation coefficient, lowest RMSE, and smallest p-value as shown in Table I through V. The RHbased model follows secondly, outperforming the *Temp*-, AP- and WS-based models across all the three metrics. Before making a decision on the best model in the prediction of visibility, the issue of an insignificant predictor under the FSH-based model is re-visited. In view of the fact that the intercept term is not a predictor variable, there is no specific hypothesis regarding its usefulness so it might be best to exclude it in order to simplify the model. One further advantage of leaving out an insignificant term is that an extra degree of freedom is gained, which is valuable considering the small number of samples (Ns = 12). The *FSH*-based model will now be reduced to simply $y_i = \beta_1 x_i + \epsilon_i$. After regressing visibility on FSH with β_0 =0, it turns out that there is little change in the model performance in terms of the correlation coefficient, R=0.9741 compared to the previous R=0.9735. More impressively, the significance of the FSH coefficient has improved a great deal as indicated by a t-statistic value of 120.02 compared to the previous 13.47. This is a culmination of reduced standard error in the estimation of the FSH coefficient, previously at SE=2.66 and currently at SE=0.30. This indicates an almost ten-fold reduction in the standard error in estimating β_1 . Thus, in the adjusted model, the expected variance in the β_1 coefficient has significantly been reduced and this improves the model consistency.

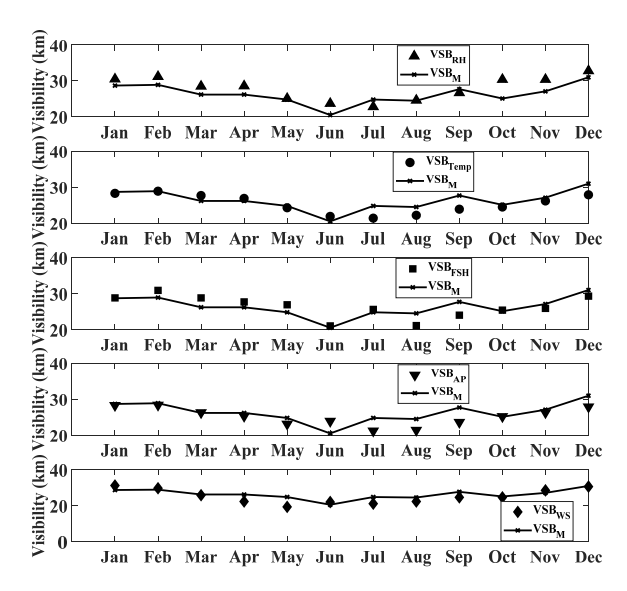


Fig. 3. Measured and estimated visibility for all IVs

TABLE I SLR_{RH} ESTIMATED COEFFICIENTS

SLNRH ESTIMATED COEFFICIENTS				
	Estimate	SE	tStat	<i>p</i> -value
Intercept	76.3846	4.9871	15.3165	2.8601×10 ⁻⁸
RH	-0.7178	0.0701	-10.2451	1.2726×10^{-6}
Model	RMSE=0.995	R=0.9555	<i>p</i> -value	=1.3×10 ⁻⁶

	SERTEMF ESTIMATES COEFFICIENTS				
	Estimate	SE	tStat	<i>p</i> -value	
Intercept	11.7201	2.3550	4.9767	0.0006	
Temp	0.7965	0.1347	5.9124	0.0001	
Model	RMSE =1.5913	R=0.8818	<i>p</i> -value	$=1.5\times10^{-4}$	

TABLE III SLR_{ESH} ESTIMATED COEFFICIENTS

	Estimate	SE	tStat	<i>p</i> -value
Intercept	0.353	1.8715	0.1886	0.8542
FSH	35.8031	2.6587	13.4665	9.8104×10^{-8}
Model	RMSE=0.771	R=0.9735	<i>p</i> -valu	e=9.8×10 ⁻⁸

TABLE IV

SLR _{AP} ESTIMATED COEFFICIENTS						
	Estimate SE tStat p-value					
Intercept	878.7786	199.6018	4.4027	0.0013		
AP	-0.8435	0.1973	-4.2755	0.0016		
Model	RMSE=2.006	R=0.8040	<i>p</i> -value=	=1.6×10 ⁻³		

TABLE V
SLRws ESTIMATED COEFFICIENTS

	Estimate	SE	tStat	<i>p</i> -value
Intercept	10.0958	1.8815	5.3658	3.1642×10 ⁻⁴
WS	2.9664	0.359	8.264	8.8506×10^{-6}
Model	RMSE=1.206	R=0.9340	<i>p</i> -val	ue=1.6×10 ⁻³

IV. Multiple Linear Regression (MLR) Model

The goal of any regression technique is to model the relationship between the independent (explanatory/regressors) and the dependent (response) variables. Multiple Linear Regression (MLR) is one such approach that uses several independent variables to predict the outcome of a dependent variable [24]. This, in contrast with a simple linear regression technique in which only two continuous variables are available - an independent variable and a dependent variable, employs rather multiple continuous independent variables to predict a single outcome. In its structure and formulation, it is similar to a simple linear regression except that the linear fit is a plane that cuts through several planes. A multiple regression model is obtained by extending this interpretation to a scenario wherein multiple regressors exist. In such an environment, the dependent variable is related to two or more independent variables. In general, for m variables it takes the form:

$$y_{i} = \beta_{0} + \beta_{1}x_{i1} + \beta_{2}x_{i2} + \dots + \beta_{m}x_{im} + \epsilon_{i}$$

$$i = 1, 2, \dots, n$$
(9)

where β_0 is the intercept. β_j [j=1,2,...,m] are the regression coefficients that measures the unit change in the dependent variable in response to a change in the independent variables. Here ϵ_i represents the random error term and it is assumed to be normally distributed with mean 0 and constant variance σ^2 i.e. $\epsilon_i \sim N(0,\sigma^2)$.

The expression in (9) may be presented in a more compact form by using the matrix framework. It is

Copyright © 2020 Praise Worthy Prize S.r.l. - All rights reserved

straightforward that (9) can be re-written in the vectorized form:

$$Y = X \beta + \epsilon \tag{10}$$

which can be written in the matrix form:

$$\begin{bmatrix} y_1 \\ y_2 \\ \vdots \\ y_n \end{bmatrix} = \begin{bmatrix} 1 & x_{11} & \cdots & x_{1m} \\ 1 & x_{21} & \cdots & x_{2m} \\ \vdots & \vdots & \ddots & \vdots \\ 1 & x_{n1} & \cdots & x_{nm} \end{bmatrix} \begin{bmatrix} \beta_0 \\ \beta_1 \\ \vdots \\ \beta_m \end{bmatrix} + \begin{bmatrix} \epsilon_1 \\ \epsilon_2 \\ \vdots \\ \epsilon_n \end{bmatrix}$$

where *Y* is an $n \times 1$ dimensional random vector containing observations, *X* is an $n \times (m \times 1)$ matrix determined by the regressors, β is an $(m+1)\times 1$ vector of parameters to be determined, and ϵ is an $n \times 1$ vector of random errors.

When performing MLR analysis, the regression coefficients of (9) are estimated using the least squares method. These coefficients provide information about the unrelated contributions pertaining to each regressor variable towards predicting the outcome variable.

Contrary to simple linear regression, the degree of correlation between pairs of regressor variables must be inferred.

V. Estimation of Visibility Using MLR

It has been shown in previous research contributions [6]-[8], as it shall also be done here, that visibility can be estimated from several meteorological factors. Factors such as Relative Humidity (*RH*), temperature (*Temp*), Fractional Sunshine Hours (*FSH*), Atmospheric Pressure (*AP*) and Wind Speed (*WS*) have been shown to have a strong relationship with visibility and have thus been utilized in its prediction. In this work, data spanning a period of eight years is used to facilitate the prediction process. In the development of the MLR model, reference will be made to the simple linear regression models based on each of the aforementioned five IVs for comparison and completeness. Similar to SLR, in its application, MLR takes the following assumptions:

- The mean of the response variable, $E(Y_i)$, for each regressor value set $(x_{i1}, x_{i2}, ..., x_{im})$ is a linear function of the regressors;
- The errors, \in_i , are independent;
- The errors, \in_i , for each regressor value set $(x_{i1}, x_{i2}, ..., x_{im})$, are normally distributed.
- The errors, \in_i , for each regressor value set $(x_{i1}, x_{i2}, ..., x_{im})$, have equal variances.

In summary, these assumptions may be understood to describe a process whose error terms are independent, normally distributed, random with zero mean and constant variance. Verifying the validity of the assumptions for a multiple regression model in a comprehensive manner is not a trivial task, however, the thoroughness with which this is done speaks to the

confidence that can be placed on the model. As observed in Section III, the errors generated by regressing visibility on *RH*, *Temp*, *FSH*, *AP* and *WS* are fairly random, independent and normally distributed. In extension to this view, the errors generated by applying MLR is expected to be random, independent and normally distributed as well. The MLR model for estimating visibility is determined to be:

$$VSB_{ALL} = 35.6326 - 0.3540(RH)$$

+23.6978(FSH) - 0.3219(WS) (11)

The performance of the MLR model in (11) is summarized in Table VI. Clearly this model outperforms the SLR models presented in Section III in terms of the correlation coefficient, R = 0.9915, and RMSE = 0.4915.

However, further analysis of the model reveals that the WS predictor term of the model is not significant at 5% significant level. The p-value for the WS term is 0.5233.

In summary, the MLR model has significantly improved the model accuracy but has also drastically increased the standard error in the prediction of the model coefficients. The increased variance in the estimation of model coefficients makes it difficult to comprehend the effects of individual predictors towards observed changes in visibility. Ultimately, there is a limited research conclusion that can be drawn from the model. With a quick glance at equations (3)-(7) in conjunction with (11), it can be seen that there is an increased variance in the coefficient estimates i.e. minor changes in the model can result in highly sensitive estimates.

Two observations are notable: 1) The significance of wind speed in the prediction of visibility has diminished greatly in MLR compared to SLR. 2) there is a direct proportional relationship between wind speed and visibility when using SLR, while the relationship is inversely proportional when using MLR (the sign has been reversed). This is an indication that the expected value of visibility for a change in each predictor is not a linear function of the changes in the predictors. Simply put, in the MLR model, the change in visibility cannot be attributed to a change in a single predictor whilst holding others constant. Thus, the linearity assumption is violated.

Theoretically, it is reasonable to assume that the issues raised above may partly be due to the fact that the IVs are related to one another in some way. It is expected that the meteorological factors be related to each other at a given location, giving rise to the phenomenon of multicollinearity.

TABLE VI MLR ESTIMATED COEFFICIENTS

	Estimate	Standard Error	tStat	<i>p</i> -value
Intercept	35.6326	9.3473	3.8121	0.0051
RH	-0.3540	0.0972	-3.6422	0.0066
FSH	23.6978	4.6715	5.0728	0.0010
WS	-0.3219	0.4823	-0.6673	0.5233
Model	RMSE=0.4915	R = 0.9915	<i>p</i> -value	$=2.0294\times10^{-7}$

Copyright © 2020 Praise Worthy Prize S.r.l. - All rights reserved

VI. Multicollinearity of Visibility Predictors

Multicollinearity is a phenomenon that arises due to having two or more predictors in a regression model with a moderate or high degree of correlation.

Its presence reduces the precision of the estimate of coefficients, which weakens the statistical power of the regression model.

In the presence of multicollinearity, the significance of some predictors may be diminished making it difficult to determine the role of each predictor.

Assuming that multicollinearity exists, the critical question is: to what extent are the IVs correlated?

Conceptually, the idea is to figure out if any of the predictors measure the same or similar construct. The dependence between multiple variables can be evaluated by computing a correlation matrix. In this work, the correlation analysis has been performed using Pearson's parametric correlation test.

In its application, the correlation coefficient, R, between two random variables \mathbf{X} and \mathbf{Y} with n series of measurements sampled such that they are presented in the form x_i and y_i for i=1,2,3,...,n, then the sample correlation coefficient may be used to estimate the population correlation between \mathbf{X} and \mathbf{Y} . The sample correlation coefficient is calculated as:

$$R = \frac{\sum_{i=1}^{n} (x_i - \overline{x})(y_i - \overline{y})}{\sqrt{\sum_{i=1}^{n} (x_i - \overline{x})^2 (y_i - \overline{y})^2}}$$
(12)

where \overline{x} and \overline{y} are the sample means of **X** and **Y**, respectively. For a given system of study with n random variables M_1, \ldots, M_n , its correlation matrix is an $n \times n$ matrix whose i,j entry represents $corr(M_i, M_j)$. It is common practice to create a graphical display of the correlation matrix, this can be done using the statistical toolbox in MATLAB. The plot shows correlations among pairs of variables in M. The scatter plots of variable pairs appear in the off diagonal while the histograms of the variables appear along the diagonal.

The least squares method is used to determine the best fit line between variables with correlation coefficients also displayed on each graph pair as shown in Fig. 4. The correlation coefficients, R (extracted into the R-matrix below), indicate which pairs of variables have correlations significantly different from zero. The significance of the correlations are determined by calculating the p-values for each variable pair and displayed as p-matrix below:

$$R = \begin{bmatrix} VSB & RH & Temp & FSH & AP & WS \\ VSB & 1.0000 & -09554 & 0.8819 & 0.9735 & -0.8041 & 0.9339 \\ RH & -0.9554 & 1.0000 & -0.8060 & -0.8976 & 0.7397 & -0.9297 \\ Temp & 0.8819 & -0.8060 & 1.0000 & 0.9480 & -0.9804 & 0.9144 \\ FSH & 0.9735 & -0.8976 & 0.9480 & 1.0000 & -0.8842 & 0.9264 \\ AP & -0.8041 & 0.7397 & -0.9804 & -0.8842 & 1.0000 & -0.8900 \\ WS & 0.9339 & -0.9297 & 0.9144 & 0.9264 & -0.8900 & 1.0000 \\ \end{bmatrix}$$

$$p = \begin{bmatrix} VSB & RH & Temp & FSH & AP & WS \\ VSB & 1.0000 & 0.0000 & 0.0001 & 0.0000 & 0.0016 & 0.0000 \\ RH & 0.0000 & 1.0000 & 0.0015 & 0.0001 & 0.0060 & 0.0000 \\ Temp & 0.0001 & 0.0015 & 1.0000 & 0.0000 & 0.0000 & 0.0000 \\ FSH & 0.0000 & 0.0001 & 0.0000 & 1.0000 & 0.0001 & 0.0000 \\ AP & 0.0016 & 0.0060 & 0.0000 & 0.0001 & 1.0000 & 0.0001 \\ WS & 0.0000 & 0.0000 & 0.0000 & 0.0000 & 0.0001 & 1.0000 \\ \end{bmatrix}$$

Evidently, the output pairwise p-values are all less than 5% significant level, indicating that all pairs of variables have correlations significantly greater than zero. That is, there is a fairly strong linear relationship between the predictor variables. For example, AP and Temp are strongly correlated (R=-0.9804), while RH and AP are moderately correlated (R=0.7397). It may not be adequate to assess the severity of multicollinearity in a regression analysis by analysing the correlation coefficients, usually, a Variance Inflation Factor (VIF) is used. This factor is the ratio between the variance of a predictor in a model with multiple predictors and the

variance of the predictor in a model with a single term [18]. It basically quantifies the extent to which the variance is inflated, as the name suggests. Considering a model in which x_m is the only outcome predictor (as in the SLR case in (1)), it can be shown that the variance of the estimated coefficient b_m is given by:

$$\sigma^{2}(b_{m}) = \frac{\sigma^{2}}{\sum_{i=1}^{n} \left(x_{im} - \overline{x}\right)^{2}}$$

$$(13)$$

Copyright © 2020 Praise Worthy Prize S.r.l. - All rights reserved

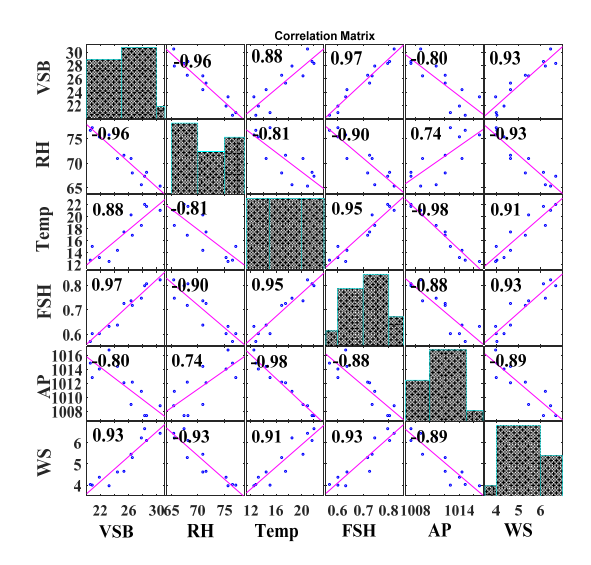


Fig. 4. Correlation Matrix for Visibility and all the IVs

In a multiple linear regression model where multicollinearity is present, such as in (9), the variance of b_m is inflated. The inflated variance can be calculated as:

$$\sigma^{2}(b_{m}) = \frac{\sigma^{2}}{\sum_{i=1}^{n} (x_{im} - \overline{x})^{2}} \times \frac{1}{1 - R_{m}^{2}}$$
(14)

where R_m^2 is the coefficient of determination (R^2) obtained by regressing the m^{th} predictor on the remaining predictors. According to (14), the higher the correlation between predictor x_{im} and the other predictors, R_m^2 , the greater the variance of b_m . By taking the ratio of the two variances, the proportion of inflation can be determined.

Thus, VIF is found as follows:

$$\sigma^{2}(b_{m}) = \frac{\frac{\sigma^{2}}{\sum_{i=1}^{n} (x_{im} - \overline{x})^{2}} \times \frac{1}{1 - R_{m}^{2}}}{\frac{\sigma^{2}}{\sum_{i=1}^{n} (x_{im} - \overline{x})^{2}}} = \frac{1}{1 - R_{m}^{2}}$$
(15)

For all the m predictors available in the MLR model there exists a corresponding variance inflation factor. The objective is to determine the extent of "inflation" on the variance of the estimated regression coefficient b_m as a result of correlation among predictor variables. It is straightforward from (15) that a VIF of 1 indicates no correlation between the m^{th} predictor and the rest of the predictor variables, thus, the variance of b_m is not inflated at all. There is no general agreement on the interpretation of VIF, but the general rule of thumb is that a VIF exceeding 5 warrants further investigation [19] while those in excess of 10 signifies serious multicollinearity [20]. These require correction for meaningful model

interpretation. By regressing WS, FSH and RH on the remaining two variables at a time, the VIF for each predictor variable can be calculated using (15). The results are shown in Table VII. The coefficient of determination for WS, RH and FSH are, $R_{WS}^2 = 0.908$, $R_{RH}^2 = 0.873$ and $R_{FSH}^2 = 0.869$ respectively. As shown in Table VII, their corresponding VIFs are 10.87, 7.89 and 7.60 respectively. The VIFs for WS, RH and FSH are fairly large. By interpretation, for example, the VIF for WS indicates that the variance of the estimated coefficient b_{WS} of predictor WS is inflated by a factor of 10.87. It follows then that the estimated coefficients of RH (b_{RH}) and FSH (b_{FSH}) are inflated by factors of 7.89 and 7.60, respectively.

VII. Mitigation for Multicollinearity

It has been shown in the analysis of the MLR model of (11) that the model exhibits signs of multicollinearity.

Furthermore, it has been ascertained through the evaluation of variance inflation factors that indeed the model has cases of multicollinearity among some of the predictor terms. The objective of modeling visibility with meteorological factors is to obtain a model which is easy to interpret with stable coefficients and statistical significance. The presence of multicollinearity makes it difficult to specify the correct model. In the following sub-sections two approaches are proposed to deal with the effects of multicollinearity.

VII.1. Removing Highly Correlated Predictors

Based on the results obtained in Section VI and equation (15), it is straight forward that the value of VIF can be reduced by removing one of the highly correlated predictor pairs from the model. Using the guidelines provided in Section VI and the results in Table VII, the severe multicollinearity effects involving WS (VIF = 10.87) need to be addressed (since it is above 10). By observing the correlation matrix plot in Fig. 4, further light is shed on which predictor pairs are highly correlated.

TABLE VII
DETERMINATION OF VARIANCE INFLATION FACTORS

	DETERMINATION OF VARIANCE INFLATION FACTORS				
	WS as output				
	Estimate	Standard Error	tStat	<i>p</i> -value	
Intercept	9.75147	5.58268	1.74674	0.11463	
RH	-0.11889	0.05425	-2.19149	0.05611	
FSH	5.50649	2.65601	2.07321	0.06801	
Model	RMSE=0.3397	$R^2 = 0.908$	VIF=	10.8696	
		RH as output			
	Estimate	Standard Error	tStat	<i>p</i> -value	
Intercept	94.90659	5.15379	18.41492	1.87844×10 ⁻⁸	
FSH	-12.53896	15.46406	-0.81085	0.43837	
WS	-2.92676	1.33551	-2.19149	0.05611	
Model	RMSE=1.6853	$R^2 = 0.873$	VIF=	=7.8927	
		FSH as output			
	Estimate	Standard Error	tStat	<i>p</i> -value	
Intercept	0.78240	0.61387	1.27453	0.23440	
RH	-0.00543	0.00670	-0.81085	0.43837	
WS	0.05870	0.02831	2.07321	0.06801	
Model	RMSE=0.0351	$R^2 = 0.869$	VIF=	=7.6046	

Copyright © 2020 Praise Worthy Prize S.r.l. - All rights reserved

It turns out that the three predictor variables which exhibit severe multicollinearity (WS, RH and FSH) in the MLR model are in fact highly correlated among themselves. The correlation coefficient (R) between the sets of WS & RH, WS & FSH and RH & FSH are -0.93, 0.93 and -0.90 respectively. As revealed in Table VI, the WS predictor term of the model is not significant at 5% significant level as the p-value for the WS term is 0.5233.

Therefore, removing the WS term from the model since it is insignificant and regressing visibility on FSH and RH, the model reduces to:

$$VSB_{RH\&FSH} = 32.4940 - 0.3158(RH) + +21.9255(FSH)$$
 (16)

The performance of model (16) is shown in Table VIII. It is evident from Table VIII that all the estimated coefficients for predictor variables included in the models are now significant at 5% significant level. The VIF criteria is used again to assess effects of multicollinearity.

It should be noted that for a model with only two predictor terms, the VIFs for the two predictors will be the same i.e. the same R^2 value is obtained after regressing one term on the other. In this case, VIF_{RH}=VIF_{FSH}=5.1467. It can be concluded that the effects of multicollinearity has been addressed adequately. Simply put, there is hardly any variance inflation present. Incidentally, the model accuracy does not seem to have been lost in terms of the R^2 value. In fact, the performance observed in Table VIII is slightly better than that of (11) as shown in Tables VI and VIII, respectively. The model in (16) has a slightly smaller RMSE (0.4761 vs 0.4915) as well as the *p*-value (by an order of 10), while the $R^2 = 0.98$ remains approximately equal.

VII.2. Introducing Interaction Terms

A linear combination of predictors is known to alleviate effects of multicollinearity. Even though *RH*, *WS* and *FSH* are not measured in the same way i.e. *RH* is measured as a percentage, *WS* in derived units while *FSH* is a ratio. As shown in Subsection VII.1, excluding highly correlated predictors may alleviate effects of multicollinearity.

However, it is also possible that such correlated predictors may have a complementary effect in determining the output variable. In this way, the two variables are combined into one variable. In this work, the meaningful interactions between RH, WS and FSH have been found to be RH+WS, RH-WS, and $FSH\times WS$.

TABLE VIII
MODELING WITHOUT HIGHLY CORRELATED PREDICTORS

MODELING WITHOUT HIGHLY CORRELATED PREDICTORS				
	Estimate	Standard Error	tStat	<i>p</i> -value
Intercept	32.4940	7.8250	4.1526	0.0025
RH	-0.3158	0.07604	-4.1530	0.0025
FSH	21.9255	3.7228	5.8895	0.0002
Model	RMSE=0.4761	$R^2 = 0.9821$	p-value=1.38	04×10^{-8}

The representative formulations are shown in (17) and (18) below.

$$y_{i} = \beta_{0} + \beta_{1}(x_{i1} \pm x_{i2}) + \beta_{2}x_{i3} + \epsilon_{i}$$
 (17)

and:

$$y_{i} = \beta_{0} + \beta_{1}(x_{i1} \times x_{i2}) + \beta_{2}x_{i3} + \epsilon_{i}$$
 (18)

In (17), x_{i1} and x_{i2} are the i^{th} elements of RH and WS while x_{i3} represent the i^{th} elements of *FSH*. On the other hand, x_{i1} and x_{i2} are the i^{th} elements of *FSH* and *WS* while x_{i3} represent the i^{th} elements of RH in (18). The results of these regressions are shown in Table IX. It can be observed that all the model term coefficients are significant at 5% significant level. Even though the model derived from the RH+WS interaction term slightly outperforms the other two in terms of regression standard errors, p-values and R^2 , all the models produce fairly similar results. Through visual inspection, there is no sign of multicollinearity since all the model terms are consistent with theoretical basis (significant with no sign reversals). This is also corroborated by the VIFs. By regressing the interaction terms on the remaining predictor, it is found that $VIF_{RH+WS}=3.9494$, $VIF_{RH-WS}=3.9494$ WS=6.0205, and $VIF_{FSH \times WS}$ =6.7431. The model with the RH+WS interaction term is also slightly preferred since its VIF=3.9494 is lesser than 5 while the other two VIFs are slightly higher than the threshold value of 5.

VIII. Discussion of Results

It has been established in this work that visibility can be accurately determined from several meteorological factors. In the first instance, simple regression analysis is used in the estimation of visibility using relative humidity, fractional sunshine, temperature, atmospheric pressure and wind speed. A multiple regression analysis is then introduced to take advantage of the variety of available meteorological factors. The results obtained are summarized in two parts, SLR models and MLR models.

TABLE IX
MODELING WITH INTERACTION TERMS INTRODUCED

		(RH+WS)		
	Estimate	Standard Error	tStat	<i>p</i> -value
Intercept	35.8690	8.2920	4.3257	0.0019
RH+WS	-0.3572	0.0826	-4.3231	0.0019
FSH	23.9390	3.1756	7.5385	3.5468×10^{-5}
Model	RMSE=0.4635	$R^2 = 0.9830$	<i>p</i> -value=	1.0852×10^{-8}
		(RH-WS)	•	
	Estimate	Standard Error	tStat	<i>p</i> -value
Intercept	28.4385	7.5419	3.7707	0.0044
RH-WS	-0.2697	0.0715	-3.7742	0.0044
FSH	21.0557	4.2788	4.9209	0.0008
Model	RMSE=0.5059	$R^2 = 0.9798$	<i>p</i> -value =	2.3847×10 ⁻⁸
		$(WS \times FSH)$	•	
	Estimate	Standard Error	tStat	<i>p</i> -value
Intercept	45.3112	11.7845	3.8450	0.0039
$FSH \times WS$	1.4625	0.5242	2.7898	0.0211
RH	-0.3561	0.1404	-2.5359	0.0319
Model	RMSE=0.7681	$R^2 = 0.9534$	<i>p</i> -value=	1.0224×10^{-6}

Copyright © 2020 Praise Worthy Prize S.r.l. - All rights reserved

VIII.1. SLR Models

As mentioned before, in a regression model it is desired to test the significance of the parameters included in the model. By testing for the significance of the parameter coefficients, a decision can be made regarding the significance of the parameter concerned. All the tests are performed at 5% significant level. In practical terms, it is not enough just to have information about the significance of parameters, generally there exists a hypothesis about the parameters. For example, it is expected that full sunshine hours (clear skies) result in increased visibility. Any result in the contrary merits further investigation as the model integrity may be compromised.

The 95% Confidence Interval (CI) for the model coefficients are presented in Table X to provide further insight into the model performance. The lower and upper bounds of the confidence interval are denoted L_b and U_b , respectively.

As shown in Table X, for the 95% confidence level the confidence interval for the intercept term, β_0 for *FSH* crosses the zero mark. Therefore, this makes it difficult to specify the direction of its effect. This behaviour is significant in the *FSH* model. As mentioned in Section III, the intercept term is not a predictor variable, therefore it might be reasonable to ignore it in the *FSH* model. By setting β_0 =0 in the *FSH* model, the reduced model will only consist of the *FSH* term. The regression now changes to what is commonly known as a regression through the origin (RTO). The confidence interval for the coefficient of *FSH*, β_{FSH} was found to be within [35.6 37.0].

Obviously the CI width for β_{FSH} has narrowed compared to that shown in Table X (with intercept). As stated in Section III, the model performance generally remains unchanged. However, this model might lack practical interpretation due to the inference that when FSH = 0, VSB = 0 as well. The difficulty of interpretation arises simply because there is no measurement recorded near FSH = 0.

VIII.2. MLR Models

In the presence of multiple meteorological factors, a multiple regression model is presented in Section V. By including all the three predictors (based on their high correlation with visibility) in the model, the regression results are shown in Table VI. The MLR model performed better than all the SLR models in terms of the Regression SE, R^2 , and p-value. In comparison, the model performance results can be seen in Table XI. The model containing all the predictor variables is denoted as MLR_{ALL} .

TABLE X
CONFIDENCE INTERVALS FOR SLR MODELS

	R	Н	FS	SH	WS	
CI	β_0	β_{RH}	β_0	β_{FSH}	β_0	β_{WS}
L_b	65.27	-0.87	-3.82	29.88	5.90	2.17
U_b	87.50	-0.56	4.52	41.73	14.29	3.77

 $TABLE \; XI \\ COMPARISON BETWEEN \; SLR \; AND \; MLR_{ALL} \; MODEL \\$

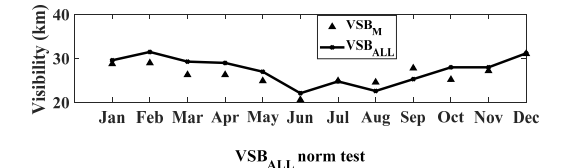
	RH	FSH	WS	MLR_{ALL}
RMSE	0.9951	0.7713	1.2058	0.4915
R^2	0.9130	0.9477	0.8723	0.9830
<i>p</i> -value	1.3×10 ⁻⁶	9.8×10^{-8}	8.85×10^{-6}	2.0294×10 ⁻⁷

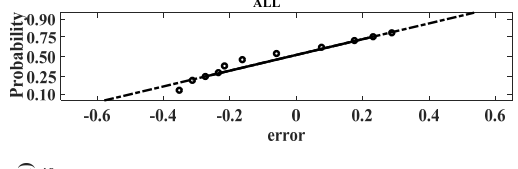
As in simple regression models, the objective is to reliably specify a model with some degree of confidence in the parameters included in the model. For any of the variables x_{im} included in the MLR model, the null hypothesis states that the coefficient β_m is not different from 0, with the alternative stating that β_m is significantly different from 0. The sensitivity of the coefficients of the MLR model parameters is quantified through the 95% confidence intervals. In Section VI, it was determined through the Variance Inflation Factor (VIF) that the estimated coefficient for WS (b_{WS}) is highly inflated. The same conclusion can be reached by observing the CI of the coefficients in question. As seen from Table XII, the expected mean value of this coefficient swing from negative to positive values, indicating its lack of significance. The lack of statistical significance in this model parameter makes it difficult to specify a reliable model due to the wide CI of the parameter coefficient.

The relatively low RMSE and high R^2 values may be applicable to specific samples and may not be representative of the overall data population. The performance of the MLR_{ALL} model is also shown in Fig. 5 against the measured data. In the same figure, the results of the normality test are shown. The error distribution does not indicate any significant deviation from the normality assumption. Fig. 5 also shows the performance of $VSB_{RH\&FSH}$ model (MLR model (16) after the removal of the WS predictor term) against measured data in the year 2017. The $VSB_{RH\&FSH}$ model contains the RH and FSH predictor terms alongside its intercept as depicted in Table VIII.

TABLE XII

CIs OF THE MLR _{ALL} MODEL COEFFICIENTS				
CI	βο	β_{RH}	β_{FSH}	β_{WS}
L_b	14.0776	-0.5782	12.9253	-1.4341
U_b	57.1876	-0.1299	34.4704	0.7904





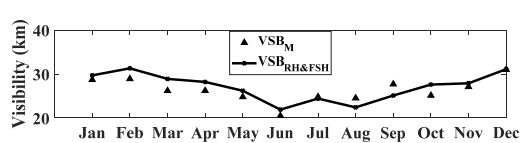


Fig. 5. MLR Model Including all the Predictors and the Error Normality Test

Copyright © 2020 Praise Worthy Prize S.r.l. - All rights reserved

VIII.2.1. MLR with Moderately Correlated Predictors

In Section VI, it was shown that the lack of model specificity in MLR may be due to a severe case of multicollinearity. By regressing each predictor term on the remaining ones, it was established through VIFs that indeed some parameters have strong linear relationships with others.

Specifically, it was found that WS and FSH are highly correlated (R=0.93).

The first approach in dealing with multicollinearity was to eliminate the redundant term in the model i.e. excluding *WS* from the final model.

The case where WS was eliminated was explored and the results are presented in Table VIII.

Overall, it was found that the issue of multicollinearity was adequately addressed without any loss in model precision. The confidence intervals of the model coefficients also show stability since they no longer cross the zero mark as depicted in Table XIII.

The performance of the model in which the highly correlated term WS is excluded is shown in Fig. 5. It can be seen that the model estimates the expected visibility satisfactorily throughout the year. In Table XIII, all the parameter coefficients of the model with FSH and RH have a narrower CI width than they had in MLR_{ALL} model shown in Table XII. The CI width of the intercept term, β_0 is ≈ 35 in Table XIII compared to ≈ 43 in Table XII while the coefficient of RH has a CI of ≈ 0.344 in Table XIII as opposed to ≈ 0.448 in Table XII. Also, β_{FSH} has a CI of ≈ 17 in Table XIII as opposed to ≈ 22 in Table XIII.

VIII.2.2. MLR with Interaction Terms

An alternative approach was presented in Subsection VII.2 which deals with effects of multicollinearity. It was shown therein that combining the highly correlated predictor terms in some way can alleviate the effects of multicollinearity in multiple regression model. In this case, the parameters of concern are RH, WS and FSH which have been shown to be highly correlated. By combining RH, WS and FSH new variables are generated, in this work, RH+WS, RH-WS, and $WS\times FSH$ are used. It is possible that other combinations may also work which include these basic terms in their formulation but in this work, these three are considered adequate for the Cape Town location.

The model parameter coefficients were tested at 5% significant level as well as by investigating their VIFs. In all cases the coefficients were found to be significant.

The confidence intervals for all the three models are shown in Table XIV. By observing the model parameter coefficient CIs, all the parameters included in all three models are significant.

TABLE XIII
CIS OF THE MLR MODEL COEFFICIENTS
WITHOUT CORRELATED PREDICTORS

			-
CI	β_0	β_{RH}	β_{FSH}
L_b	14.7927	-0.4878	13.5040
U_b	50.1953	-0.1438	30.3471

TABLE XIV
CISOF THE MLR MODEL COEFFICIENTS WITH INTERACTION TERMS

Model	β_0	β_I	β_{FSH}
RH+WS	$L_b = 17.1111$	$L_b = -0.5441$	$L_b = 16.7554$
KH+WS	$U_b = 54.6269$	$U_b = -0.1703$	$U_b = 31.1227$
RH - WS	$L_b = 11.3775$	$L_b = -0.4314$	$L_b = 11.3763$
KH - WS	$U_b = 45.4996$	$U_b = -0.1081$	$U_b = 30.7352$
Model	β_0	β_I	β_{RH}
$WS \times FSH$	$L_b = 18.6528$	$L_b = 0.2766$	$L_b = -0.6739$
WS×FSH	$U_b = 71.9696$	$U_b = 2.6483$	$U_b = -0.0384$

The performance of the models with interaction terms has been summarized in Table IX. The monthly estimation of average visibility throughout the year is shown in Fig. 6 using the models with interaction terms.

The measured visibility is denoted as VSB_M while the models with interaction terms are denoted VSB_{RH+WS} , VSB_{RH-WS} , and $VSB_{FSH\times WS}$ for RH+WS, RH-WS, and $FSH\times WS$ models, respectively. It can be seen from Fig. 6 that the regression models estimate visibility accurately throughout the year.

VIII.3. FSO Visibility

In the planning process for the deployment of FSO systems, visibility at a location is a key component for designers.

The available measured visibility data used in this work is based on a 5% threshold of the visible light. In other words, of the total transmitted signal, 95% is scattered and/or absorbed by the atmosphere. This threshold was adopted by the World Meteorological Organisation as it meets the aeronautical requirements [21]. In principle, the value of 0.05 ensures a reliable resolution of a black object against the horizon in daylight at a wavelength of 550 nm where the human eye has the highest sensitivity. The received 5% intensity of visible light corresponds to around -13 dB of the source intensity. However, the photodiodes used in FSO systems typically have a receive sensitivity of about -30 dB (~0.001 of the transmitted intensity) or less [22], which is much lower than the eye sensitivity. In contrast with the 5% visible light threshold, FSO receivers can detect down to 0.1% of the transmitted intensity. This translates into longer visibility away from the transmitter for FSO systems as compared to visible light reception by the eye. At a distance L from the source, the signal intensity $I(L) \propto (1/L^2)$.

Therefore, the optical visibility at 0.1% threshold is much higher than that recorded for meteorological visibility. If the transmitted intensity is I_0 , when the receiver sensitivity is adjusted from $0.05 \times I_0$ to $0.001 \times I_0$ the optical visibility will be higher than the meteorological visibility by a factor of $\left(10/\sqrt{2}\right)$ for the same wavelength (550 nm) under the same weather

same wavelength (550 nm) under the same weather conditions. In this view, as a future study it should be considered to translate measured meteorological visibility into optical visibility for determination of atmospheric attenuation coefficients.

Copyright © 2020 Praise Worthy Prize S.r.l. - All rights reserved

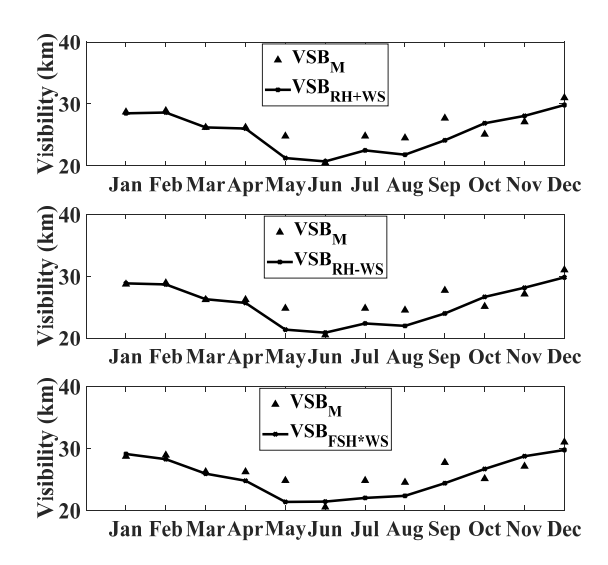


Fig. 6. MLR Fitting with Interaction Terms

TABLE XV
REGRESSION EQUATIONS FOR OTHER CITIES IN SOUTH AFRICA

REGRESSION	EQUATIONS FOR OTHER		
City	Regression Equation	Correlation Coefficient	Regression Standard Error
Bloemfontein	$VSB_{BLOEM} =$ 27.9547 +1.7476×10 ⁻⁴ ($Temp \times AP$)	0.9304	0.3531
Johannesburg	$VSB_{JHB} = 10.1288$ + $(0.1937 \times Temp)$ + $(1.3808 \times WS)$	0.8888	0.6750
Kimberley	$VSB_{KIM} = 40.7399$ -0.0378(RH + WS)	0.8303	0.2443
Durban	$VSB_{DBN} = 15.4965$ + $(5.6239 \times FSH)$	0.6580	0.7743
Kruger Mpumalanga	$VSB_{MPU} = 15.9984$ -8.6808×10 ⁻⁵ $\left(Temp^{(WS)}\right)$	0.6386	0.7823
Polokwane	$VSB_{POL} = 24.9626 - $ $0.0135 (AP \times FSH)$	0.8431	0.8234
Port Elizabeth	$VSB_{PE} = 16.8358 + (15.4479 \times FSH)$	0.6190	0.7921

IX. Conclusion

The modeling of visibility has been presented through regression analysis. It has been shown in this study that meteorological parameters at a location can be used adequately to model and possibly predict optical signal visibility. As shown in the discussions, all models presented have a good agreement with the measured data.

In the case of multiple regression models, the significance of the model parameters is achieved by reducing the effects of multicollinearity. The choice of the model may not be reliant on just its performance but rather the availability of the parameters as well. SLR models can be used in situations whereby a single meteorological parameter is measured reliably over a

long period of time in the absence of others. Otherwise, it is preferable to use MLR models to take into account all the different constructs each parameter describes.

However, caution must be exercised when too many parameters are available to avoid model overspecification. In such cases, the fitting algorithm may capture the idiosyncratic properties of that specific data rather than the true underlying trend of how visibility actually varies. In locations where measured visibility data is not available, visibility may be inferred from measurement data collected in locations with similar weather patterns. As part of future work, the performance of these visibility regression models will be compared with various artificial neural network predictive models such as the Generalized Regression Neural Network (GRNN), Multi-Layer Perceptron (MLP) neural network and Gaussian Process Regression (GPR) Delta based method.

Acknowledgements

The authors of this paper would like to thank the South African Weather Service (SAWS) for providing the data which made this work possible.

References

- C. Yu, L. Yu, Y. Wu, Y. He, and Q. Lu, Uplink scheduling and link adaptation for narrowband Internet of Things systems, *IEEE Access*, Volume 5, February 2017, Pages 1724-1734.
- [2] I. Alimi, A. Shahpari, V. Ribeiro, N. Kumar, P. Monteiro, and A. Teixeira, Optical wireless communication for future broadband access networks, 2016 21st European conference on networks and optical communications (NOC), pp. 124-128, Lisbon, Portugal, June 2016.
- [3] G. Parca, A. Tavares, A. Shahpari, A. Teixeira, V. Carrozzo, and G. T. Beleffi, FSO for broadband multi service delivery in future networks, 2013 2nd International Workshop on Optical Wireless Communications (IWOW), pp. 67-70, Newcastle upon Tyne, UK, October 2013.
- [4] Z. Ghassemlooy, W. Popoola, and S. Rajbhandari, *Optical wireless communications: system and channel modelling with Matlab*® (CRC press, 2019).
- [5] Ceruti, A., Bombardi, T., Piancastelli, L., Visual Flight Rules Pilots Into Instrumental Meteorological Conditions: a Proposal for a Mobile Application to Increase In-flight Survivability, (2016) International Review of Aerospace Engineering (IREASE), 9 (5), pp. 144-151.
 - doi: https://doi.org/10.15866/irease.v9i5.10391
- [6] A. Usman, G. Ismaila, K. Olaore, and S. Lawal, Developing a model for predicting the visibility for Sokoto using fraction of sunshine hours data, *Research Journal of Applied Sciences*, Volume 6, (Issue 6), 2011, Pages 378-380.
- [7] A. Usman, K. Olaore, and G. Ismaila, Estimating visibility using some Meteorological data at Sokoto, Nigeria, *Int. J. Basic Appli. Sci*, Volume. 1, (Issue 4), April 2013, Pages 810-815.
- [8] D. Akpootu, M. Iliyasu, W. Mustapha, S. Aruna, and S. Yusuf, Developing Regression Models for Estimating Atmospheric Visibility over Ikeja, Nigeria, *Journal of Scientific Research and Reports*, Volume 15, (Issue 6), September 2017, Pages 1-14.
- [9] Balamurugan, S., Alwarsamy, T., Boring Tool Chatter Suppression Using Magneto-Rheological Fluid Damper through Regression Models, (2013) International Review of Mechanical Engineering (IREME), 7 (3), pp. 556-562.
- [10] Deb, T., Kumar Pal, S., Study on Uplift Behavior of Single Belled Anchor Piles in Sand Bed and Multiple Regression Analyses, (2017) International Review of Civil Engineering (IRECE), 8 (3),

Copyright © 2020 Praise Worthy Prize S.r.l. - All rights reserved

- pp. 97-112.
- doi: https://doi.org/10.15866/irece.v8i3.12001
- [11] Idroes, R., Noviandy, T., Maulana, A., Suhendra, R., Sasmita, N., Muslem, M., Idroes, G., Irvanizam, I., Retention Index Prediction of Flavor and Fragrance by Multiple Linear Regression and the Genetic Algorithm, (2019) *International Review on Modelling and Simulations (IREMOS)*, 12 (6), pp. 373-380. doi:https://doi.org/10.15866/iremos.v12i6.18353
- [12] Jai Aultrin, K., Anand, M., Optimization of Machining Parameters in AWJM Process for Lead Tin Alloy Using RSM and Regression Analysis, (2015) *International Review of Mechanical Engineering (IREME)*, 9 (2), pp. 136-144. doi: https://doi.org/10.15866/ireme.v9i2.4791
- [13] Thanga Parvathi, B., MercyShalinie, S., Differential Evolution (DE) based Multiple Regression Model for Classification, (2014) International Review on Computers and Software (IRECOS), 9 (6), pp. 1117-1124.
- [14] E. Kinab, T. Salem, and G. Merhy, BIPV building integrated photovoltaic systems in mediterranean climate, *International Conference on Renewable Energies for Developing Countries* 2014, pp. 180-185, Beirut, Lebanon, November 2014.
- [15] M. Sanz, A. Carrara, C. Gimeno, A. Bucher, and R. Lopez, Effects of a dry and warm summer conditions on CO2 and energy fluxes from three Mediterranean ecosystems, *Geophys. Res. Abstr*, Volume 6, 2004, Page 3239.
- [16] T. Silva, R. Vicente, F. Rodrigues, A. Samagaio, and C. Cardoso, Performance of a window shutter with phase change material under summer Mediterranean climate conditions, *Applied Thermal Engineering*, Volume 84, June 2015, Pages 246-256.
- [17] E. Xoplaki, J. F. González-Rouco, J. Luterbacher, and H. Wanner, Mediterranean summer air temperature variability and its connection to the large-scale atmospheric circulation and SSTs, *Climate dynamics*, Volume 20, (Issue 7-8), March 2003, Pages 723-739.
- [18] G. James, D. Witten, T. Hastie, and R. Tibshirani, An introduction to statistical learning (Springer-Verlag New York, 2013).
- [19] S. Sheather, A modern approach to regression with R (Springer-Verlag New York, 2009).
- [20] M. H. Kutner, C. J. Nachtsheim, J. Neter, and W. Li, Applied linear statistical models (McGraw-Hill Irwin New York, 2005).
- [21] M. Jarraud, Guide to meteorological instruments and methods of observation, World Meteorological Organisation (WMO), Geneva, Switzerland, Volume 1, (Issue 8), 2008, Page 29.
- [22] A. Prokes, Atmospheric effects on availability of free space optics systems, *Optical Engineering*, Volume 48, (Issue 6), June 2009, Page 066001.
- [23] Al-Adwany, M., Yahya, H., Thanoon, M., Hamdoon, H., Saadallah, N., Hamed, A., Simulation and Hardware Implementation of DC-Biased Optical OFDM (DCO-OFDM) for Visible Light Communications, (2020) International Review on Modelling and Simulations (IREMOS), 13 (2), pp. 108-117. doi: https://doi.org/10.15866/iremos.v13i2.17486
- [24] Cárdenas, J., Valencia, G., Forero, J., Hydraulic Performance Prediction Methodology in Regenerative Pumps Through CFD Analysis, (2019) *International Journal on Energy Conversion* (IRECON), 7 (6), pp. 253-262. doi: https://doi.org/10.15866/irecon.v7i6.18341

Authors' information

¹Discipline of Electrical, Electronic and Computer Engineering, University of KwaZulu-Natal, Durban, South Africa.

²Department of Electrical, Computer and Telecommunication Engineering, Botswana International University of Science & Technology, Palapye, Botswana.



Olabamidele O. Kolawole received his Bachelor of Technology degree in Physics (Electronics) from the Federal University of Technology, Akure, Nigeria in 2012 and a Master of Science degree in Electronic Engineering from the University of KwaZulu-Natal, Durban, South Africa in 2018. He is currently studying to obtain his Doctorate in

Electronic Engineering at the University of KwaZulu-Natal, Durban, South Africa. He is a member of the IEEE Eta Kappa Nu (Mu Eta chapter) and a student member of the IEEE. His research interests include free space optics and RF propagation studies.



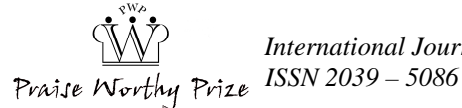
Modisa Mosalaosi received his Bachelor's degree in Electrical Engineering in 2009, MScEng and PhD degrees in Electronic Engineering in 2015 and 2017 respectively from the University of KwaZulu-Natal, Durban, South Africa. He is currently a Lecturer at the Department of Electrical, Computer and Telecommunication Engineering. Botswana

Telecommunication Engineering, Botswana International University of Science and Technology, Palapye, Botswana. He is a member of the IEEE Eta Kappa Nu (Mu Eta chapter) and a professional member of the IEEE. His research interests include power line communications, RF and propagation studies and free space optics.



Thomas J. O. Afullo obtained his Bachelor's degree in Electrical and Electronic Engineering (Hons) from the University of Nairobi in 1979, MSEE from the University of West Virginia, USA in 1983 and the license in Technology and PhD in Electrical Engineering from Vrije Universiteit (VUB), Belgium in 1989. He is currently a Professor and Director for Centre for

Radio Access and Rural Technology (CRART) in the Discipline of Electrical, Electronic and Computer Engineering at the University of KwaZulu-Natal, Durban, South Africa. He is a member of the Eta Kappa Nu (MHKN), senior member, IEEE and a Fellow of the South African Institute of Electrical Engineers (FSAIEE). His research interests include RF and propagation studies in Africa, free space optics and power line communications.



Modeling Environmental Effects on Electromagnetic Signal Propagation Using Multi-Layer Perceptron Artificial Neural Network

Virginia C. Ebhota, Viranjay M. Srivastava

Abstract – In this research work, the impact of environmental factors affecting electromagnetic signal propagation in microcell built-up area with residential and commercial buildings referred to as location-1 and rural area surrounded by mountains, tall trees and foliage referred to as location-2 have been studied and analyzed. The objective of this work is to investigate, analyze and discuss the effects of environmental factors on electromagnetic signal propagation in the two locations and their impact on electromagnetic signal during its propagation. Further objective of this work is modeling signal power losses in the two locations using Multi-Layer Perceptron Artificial Neural Network, using recorded errors from trained experimental data collected from Long Term Evolution network from each of the locations. 1st order statistical performance indices such as Root Mean Squared Error, Mean Absolute Error, Standard Deviation and Correlation Coefficient have been employed for error analysis. The results from Location-1 give minimal transmission errors, which show that radio frequency signal requires clear unobstructed transmission path. Results from location-2 demonstrate higher transmission error that can be attributed to multipath mechanism and fading phenomenon caused by the presence of mountains, tall trees and foliage. This prediction is very important for performance optimization of wireless networks during new network planning, design and upgrade especially in similar areas as location-2. Copyright © 2020 Praise Worthy Prize S.r.l. - All rights reserved.

Keywords: Electromagnetic Signal, Environment Effects, Fading Phenomenon, Signal Power Loss, Artificial Neural Network, Multi-Layer Perceptron

	Nomenclature
α	Decay rate parameter
β	Performance index
δ	Weight update vector
λ	Damping factor
a	Neuron
b	Bias
E	Error
E_d	Sum squared error
E_s	Sum squared weight
F	Cost function
J	Jacobian matrix
H	Hessian factor
r	Correlation coefficient
$w \times x$	Point product
n	Number of input
w	Vector of weights
W_{xa}	Weight of neurons
ANN	Artificial Neural Network
BS	Base Station
BP	Back Propagation
BR	Bayesian Regularization
GPS	Global Positioning System
GSM	Global System for Mobile Communication
LM	Levenberg-Marquardt
LTE	Long Term Evolution Network

ML	Machine Learning
MSE	Mean Squared Error
MAE	Mean Absolute Error
MLP	Multi-Layer Perceptron
MS	Mobile Station
PL	Pathloss
R	Receiver
RSRP	Reference Signal Receive Power
RMSE	Root Mean Squared Error
SD	Standard Deviation
T	Transmitter
TEMS	Test Mobile System Software
UE	User Equipment
MAE	Mean Absolute Error

I. Introduction

As signal transmits from the transmitter to the receiver, there is decrease in the signal strength because of different interferences, which result to pathloss. The complexity of the propagation environment contributes adversely to difficulty in the prediction of received signal strength [1]-[3]. Pathloss is the attenuation of electromagnetic signal as it transmits through space [4].

An accurate and non-complex pathloss prediction model is important for coverage prediction, system

performance optimization, Base Station (BS) locations etc. Accordingly, there have been efforts from different engineers and researchers across the globe in order to find out realistic models for the prediction of pathloss at different frequencies and in different scenarios. Long Term Evolution Network (LTE) and 5th generation networks are designed to support wide coverage, improve connection density, increase throughput, enhance spectral density and reduce radio tendency etc. Different measurement campaigns and drive tests have been carried out to collect attenuation data at new frequencies.

The planning of network communication system such as LTE comes with stern challenges and superior models such as model based on Artificial Neural Networks (ANNs) are required for pathloss prediction [5].

Traditional pathloss models are based on deterministic and empirical methods [4]. The former applies radio signal propagation mechanism and analysis based on numerical techniques for modeling, while the latter relies majorly on measurements from specific scenario and at given frequency. Deterministic models can achieve high accuracy and give the pathloss value at any precise position, however, they are computational inefficient as a result of excessive computational time in real environment [6]. On the other hand, empirical models consider few parameters such as frequency of operation, antenna height, antenna separation distance etc., and as such, the model equations are concise. However, because the parameters are extracted from data measured from specific scenario, their accuracy are most of the time unsatisfactory when applied to broader environment.

Machine Learning (ML) is a technique that is based on vast dataset and flexible model architecture for prediction. Nowadays, ML techniques have been applied in different areas such as data mining, computer vision, self-driving cars, speed recognition etc. The different tasks performed using ML can be classified either as supervised or unsupervised learning. The task of supervised learning algorithms with labelled data is to learn general and accurate function between input and output data. This makes it appropriate for solving regression and classification problems. On the other hand, unsupervised learning algorithms need to describe the hidden structure from unlabeled data. In principle, prediction of pathloss is a supervised learning regression problem that can appropriately be solved by ML technique such as ANNs. Machine learning techniques are more accurate than the traditional empirical models and more computational efficient than the deterministic ones [3], [7]. Amongst the ML based techniques, ANN are widely used in the prediction of pathloss, especially back propagation-based models. This is because Back Propagation (BP) ascertains the gradient of loss function and it is broadly applied in the optimization of gradient descent algorithm for the adjustment of weight of every neuron which contributes to the learning process [8].

Back propagation-based ANN comprises an input layer, an output layer and one or more hidden layers.

Artificial neural network with multiple layers of

neurons in the hidden layer enables enhanced processing power and flexibility of the network system. However, many neurons in the hidden layer usually give rise to over specification of the system, thereby causing poor generalization, while few neurons in the hidden layer cause improper fitting of input data resulting to a reduction in the system robustness [9]. Similar research work has been carried out in [10]. The authors have concentrated on environmental factors (rain attenuation) that affect propagation at very high frequencies (20 GHz-30 GHz) electromagnetic signal in space communication.

The characteristics of radio propagation at 20 GHz band as a result of rain attenuation have been studied in [11]. In [12], the authors have used prediction models that combine rain combination and other impairments for earth-satellite paths. The authors in [13] have studied the centimeter and the millimeter wave attenuation and brightness temperature as a result of atmospheric oxygen and water vapor. Their various results have demonstrated a negative impact of each of the considered environmental factor on wave propagation. In this research work, authors have studied and analyzed the impact of environmental factors affecting signal power during electromagnetic signal propagation at 1900 MHz frequency band. The analyses are carried out using experimental data from LTE cellular network collected from two different locations and Multi-Layer Perceptron (MLP) ANN employed in modeling the impact of the environmental factors (multipath mechanism and fading phenomenon). Furthermore, the effectiveness of MLP-ANN in modeling signal power loss in the two considered locations have been investigated and compared. The impact of environmental factors in each location using recorded errors during signal transmission was analyzed.

This research paper has been organized as follows.

Section II has the basic terminologies for the scenario and networks used in the research work. Section III discusses the method of collection of the experimental data. Section IV has the results and analysis of the errors for this model. Finally, Section V concludes the work and recommends the future aspects.

II. Basic Terminologies for the Scenario and Networks Used in this Research Work

II.1. Environmental Factors Affecting Signal Propagation

The design and the development of communication network systems at different frequencies are mostly affected by medium of propagation [10]. These include atmospheric influences, attenuation from rain, clouds, atmospheric gases, fog and scintillation which becomes critical as frequency increases. Therefore, information availability on the effects of propagation is an important criterion for effective design of communication network [14]. The success in the execution of the space program

is dependent on adequate evaluation of the adverse nature of the natural atmosphere. Despite radiations, the atmosphere comprises different types of plasma environments meteoroids, atomic oxygen, ultraviolent radiations, debris and thermal environment. Some basic environmental factors that affect signal propagation considered during analysis in this research work are as follow.

II.1.1. Fading Phenomenon

Fading in radio system is majorly related to atmospheric changes and imposes more problems at increased frequencies. Though by nature it is a random event, there are certain conditions that exaggerate this phenomenon and make it more troublesome. The effect of fading is more pronounced during a clear and quiet period than during an extreme weather, while fluctuations in the electromagnetic field strength are greater during the night than during the daytime [15].

The fading element should be added in the network plan to cater for carrier-to-interference (C/I) ratio.

However, the fading margin to be included to account for this depends on certain elements such as the correlation of pathloss prediction error, which thereafter has effect on the terrain and clutter environment. It also depends on the handover application and settings from location to location at the movement of customers, which are unnoticed. In addition, it depends on the management techniques employed in the network to cater for the variability and density of calls, the users and services distribution in the area. The needed fade margin increases as the prediction error of the model increases.

For un-correlated errors between two locations with prediction standard deviation of 7.8 dB for both locations, the operational variability of C/I and subsequently the fading margin is in the region of 11.0 dB overlap for a network with 50% confidence [16].

There is an increase in this figure to 17.6 dB for a network with 95% confidence. Therefore, the C/I level is 17.6 dB for fade margin of 95%. Tolerating this margin for link budget results to very low capacity and ineffective network design.

II.1.2. Slow Fading

Measured signal level, terrain and location information with the antenna radiation pattern are all processed to give pathloss measurement against location.

These processes comprise distance dependent component that depends on characteristics of the local clutter of the nearby propagation environment. When the distance dependent component is subtracted from the overall loss, the subsequent effect is slow shadowing [1].

The statistics of the shadowing are examined to generate representative parameters of the test area using 1st order statistical performance indicators such as standard deviation, etc. The shadowing parameter can be anticipated per clutter class or for an area depending on

the available measurement density for every clutter category with the test area. The shadowing parameters derived are used to create set of shadowing predictions for the total area of interest.

II.2. Artificial Neural Networks

Artificial neural networks are employed in solving non-linear regression problems such as pathloss prediction and have demonstrated low prediction errors when there are enough data sets [4], [15], [17]. The ANN such as MLP network based on neuron model is a feedforward network structure that comprises an input layer, one or more hidden layers and an output layer in a feedforward structure. Neurons are connected to the ones in the next layer in its entirety by different weights while there is no neuron connection in the same layer. The MLP-ANN model complexity and accuracy depend on the number of both the hidden layers and the neurons, which determine the size of the network. However, finding an adequate MLP-ANN structure for the prediction of pathloss remains an open problem, since the architectural definition of MLP-ANN affects the layers and neurons for connection. Inappropriate choices can resist solving problems of inadequate parameter adjustments or over-fitting of the training data.

Therefore, the architectural optimization of the hidden layers and neurons connections in order to establish MLP-ANN that solves a given prediction problem effectively remains open for research

II.2.1. Multi-Layer Perceptron ANN

Multi-layer perceptron artificial neural network comprises several neurons of multiple layers with a non-linear activation function such as hyperbolic tangent, logistic sigmoid and rectifier unit [17], [22]-[25]. A perceptron is a simply neural network model with a single computational neuron comprising of several inputs, a processor and an output. It calculates the error between sample data output and network output and uses it in adjusting the weight during network training. The activation function for a perceptron neuron is a binary function with two possible results [17]:

$$f(x) = 1ifw \times x + b > 0 \tag{1}$$

where w is a vector of weights (real value), b is bias, and $w \times x$ is point product of $\sum_{i=1}^{n} x_i w_i$, n is number of inputs.

However, perceptron neuron cannot solve problems that are linearly separable and cannot reach a state with every input vector properly trained with non-linearly separable training sets because of its linearity. This results to the non-convergence of the perceptron network. Therefore, by connecting neurons in multi-layers with non-linear activation function, there is the creation of non-linear decision boundaries that permits solving of

more complicated and non-linearly separable problem [8]. In training MLP-ANN with x_n input neurons as shown in Fig. 1, the overall network output Y is the network output from the first hidden layer, which becomes the input to the second hidden layer until it is trained in the 3rd hidden layer which eventually delivers it to the output. The output from the first hidden layer to the second hidden layer can be stated as:

$$x_{1}^{n} = f\left(\sum_{k=1}^{n} w_{ka} x_{1}^{n}\right) \tag{2}$$

where n=1,2,3, w_{xa} is the weight and x and a are neurons. This apparently becomes input to the second hidden layer b_1^n and the sequence continues for the number of the hidden layer adopted for the network training. The overall network output becomes:

$$Y_{1}^{n} = f\left(\sum_{c=1}^{n} w_{cy}^{n} c_{1}^{n}\right)$$
 (3)

II.2.2. Training Using Bayesian Regularization Algorithm

Bayesian Regularization (BR) algorithm is applied in weight update during network training in contract with Levenberg-Marquardt (LM) algorithm and it has demonstrated near better training by linear permutation of squared error and weight variables [9]. This algorithm uses Jacobian for network computation which presumes a performance Mean Squared Error (MSE) and computations use BP, modifying all the variables in accordance with LM function approximation method [18]:

$$\[J^t J + \lambda I\] \delta = J^t E \tag{4}$$

where J is Jacobian matrix, δ is weight update vector (unknown), E is error, J'J is approximated Hessian and λ is the damping factor. For the optimization process, the damping factor is modified at every iteration. Generally, the Hessian is approximated using Jacobian matrix and not necessarily computation of least square problems [19]:

$$H = J^t J \tag{5}$$

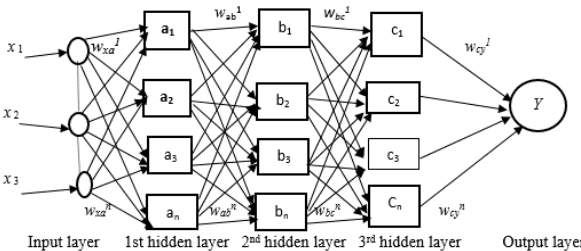


Fig. 1. Architecture of MLP-ANN with three hidden layers adopted during network training in this research work

Levenberg-Marquardt algorithm is sensitive and based on the preliminary weight value of the network.

Convergence may take place at local minima or non-convergence observed. The data outliers and initial weights are also not considered, and this may result in poor generalization [18]. Therefore, BR algorithm is applied to avert poor network generalization by permitting adequate weights that are essential for solving specific problem [20]. It expands the cost function to observe the smallest error using the smallest weight.

Therefore, two hyper-parameters, alpha and beta, are introduced in order to advise the direction of the learning process (minimal error or minimal weight). The cost or performance function is expressed as [20]:

$$F = \beta E_d + \alpha E_s \tag{6}$$

where E_d is the sum squared error while E_s is sum squared weight, α and β are the decay rate parameter and performance index, respectively. Addition of BR to LM adds up a small overhead to the process of network training.

III. Data Collection and Methodology

The data employed for ANN network training have been collected from two different locations in order to investigate the impacts of environmental factors affecting electromagnetic signal in course of transmission. The first location (location-1) is a metropolitan area with residential and commercial buildings while the second one (location-2) is a rural area surrounded by mountains, tall trees and foliage.

III.1. Tools for Data Collection, Data Collection and Methodology

Data collection from both location 1 and 2 has been piloted by means of drive test from selected BSs transmitting at 1900 MHz frequency band with the provision of information on the cell file by a telecommunication company using LTE cellular network.

A digital map of the areas has been adopted during the drive test and the equipment for the drive test comprises a laptop and a Sony Ericsson mobile handset. This equipment is installed with 2016 Test Mobile System Software (TEMS); this allows it to access and extract signal data alongside the measurement test route. Power inverters, Global Positioning System (GPS) have been employed for matching up of the User Equipment (UE) i.e. Mobile Station (MS) measurement locations in correlation to the field test environment and the transmitter, test cables etc. are all utilized. The drive test tools and the technique of measurement permit access generation and acquiring real time LTE signal power data from the BS that has been employed for the ANN training. The Transmitter (T) and the Receiver (R) parameters adopted for experimental purpose are transmitter frequency of 1900 MHz, transmitter antenna

Copyright © 2020 Praise Worthy Prize S.r.l. - All rights reserved

height of 34 m, transmitter power of 43 dB, receiver antenna gains of 18 dBi and receiver antenna height of 1.5 m. The LTE signal parameter extracted during the drive test log files for the prediction analysis in ANN is the Reference Signal Receive Power (RSRP (dBm)). This gives the signal power measurement that has been carried out in the two locations for case study.

III.2. Multi-Layer Perceptron Network Training and Prediction

The MLP-ANN training has been carried out using a written neural network program, which has been computed and simulated in MATLAB 2015a using BR training algorithm (trainbr), all coded and implement by means of ANN toolbox. 3,895 data have been collected from location 1 while 1,932 have been collected from location 2. These data have measured electromagnetic signal power as it transmits over given range of distances. The data serve as inputs to the MLP-ANN, which has been normalized in Excel spreadsheet in order to prevent bias of data presentation. Network training has been carried out using early stopping technique with data ratio of 70% for training, 20 % for testing and 10 % for validation. The 1st order statistical performance metrics: Mean Absolute Error (MAE), Root Mean Squared Error (RMSE), Standard Deviation (SD) and correlation coefficient (r) have been used for error analysis of the trained network. These parameters calculate error between the actual measured values and the predicted values during network training.

IV. Error Analysis: Results and Discussion

The respective experimental data obtained from location-1 and location-2 have been employed in MLP-ANN training and prediction and results are shown in Table I and Table II respectively. The basis of comparison in this work is the error encountered during signal transmission from the transmitting BS for the two locations. The MLP-ANN has been trained with different number of neurons in the hidden layer ranging from 10-60 neurons to ensure well-adapted trained neural network that best predicts the signal power losses during network training. The regression function and the training performance have eben analyzed using RMSE, MAE, SD and r.

IV.1. Regression Analysis

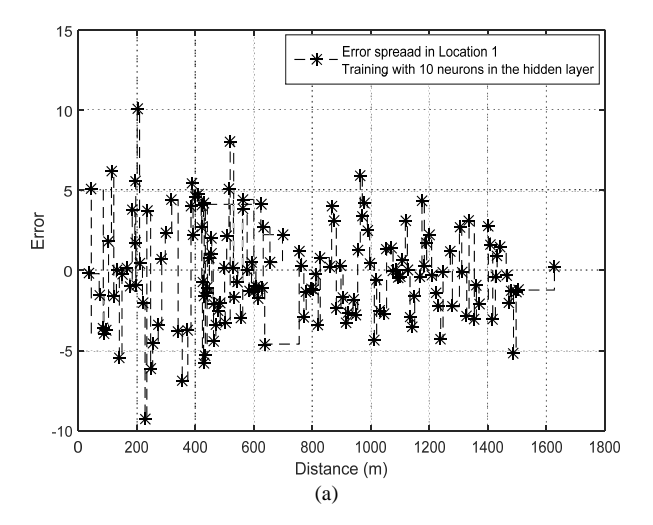
The regression function compares the actual output with the desired one i.e. the target during MLP-ANN training. It returns correlation coefficient between measured and predicted data with values closer to +1 implying closer connection [3]. The error spread at various distances during signal propagation from Fig. 2(a) is seen to be within the range of -10 to +10 and from -7 to +7 in Fig. 2(b). This shows a closer relationship between measured and predicted data using 30 neurons in

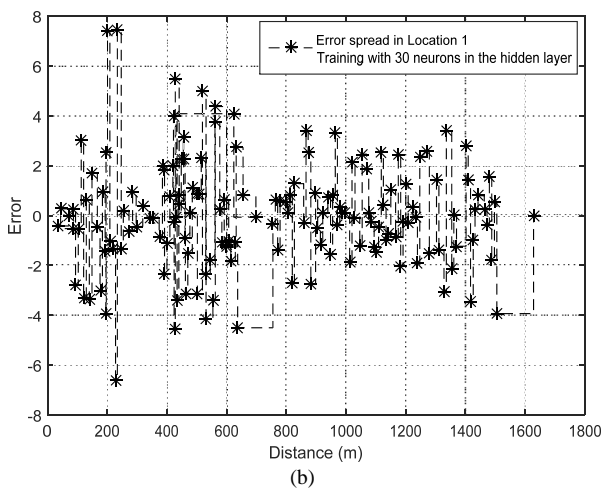
the hidden layer during MLP-ANN training in comparison to training with 10 neurons in the hidden layer. From Table I, the regression coefficient of correlation is seen to be 0.9120, 0.9447. 0.9533, 0.9464, 0.9483, and 0.9436 for MLP-ANN training of 10 to 60 numbers of neurons in the hidden layer. Averagely, the regression is close to +1 and it shows a strong connection between measured and predicted values on application of 30 neurons in the hidden layer, since minimal error encounter has been recorded. Figs. 2(a) and 2(b) show real-time error spread at different distance as the signal transmits from BS transmitter to the receiver terminal for 10 and 30 neurons in the MLP-ANN hidden layer respectively.

TABLE I

1st Order Statistical Performance Indices From MLP-ANN
TRAINING FOR LOCATION-1 (TRAINING ALGORITHM - trainbr)

Hidden layer	Epoch	Training	RMSE	MAE	SD	r
neurons	no 1000	time (s)	KWISE	MAL	SD	1
10	359	7	3.0798	2.4167	1.9091	0.9120
20	542	159	2.4872	1.8306	1.6837	0.9447
30	1000	180	2.2669	1.6528	1.5516	0.9533
40	1000	747	2.4305	1.4819	1.9265	0.9464
50	1000	780	2.4868	1.4486	1.7214	0.9483
60	1000	1,200	2.0218	1.2581	1.5827	0.9436



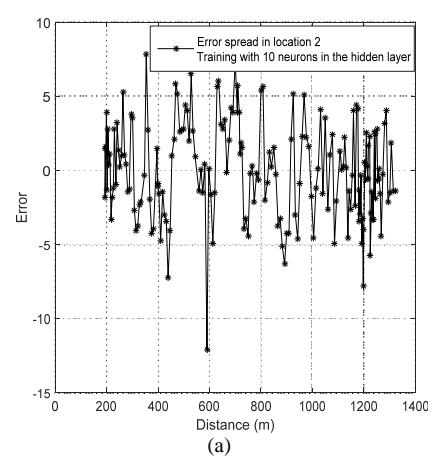


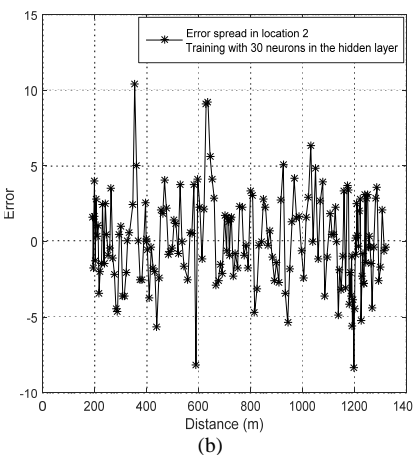
Figs. 2. Regression error spread in Location-1 at ANN training with (a) 10 neurons and (b) 30 neurons in the MLP-ANN hidden layer

Copyright © 2020 Praise Worthy Prize S.r.l. - All rights reserved

From Figs. 3, the error spread during signal propagation at different distances ranges from -13 to +8 with 10 neurons in the hidden layer of MLP-ANN and -9 to +11 with 30 neurons in the hidden layer of MLP-ANN during network training. This shows greater error in comparison to Figs. 2(a) and 2(b) of location-1 as the regression or coefficient of correlation is far from +1.

This phenomenon can be attributed to the environmental factors such as multipath mechanism, which result in refraction, reflection and scattering of propagation signal because of mountains, tall trees, and foliage that cover location-2 and obstruct signal propagation. The recorded coefficient of correlation shows values of 0.7709, 0.8300, 0.8781, 0.8834, 0.8941 and 0.8991 for different MLP-ANN training with 10 to 60 numbers of neurons in the hidden layer as shown in Table II.





Figs. 3. Regression error spread in Location-2 at ANN training with (a) 10 neurons, and (b) 30 neurons in the MLP-ANN hidden layer

TABLE II 1st Order Statistical Performance Indices From MLP-ANN TRAINING FOR LOCATION-2 (TRAINING ALGORITHM-trainbr)

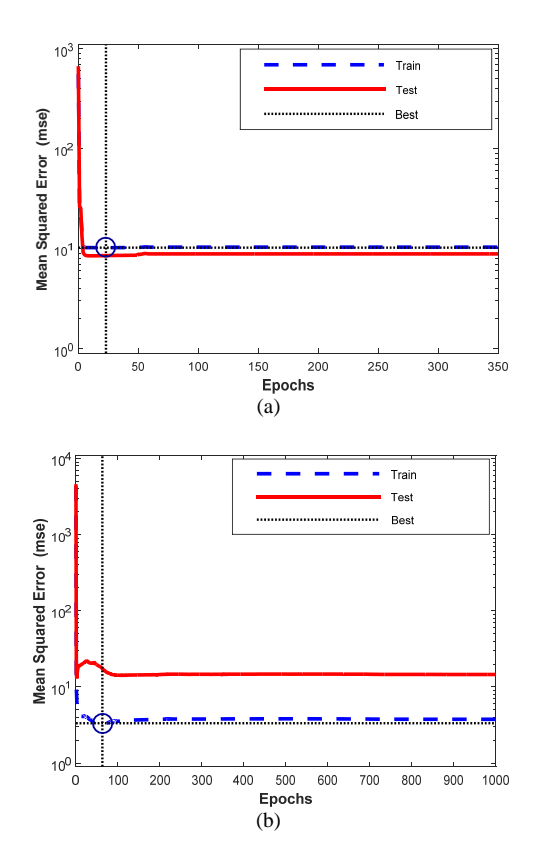
Hidden layer neurons	Epoch no 1000	Training time (s)	RMSE	MAE	SD	r
10	240	11	4.2361	3.6466	1.9988	0.7709
20	500	167	3.9398	2.4966	1.9540	0.8300
30	991	184	3.5690	2.2636	1.8594	0.8781
40	995	728	3.1438	1.8211	1.8103	0.8834
50	995	800	3.0030	1.7805	1.7764	0.8941
60	1000	1100	2.9413	1.7505	1.6611	0.8991

These values are farther from +1 compared to the values recorded in location-1, thus showing stronger disconnection between measured and predicted values.

IV.2. Training Performance

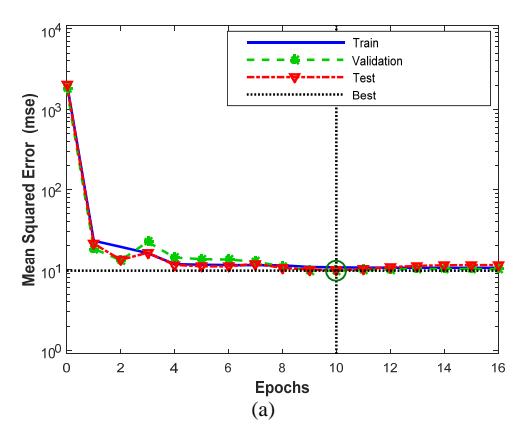
The MSE calculates the average of the squares of the error during network training and prediction i.e. the average squared difference between the measured values and the predicted value with values closer to zero being better [21]. The MSE for both figures 4(a) and 4(b) is approximately 10. Multipath signal propagation mechanisms and other factors that cause interferences on transmitted signal power, which results, to poor reception at the user terminal are seen to be very minimal in Figs. 4(a) and 4(b) of location-1 in comparison to Figs. 5(a) and 5(b) of location-2. The MSE as shown in Figs. 5(a) and 5(b) has rapidly increased to approximately 10³ with MLP-ANN training with 10 neurons and 30 neurons in the hidden layer. These show significant difference between measured and predicted values and result to higher error during electromagnetic signal propagation.

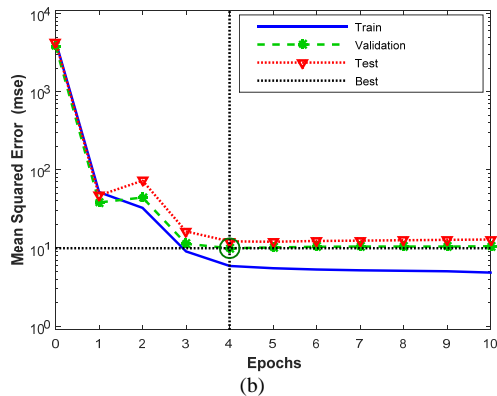
Table I and Table II clearly show strong disconnection in error computations of the 1st order statistical performance indices, the RMSE, MAE, SD, r in comparison of the two locations, with higher computed errors from location-2 demonstrating the effect of environmental factors such as mountains, tall trees and foliage on electromagnetic signal power propagation resulting to huge pathlosses.



Figs. 4. MSE in Location-1 at ANN training with (a) 10 neurons, and (b) 30 neurons in the MLP-ANN hidden layer

Copyright © 2020 Praise Worthy Prize S.r.l. - All rights reserved





Figs. 5. MSE in Location-2 at ANN training with (a) 10 neurons, and (b) 30 neurons in the MLP-ANN hidden layer

V. Conclusion and Future Recommendations

This research work has utilized MLP-ANN for modeling signal power loss with experimental data collected from two different locations in LTE cellular network; (i) a metropolitan area with residential and commercial buildings and (ii) a rural area with mountains, tall trees and foliage. Error analysis from the trained data using MLP-ANN has been carried out using 1st order statistical performance indices: RMSE, MAE, SD and r. Location-1 gives minimal training error in comparison to location-2 where mountains, trees and foliage obstructed signal transmission resulting in signal power losses thereby causing higher transmission error.

This shows the need for proper design and optimization during network planning and upgrade in scenarios such as location-2 to cater for the stochastic nature of propagation environments. For future work, broader environments for obtaining experimental data will be considered and new modeling methods using other ML techniques such as Fuzzy Inference System will be employed.

References

 V. C. Ebhota, J. Isabona, and V. M. Srivastava, Base Line Knowledge on Propagation Modelling and Prediction Techniques in Wireless Communication Networks. *Journal of Engineering*

- and Applied Sciences, vol. 13, pp. 1919-1934, 2018.
- [2] J. Isabona and V. M. Srivastava, Coverage and link quality trends in sub-urban mobile broadband HSPA network environments, Wireless Personal Communication, vol. 92, pp. 3955-3968, 2017.
- [3] V. C. Ebhota, J. Isabona, and V. M. Srivastava, Improved Adaptive Signal Power Loss Prediction Using Combined Vector Smoothing and Neural Network Approach, *Progress in Electromagnetic Research C*, vol. 82, pp. 155-169, 2018.
- [4] Y. Zhang, J. Wen, G. Yang, Z. He, and J. Wang, Path Loss Prediction Based on Machine Learning: Principle, Method, and Data Expansion, *Applied Sciences*, pp. 1-18, 2019.
- [5] Ebhota, V.C., Isabona, J. & Srivastava, V.M. Environment-Adaptation Based Hybrid Neural Network Predictor for Signal Propagation Loss Prediction in Cluttered and Open Urban Microcells. Wireless Pers Commun 104, 935–948 (2019). doi: https://doi.org/10.1007/s11277-018-6061-2
- [6] Isabona, J., Srivastava, V., Radio Channel Propagation Characterization and Link Reliability Estimation in Shadowed Suburban Macrocells, (2017) International Journal on Communications Antenna and Propagation (IRECAP), 7 (1), pp. 57-63.
- doi:https://doi.org/10.15866/irecap.v7i1.10343
- [7] W. Jiakai, "Forget the Learning Rate, Decay Loss," *International Journal of Machine Learning and Cybernetics* 2019.
- [8] P. Sridhar, Novel Artificial Neural Network Path loss Propagation Models for Wireless Communications, Advances in Wireless and Mobile Communications, vol. 10, pp. 233-237, 2017.
- [9] V. C. Ebhota, J. Isabona, and V. M. Srivastava, Signal Power loss Prediction based on Artificial Neural Networks in Microcell Environment, presented at the 3rd IEEE International Conference on Electro-Technology for National Development, Owerri, Nigeria, 2017.
- [10] A. Khola and S. Niranjan, A Study on Environmental Factors that Adversely Affect the Propagation of Very High Frequency Electromagnetic Waves in Space Communication Systems, *International Journal of Electronics Engineering*, vol. 3, pp. 309-311, 2011.
- [11] M. Shimba, Radio Propagation Characteristics Due to Rain at 20Ghz Band, *IEEE Trans*, vol. 22, pp. 507-509, 1974.
- [12] A. Dissanayake, Prediction Model that Combines Rain Combination and Other Propagation Impairments Along Earthsatellite Paths, *IEEE Trans* vol. 45, p. 1546, 1997.
- [13] E. K. Smith, Centimeter and Millimeter Wave Attenuation and Brightness Temperature Due to Atmospheric Oxygen and Water Vapour, *Radio Science*, vol. 17, pp. 1455-1464, 1982.
- [14] A. Dissanayake, Prediction Model that Combines Rain Combination and Other Propagation Impairments Along Earthsatellite Paths, *IEEE Trans. Antennas Propag*, vol. 45, p. 1546, 1997
- [15] M. Ayadi, A. B. Zineb, and S. A. Tabbane, UHF Path loss Model using Learning Machine for Heterogeneous Networks, *IEEE Trans. Antennas Propagation*, vol. 65, pp. 3675-3683, 2017.
- [16] B. J. Cavalcanti and G. A. Cavalcante, A Hybrid Path Loss Prediction Model based on Artificial Neural Networks using Empirical Models for LTE And LTE-A at 800 MHz and 2600 MHz, Journal of Microwaves, Optoelectronics and Electromagnetic Applications, vol. 16, pp. 704-718, 2017.
- [17] A. B. Zineb and M. Ayadi, A multi-Wall and Multi-Frequency Indoor Path Loss Prediction Model using Artificial Neural Networks., *Arabian Journal of Science and Engineering*, vol. 41, pp. 987-996, 2016.
- [18] Rusilawati, R., Soeprijanto, A., Wibowo, R., Reactualization of a Modified Single Machine to Infinite Bus Model to Multimachine System Steady State Stability Analysis Studies Using Losses Network Concepts and Radial Basis Function Neural Network (RBFNN), (2017) International Review on Modelling and Simulations (IREMOS), 10 (2), pp. 112-120. doi: https://doi.org/10.15866/iremos.v10i2.11207
- [19] R. D. De Veaux and L. G. Ungar. (2017, 20/04). A brief Introduction to Neural Networks. Available: http://www.cis.upenn.edu/~ungar/Datamining/Publications/nnetintro.pdf
- [20] Triqui, B., Benyettou, A., Comparative Study Between Radial Basis Function and Temporal Neuron Network Basic in Cardiac

Copyright © 2020 Praise Worthy Prize S.r.l. - All rights reserved

- Arrhythmia, (2018) International Journal on Communications Antenna and Propagation (IRECAP), 8 (2), pp. 186-193. doi: https://doi.org/10.15866/irecap.v8i2.14079
- [21] D. Wackerly, W. Mendenhall, and R. L. Scheaffer, *Mathematical Statistics with Applications* Belmont, CA, USA: Thomson Higher Education, 2008.
- [22] Ebhota, V., Isabona, J., Srivastava, V., Effect of Learning Rate on GRNN and MLP for the Prediction of Signal Power Loss in Microcell Sub-Urban Environment, (2019) *International Journal* on Communications Antenna and Propagation (IRECAP), 9 (1), pp. 36-45.

doi: https://doi.org/10.15866/irecap.v9i1.15329ggg

- [23] Shatnawi, M., Bani Yassein, M., Aljawarneh, S., Alodibat, S., Meqdadi, O., Hmeidi, I., Al Zoubi, O., An Improvement of Neural Network Algorithm for Anomaly Intrusion Detection System, (2020) International Journal on Communications Antenna and Propagation (IRECAP), 10 (2), pp. 84-93. doi: https://doi.org/10.15866/irecap.v10i2.18735
- [24] Monadjemi, S., Moallem, P., Automatic Diagnosis of Particular Diseases Using a Fuzzy-Neural Approach, (2018) *International Journal on Engineering Applications (IREA)*, 6 (1), pp. 29-34. doi: https://doi.org/10.15866/irea.v6i1.15143
- [25] Si Tayeb, M., Fizazi, H., A Dual-Level Hybrid Approach for Classification of Satellite Images, (2017) *International Review of Aerospace Engineering (IREASE)*, 10 (1), pp. 42-49. doi: https://doi.org/10.15866/irease.v10i1.11191

Authors' information

Department of Electronic Engineering, Howard College, University of KwaZulu-Natal, Durban - 4041, South Africa.



Dr. Virginia C. Ebhota received Bachelor of Engineering degree in Electronic Engineering from University of Nigeria, Nsukka (UNN), Master of Engineering from Enugu State University of Science and Technology, Enugu, Nigeria and a Doctoral degree in Electronic Engineering from Kwazulu-Natal, Durban, South Africa. Presently, she is working towards

post-doctoral research fellow with the department of Electronic Engineering, University of Kwazulu-Natal, Durban South Africa. She has published various peer-reviewed articles in Journals and IEEE Conferences. Her major research area is system modeling using Artificial Intelligence (AI), Artificial Neural network, etc.



Prof. Viranjay M. Srivastava is Doctorate (2012) in the field of RF Microelectronics and VLSI Design, Master (2008) in VLSI design, and Bachelor (2002) in Electronics and Instrumentation Engineering. He has worked for the fabrication of devices and development of circuit design. Presently, he is working in the Department of Electronic Engineering, Howard

College, University of KwaZulu-Natal, Durban, South Africa. He has more than 17 years of teaching and research experience in the area of VLSI design, RFIC design, and Analog IC design. He has supervised various Bachelors, Masters and Doctorate theses. He is a Professional Engineer of ECSA, South Africa and Senior member of IEEE, SAIEE, and member of IET, IEEE-HKN, IITPSA. He has worked as a reviewer for several Journals and Conferences both national and international. He is author/co-author of more than 200 scientific contributions including articles in international refereed Journals and Conferences and also author of various books.



Reduction of Mutual Coupling in Compact Antenna Array Using Meander Line Slot EBG Structure

Mahesh Kadu¹, Neela Rayavarapu²

Abstract – This paper presents the design and the fabrication of a compact Multiple-Input Multiple-Output (MIMO) antenna array with very low mutual coupling, operating in the 2.4 GHz band. The compact design is achieved by the introduction of a meander line structure in the conventional patch antenna. The reduced mutual coupling of about 52 dB is realized by inserting a periodic array of Electromagnetic Band Gap (EBG) elements in the radiating antenna elements. A prototype of the proposed antenna array has been manufactured on an FR4 substrate with a dielectric constant of 4.4 and a height of 1.6 mm. The excellent agreement between simulated and measured data confirms the performance of the proposed antenna array in a MIMO environment. This MIMO antenna array has a compact size of $0.40\lambda_0 \times 0.2\lambda_0$. For the validation of the results, the overall dimensions and the isolation level of the proposed design have been compared with designs previously reported in the literature and it has been found out that the proposed design is superior in both isolation level and compactness than its counterparts. **Copyright** © **2020 Praise Worthy Prize S.r.l. - All rights reserved**.

Keywords: Compact, Electromagnetic Band Gap, Mutual coupling, Multiple Input Multiple Output

Nomenclature

DG	Diversity Gain
DGS	Defected ground structure
EBG	Electromagnetic Band Gap
MEG	Mean Effective Gain
MIMO	Multiple Input Multiple Output
TARC	Total Active Reflection Coefficient
R	Resistance $[\Omega]$
L	Inductance [H]
C	Capacitance [F]
S11	Return loss at port 1 [dB]
S22	Return loss at port 2 [dB]
S21	Mutual coupling at port 2 [dB]
S12	Mutual coupling at port 1 [dB]
λ_0	Free space wavelength [m]

I. Introduction

Today's Multiple Input Multiple Output (MIMO) wireless communicating devices transmit or receive data simultaneously at the same frequency band. However, due to the small size of the wireless devices antenna, elements in a MIMO array have to be closely spaced.

This increases the mutual coupling between antenna elements leading to a severe reduction in the overall efficiency of the individual antenna elements. Isolation between elements can be enhanced by decreasing mutual coupling between elements in the antenna array by employing various diversity techniques [1]. One of these techniques is the polarization diversity, where two

elements radiate at orthogonal polarizations with respect to each other [2], [3]. The polarization reorients the antenna elements in an array and requires an excellent polarization match between transmit and receive antenna system. In spatial diversity, the separation distance between elements is maintained more than half of the free space wavelength to achieve desired isolation [1]-[3]. However, this isolation provided by the diversity system comes at the expense of the increased size of the antenna array. Many researchers have combined two or more diversity techniques in order to achieve good isolation. The polarization and the pattern diversity can be employed to reduce the mutual coupling between the antenna elements as reported in [4]. The combination of the diversity techniques makes the system more complex.

Hence, in order to achieve a compact array design researchers have developed various isolation enhancements techniques. Defected Ground Structure (DGS) is one of the most popular techniques, which improve isolation level by intentionally modifying the ground plane of microstrip antenna. The current flow in the ground plane responsible for coupling between adjacent antenna elements sharing a common ground plane can be controlled by various shapes and dimensions of the defect created in the ground structure.

In [5], a T-shape DGS structure designed in an antenna ground element generates a current opposite to the ground current. This results in the cancellation of ground current flowing between adjoining antenna ports leading to a reduced coupling between the ports. In another application reported in [6] an H-shape, DGS is

used to reduce the mutual coupling in an antenna array.

However, the modification of the ground plane may disturb the antenna's radiation pattern resulting in a reduced gain. Enhanced isolation is also achieved by suppressing the space waves using meta-materials.

Metamaterials are artificial materials characterized by the property of having both negative permittivity and permeability. A metamaterial isolator proposed in [7] is constructed with a polarization rotator wall placed between two dielectric resonator antennas that make the antenna to see each other as orthogonal elements in terms of mutual coupling. A similar method of introduction of metamaterial in an antenna reduces mutual coupling by up to 24 dB as reported in [8]. Nevertheless, the availability and the cost of metamaterial are serious concerns for a researcher in using this technique for isolation enhancement. Another approach to reduce the mutual coupling of stub loading has been studied by many researchers. Shunt open stubs suppress unwanted frequency bands by altering the impedance path to make the desired frequency pass through and block the other.

In [9], an F shaped stub designed to reduce the mutual coupling between two ultra-wideband MIMO antennas acts as a reflector for the radiation waves emitted by both the antenna elements towards each other. In the design of isolation technique as reported in [10], the flag-shaped stub in an antenna array creates an additional coupling path between the antenna elements, which cancels the effect due to the mutual coupling path between the antenna elements. Isolation can be improved by introducing open stubs in an antenna system but at the expense of increased size and so, the technique is suitable for large size wireless. The design of a neutralizing line between two radiating elements in an array design is another reported mutual coupling reduction technique. The neutralization technique of isolation enhancement not only helps to enhance the isolation between elements but also improves the impedance matching at the ports. In [11], the neutralization line connecting two patches creates a current flow, which is the opposite of the flow of the current on the ground plane.

This results in the cancelation of the ground current fields and hence the mutual coupling is suppressed between the two radiating patches. The drawback of the isolation technique is the increased size and the complication of radiation characteristics in an antenna system in a wireless device. Another way to reduce the mutual coupling in an antenna array is placing shorting pins or posts. The shorting pins or posts placed between two radiating elements in a microstrip patch antenna array can mitigate the current flow between two radiating elements. In order to achieve this operation the shorting pins or posts are usually located on the coupled edges of patch elements. A non-radiating folded shorting strip proposed in [12] is connected between each radiating element and ground plane. This leads to a reduction of the surface current flow between two antenna elements and the ground plane. Thus, the folded shorting strip

makes a current loop and that stops the current flow from port 1 to port 2.

Since the current path is closed between the two ports, the mutual coupling decreases drastically. The design and the placement of shorting pins /posts in an antenna array is a challenge and usually it hampers the impedance matching in the original patch design. Recently many of the researchers have utilized EBG structure for the reduction of mutual coupling. EBG suppresses surface waves leading to improved isolation between antenna elements in an antenna array for a given band gap. The various shapes of the EBG structures have been studied by researchers, for example, UC-EBG, star shape EBG, and spiral shape EBG [13]. Amongst these, mushroom EBG to reduce mutual coupling has been the most popular one due to its simplicity in design. An EBG layer consisting of the periodic arrangement of single unit fractal EBG is studied in [14] leading to the reduction of mutual coupling between the radiating patches. The isolation enhancement techniques available in the literature are compared in Table I. The comparison is based on the size requirement for an isolation technique that dictates the size of antenna array and isolation level offered. The first parameter considered for comparison is the isolation level offered by the isolation technique. The second parameter considered for comparison between different isolation techniques employed in microstrip antenna array is the total size of the antenna system itself.

The size of the antenna array is restricted by the size available for an antenna system in a compact wireless device.

Hence this parameter should be addressed by the designer while selecting a given isolation technique for a compact wireless application. From Table I, it can be seen that EBG structures offer a greater increase in isolation compared to all the other techniques. However, the space required for an EBG structure due to its larger size puts a limitation on the design of a compact antenna array. The major contributions of this paper include the design of a novel meander line structure for miniaturization of patch antenna as well as EBG structure. The design process is generalized and can be applied to design a compact patch antenna at any other operating frequency.

In section II, the design of a compact patch antenna is presented. Section III demonstrates the design of a compact EBG structure and a compact array with EBG structure. The findings are discussed in Section IV.

Finally, Section V gives the concluding remarks.

TABLE I
COMPARISON OF ISOLATION ENHANCEMENT TECHNIQUES

COMPARISON OF ISOEPHION ENTRANCEMENT TECHNIQUES					
Isolation technique	Size of antenna array	Isolation level			
Defected Ground Structure	Medium	Average			
Stub loading	Large	Low			
Neutralization Line	Medium	Average			
Electromagnetic Band Gap	Large	Excellent			
Meta material	Smallest	Average			
Shorting Pins	Small	Average			

Copyright © 2020 Praise Worthy Prize S.r.l. - All rights reserved

II. Design of Compact Patch Antenna

The design of the compact antenna initiates with the design of a conventional rectangular microstrip antenna, which is the most popular in literature. The conventional patch antenna has overall dimensions of 48 mm×50 mm, derived from standard equations in [15]. However, a conventional patch antenna proves to be an unsuitable candidate for an array element due to its large size. The size of a patch antenna limits the maximum spatial distance between adjacent elements of an array antenna placed in compact wireless devices. The spatial distance between two antenna elements is directly proportional to mutual coupling; the lower the distance is, the more is the mutual coupling [1]. This increased mutual coupling results in the degradation of antenna array performance.

Hence, in order to prove it as a good candidate for antenna array, the size of the conventional antenna has to be minimized. A compact patch antenna [28]-[30] can be achieved by the design of patch antenna with high permittivity dielectric substrate [16], cutting a slot in the radiating patch [17], or modified ground plane (Destructive Ground Surface) [18]. In this work, a novel approach of introducing meander line structure in conventional microstrip patch antenna is proposed to offer a compact patch antenna with half of the dimensions of the conventional patch. The proposed technique gives rise to the compact antenna with dimensions of L=20 mm, W=28 mm, and height H=1.6 mm for the substrate as depicted in Fig. 1. The patch dimensions are optimized to l=16.5 mm, w=20 mm, the spacing between meander line arms S=2.25 mm and width of meander line arm d=1 mm. When meander line slots are cut along the surface of the rectangular patch, the electric and magnetic field modifies due to the extension of length for the surface current flowing around the slots. The current mostly gathers at edges of the slots and thus results in the increased current path as compared to conventional patch. The resonant frequency is a function of surface current length. It is interestingly noted that as the length of the current path increases the resonant frequency decreases.

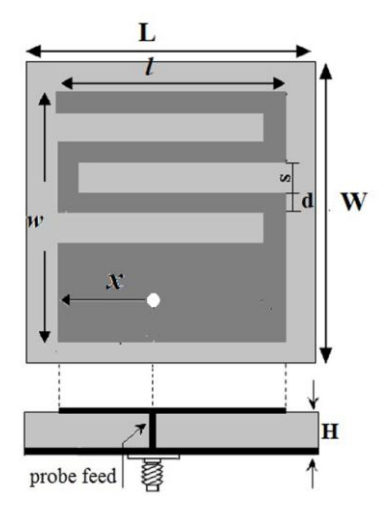


Fig. 1. Proposed patch antenna

The miniaturization of the conventional patch antenna can also be clarified with the help of the equivalent circuit diagram depicted in Fig. 2. It presents a broad guideline in the design of the compact antenna. The equivalent circuit diagram of the proposed patch antenna consists of a parallel combination of resistance (R), inductance (L) of the conventional patch in series with a new inductance (Ln), and capacitance (C) of a conventional patch in parallel with new capacitance Cn.

The new inductance and the capacitance are introduced in a conventional circuit due to the meander line slot introduced in the conventional patch. This gives rise to overall inductance to LT=L+Ln and overall capacitance to CT=C+Cn. The value of Ln can be computed as Ln=Ls+Lm given in [19]. Ls corresponds to self-inductance of a single meander line structure, whereas Lm symbolizes mutual inductance between two meander line structures. Both the self-inductance and the mutual inductance can be computed from the simple mathematical expressions readily available in the literature [19]. The capacitance Cn between adjoining meander line arms can be obtained from the mathematical relation between the surface area of meander line arm (A), the spacing between adjoining meander line arms (S), and the permittivity of the free space. Based on the aforementioned findings, some sensitive parameters are investigated to tune the performance of the proposed compact antenna. The variation of the resonant frequency with length l of meander line arm is demonstrated in Fig. 3. Whereas, the variation of resonant frequency with spacing between adjoining meander line arms S is demonstrated in Fig. 4.

The resonant frequency increases as both the length l and spacing s decrease, which verifies the above-mentioned theoretical analysis of the equivalent circuit diagram. Both the parameters are optimized in order to yield the operation of the proposed patch antenna at 2.4 GHz frequency.

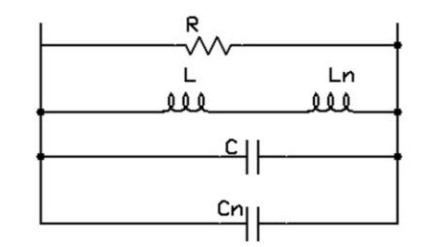


Fig. 2. Equivalent circuit diagram of proposed patch antenna

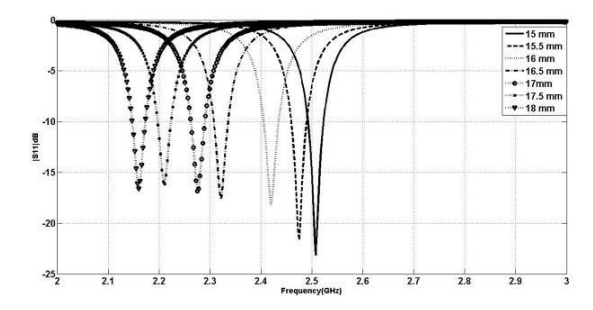


Fig. 3. Variation of resonant frequency with length (l)

Copyright © 2020 Praise Worthy Prize S.r.l. - All rights reserved

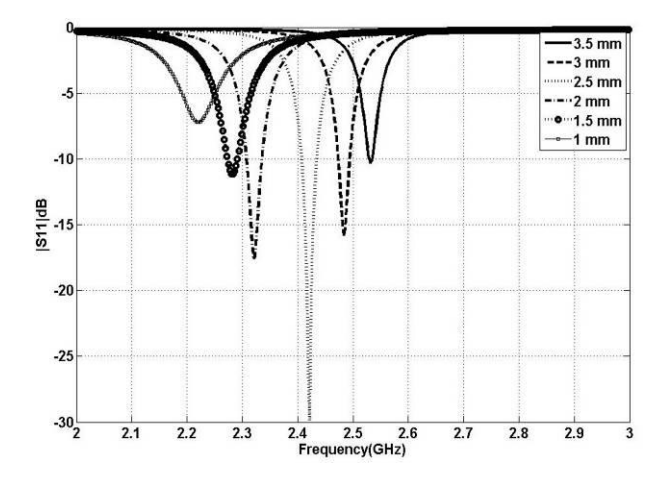


Fig. 4. Variation of resonant frequency with gap (S)

III. Design of Compact Patch Antenna Array

In the next step, a two-element antenna array etched on one end of the FR4 substrate and ground plane on the other is presented. The input signal applied to one of the elements in the antenna array couples to the adjoining element through the presence of a common substrate and ground plane.

The spatial diversity plays a key role in controlling the mutual coupling between ports of antenna elements. Hence, a trade-off exists between the mutual coupling and compact size of the array antenna.

Thankfully, the novel compact antenna design discussed in Section II acts as a decoupling structure.

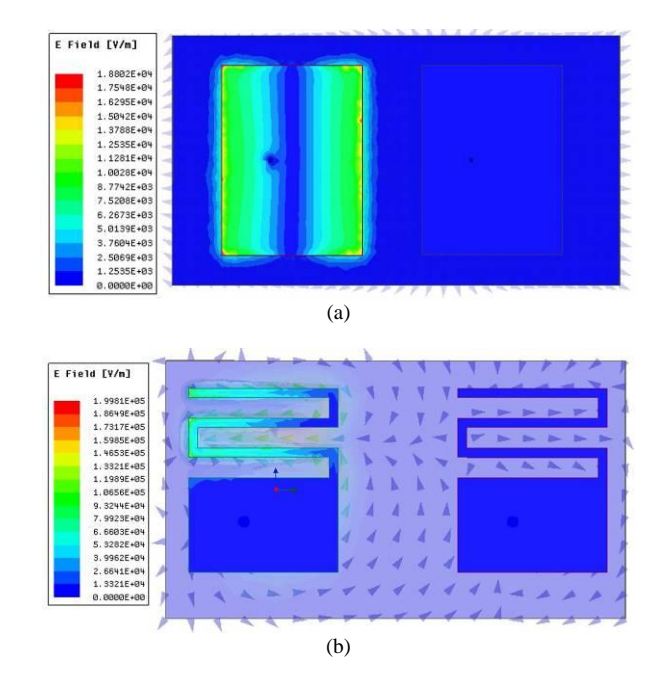
The novel antenna itself gives an improvement in the mutual coupling of about 20 dB. The mutual coupling is further reduced by the introduction of a meander line slot EBG layer in the array [20]-[22].

III.1. Spatial Diversity For Compact Patch Antenna Array

The meander line slot concentrates the current opposite to the plane of the coupled antenna as depicted in Fig. 5(b).

On the contrary, the conventional element antenna array reported in [23] concentrates the current on the edge near to coupled antenna as demonstrated in Fig. 5(a), giving rise to higher mutual coupling. This effect is examined thoroughly through experimentation as depicted in Fig. 6.

The mutual coupling increases as the separation distance between two antenna elements decreases. In addition, the mutual coupling is twice greater for antenna array of conventional antenna elements than the array of the proposed antenna elements for the same separation distance, as verified from the results seen in Fig. 6. The spatial separation for the proposed antenna array is optimized to a one-tenth value of lambda, portraying a compact size antenna array of the dimensions of 50mm×28 mm.



Figs. 5. (a) Current distribution for conventional array (b) Current distribution for proposed antenna array

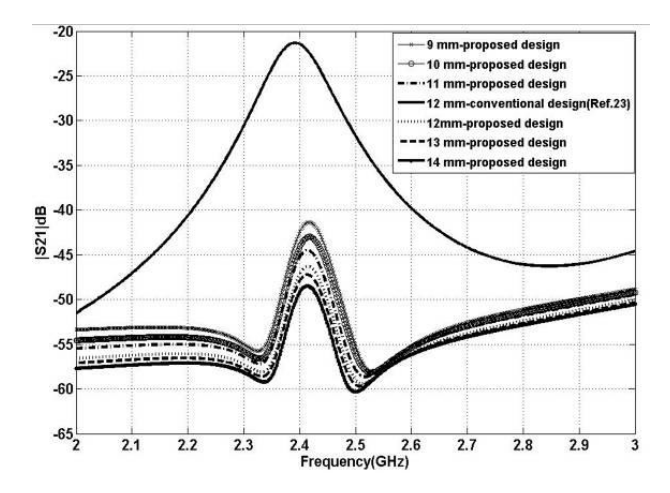


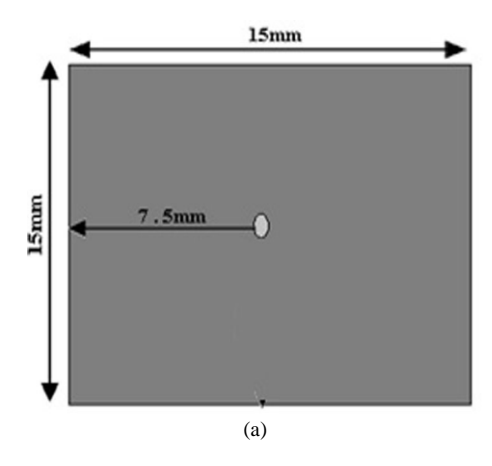
Fig. 6. Mutual coupling variation with spatial separation

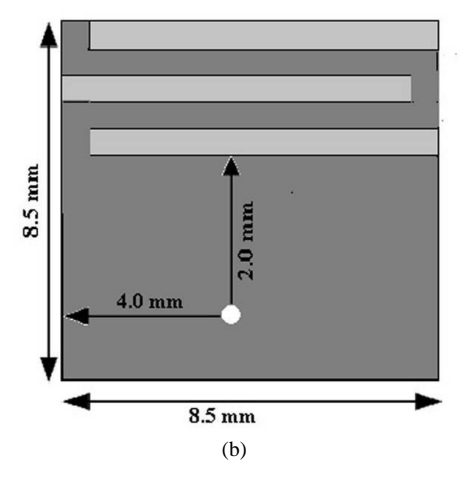
III.2. Design of Compact EBG Structure

Based on the abovementioned consideration, a compact electromagnetic band gap structure is investigated thoroughly and designed to reduce the mutual coupling. The EBG structure outperforms its counterparts in mutual coupling reduction between antenna array elements as discussed in section I.

However, the size of a single unit of conventional EBG cell is quite large and makes it unfit for compact devices. A single unit cell of a conventional EBG consists of a dielectric substrate sandwiched between a metallic patch and ground as depicted in Fig. 7(a). A connecting via is drilled to connect the patch and the ground plane. The single unit of conventional EBG is designed with commercially available substrate FR4. The length L_E and the width W_E of the unit cell of conventional EBG is obtained from equation (1).

 $Copyright © 2020 \ Praise \ Worthy \ Prize \ S.r.l. \ - All \ rights \ reserved$





Figs. 7. (a) Conventional mushroom EBG (b) Proposed meander line slot EBG

Whereas, connecting via diameter d_E is calculated from equation (2):

$$L_E = W_E = 0.12\lambda_0 \tag{1}$$

where λ_0 is the free space wavelength determined for the given band gap frequency for an EBG element:

$$d_E = 2 \times 0.005 \lambda_0 \tag{2}$$

The current in a single unit of EBG is initially induced in the metallic patch. Then it flows to the other units present in a layer prearranged in a periodic manner. The current is passed to the round element through a connecting patch via and the ground. The outcome of this cumulative action leads to a buildup of charge in the EBG layer. The stop band frequency f_b is controlled by this equivalent capacitance C_e and the equivalent inductance L_e and is given as:

$$f_b = \frac{1}{\sqrt{(L_e \times C_e)}} \tag{3}$$

The equivalent inductance L_e is controlled by the inductance created due to the connected via between the

patch element and the ground. The charge accumulated in the dielectric, patch, and ground controls the equivalent capacitor C_e .

One potential way to reduce the size of the conventional EBG is to increase its equivalent inductance or capacitance as indicated by equation (1). The band stop frequency of an EBG can be controlled by controlling the value of L_e and C_e .

This, in turn, will enable the designer to control dimensions of a unit cell of EBG as directed by equation (3). Based on the discussion, the design of a meander line slot EBG, half the dimensions of conventional EBG is presented in Fig. 7(b).

Thus, the proposed compact EBG enables the inclusion of a double number of EBG elements in the same space occupied by conventional EBG elements.

The dimensions of the meander line slot EBG depicted in Fig. 7(b) are optimized using EM simulation software HFSS. In order to verify further the stop band ability of proposed EBG structure, a very powerful analysis tool named dispersion diagram is used [24]. Dispersion diagram makes use of the brillouin diagram to derive the stop-band in a periodic EBG layer. The brillouin diagram was computed with the eigen mode solver within the Ansoft High Frequency Structure Simulator (HFSSTM) software. The dispersion diagram of the proposed meander line slot EBG is depicted in Fig. 8, computed along the edges of the irreducible brillouin zone. The diagram reveals the presence of stop band at 2.4 GHz band.

III.3. Compact Antenna Array with Meander Line EBG Structure

An EBG layer with 3 EBG elements as seen in Fig. 9(a) is etched at the midpoint of spacing between antenna elements. The proposed EBG structure occupies a very little area compared to its counterparts. The gap between two adjoining EBG elements is optimized to 0.5 mm.

The EBG layer serves as a stop band to the inter port coupling between the two antenna elements of the array. This results in the mutual coupling reduction of about 10 dB giving rise to an overall mutual coupling value less than 55 dB as depicted in Fig. 9(b).

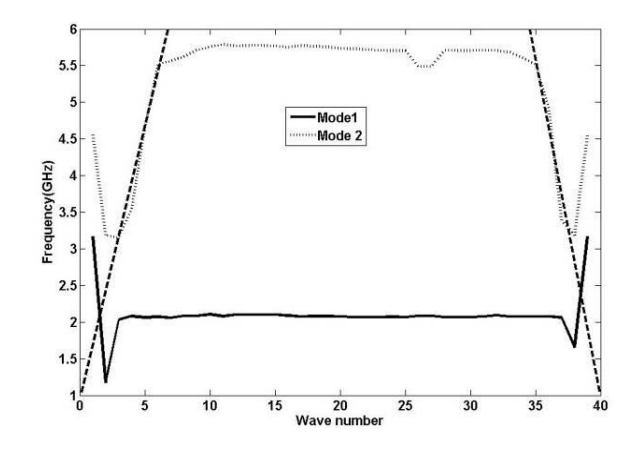
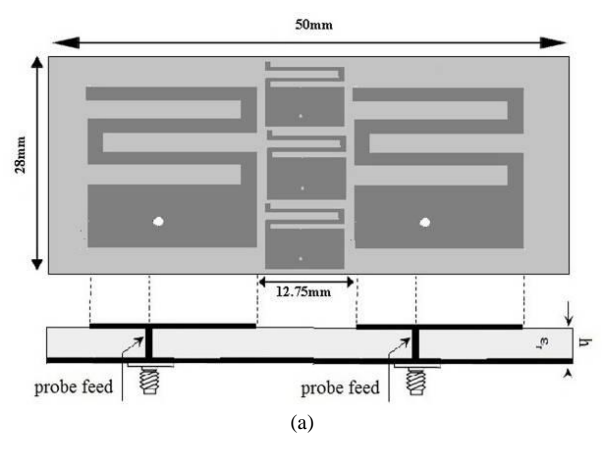
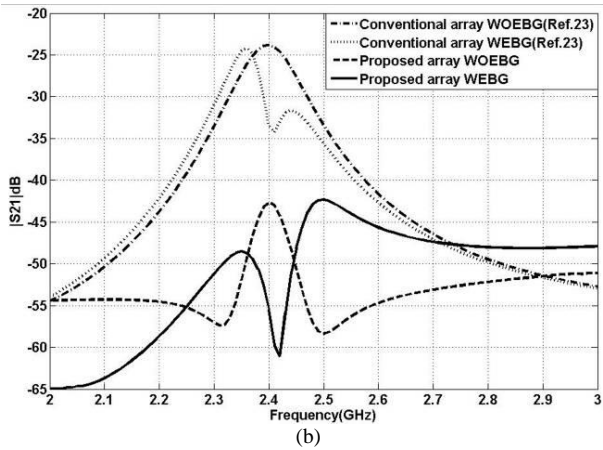


Fig. 8. Dispersion diagram for meander line slot EBG

Copyright © 2020 Praise Worthy Prize S.r.l. - All rights reserved





Figs. 9. (a) Compact array with meander line slot EBG (b) Comparison of mutual coupling with meander line embedded antenna array

IV. Results and Discussions

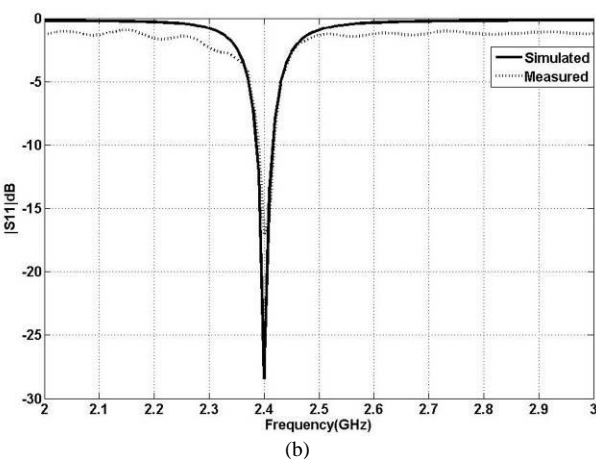
IV.1. Reflection Coefficient (S_{11})

An excellent agreement between the theoretical and the practical investigations carried out on the proposed antenna provides a deep insight into the functioning of the proposed compact antenna. A model of the proposed compact antenna has been fabricated on an FR4 substrate with a thickness of 1.6 mm and a relative permittivity of 4.4. The top view of the manufactured structure is shown in Fig. 10(a).

The performance of the prototype is validated by testing it with a 2-port Rhode and Schwartz Vector Network Analyzer. The simulated reflection coefficient (S11) is acquired from ANSYS HFSS simulation software.

The reflection coefficient parameter derived from the simulation of the antenna and the ones measured from the test are plotted in Fig. 10(b). The results confirm that the simulated reflection coefficient is lower than 10 dB in the desired band. The measured data shows a good agreement with the simulated one. The manufactured prototype is of half the dimensions of the conventional patch antenna. Nevertheless, a modest difference in simulated and measured results is observed due to the manufacturing defects.





Figs. 10. (a) Top view of prototype of compact patch antenna (b) Comparison of simulated and measured reflection coefficient

IV.2. Mutual Coupling

The introduction of meander line slot EBG results in the enhancement of isolation between port 1 and 2 of the antenna array.

For the experimental validation of the simulated results as showcased in section III, an antenna array with meander line slot EBG structure has been fabricated as seen in Fig. 11(a) and it has been also tested with a two-port vector network analyzer. The comparison of measured and simulated scattering parameters is depicted in Fig. 11(b). It is observed that isolation between ports is well below 52 dB by measurement and 55 dB by simulation. A slight variation of the measured result is seen compared to simulated ones. This variation can be accepted within the tolerance value.

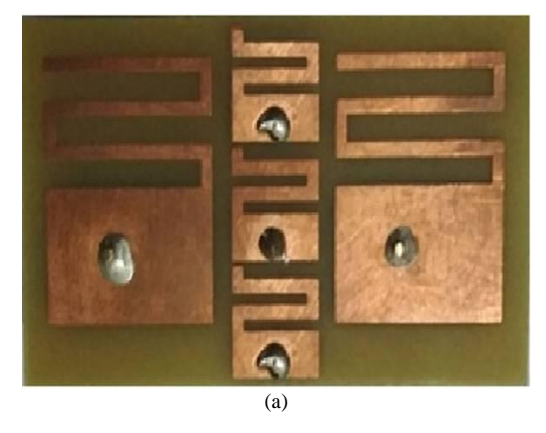
IV.3. Envelope Correlation Coefficient (ECC)

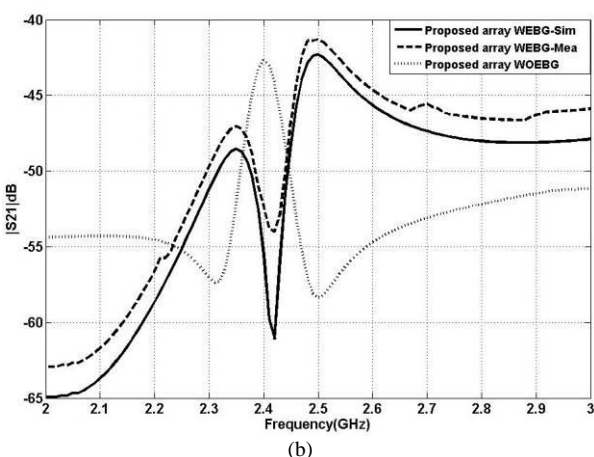
The Envelope Correlation Coefficient (ECC) plays a very significant role in determining the diversity performance of the MIMO antenna array. The satisfactory limit of ECC for excellent diversity performance is below 0.5. The ECC value is derived from the measured S-parameters by the following equation (4):

Copyright © 2020 Praise Worthy Prize S.r.l. - All rights reserved

$$ECC = \frac{\left|S11^*S12 + S21^*S22\right|^2}{\left(\left(1 - \left|S11\right|^2 - \left|S21\right|^2\right)\left(1 - \left|S22\right|^2 - \left|S12\right|^2\right)\right)}$$
(4)

where S11 and S22 are return loss values for port one and port two respectively, while S21 and S12 denote the inter port coupling of the array antenna. The ECC value calculated from the measured S parameters is depicted in Fig. 12. The value of ECC in the frequency range of operation is lower than 0.19. This ensures an efficient performance of the proposed array.





Figs. 11. (a) Top view of prototype of compact patch antenna array (b) comparison of simulated and measured mutual coupling

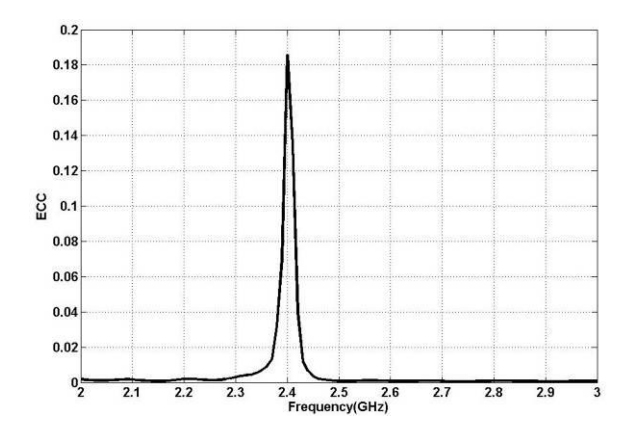


Fig. 12. Variation of measured value of ECC with frequency

Copyright © 2020 Praise Worthy Prize S.r.l. - All rights reserved

IV.4. Total Active Reflection Coefficient (TARC)

TARC is a measurement of both isolation and diversity performance of a MIMO antenna array. It is derived from total reflected power and total incident power.

TARC value is obtained from measured S parameters.

The average TARC value derived from measured scattering parameters is shown in Fig. 13. It is well below the threshold value of 30 dB that ensures a good MIMO performance.

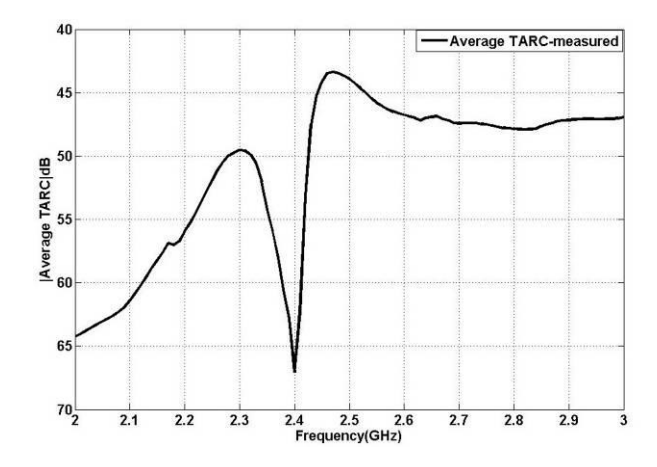


Fig. 13. Variation of measured average TARC with frequency

IV.5. Diversity Gains (DG) and Mean Effective Gain (MEG)

Diversity gain is one of the most important parameters for verification of diversity performance of MIMO antenna array and it is given as:

$$DG = 10 \times \sqrt{1 - \left| 0.99 \times ECC \right|^2} \tag{5}$$

Its maximum value obtained for a practical MIMO antenna array is 10 dB. The proposed antenna array displays a DG value of 9.9 dB from simulation and 9.8 dB from measured results as demonstrated in Fig. 14.

MEG is again a crucial parameter for assessing the diversity performance of the MIMO antenna array. It is typically defined relative to an isotropic antenna.

Mathematically, it is given as:

$$MEG_i = 0.5 \times \left(1 - \sum_{j=1}^{N} \left| S_{ij} \right|^2 \right)$$
 (6)

where i represents port at which MEG is measured and N the number of the antenna elements. The ideal ratio of mean effective gain calculated for antenna element 1 and antenna element 2 of the two-element antenna array is unity.

The calculated ratio *MEG1/MEG2* or the proposed two-element antenna array is 0.97 from measured data and 0.98 from simulated data.

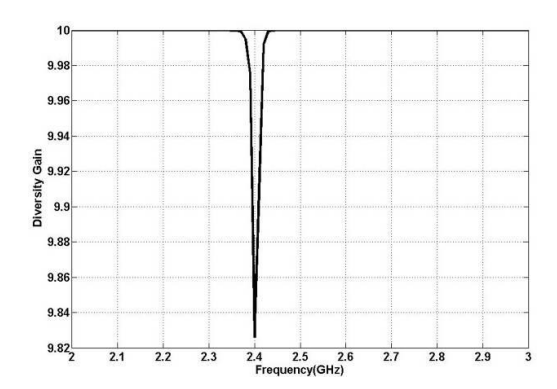
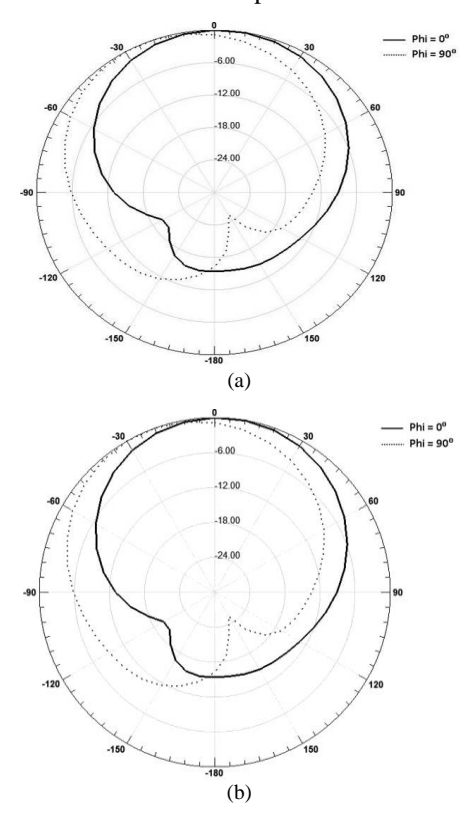


Fig. 14. Variation of DG with frequency

IV.6. Radiation Pattern

The individual antenna element in a proposed array is designed to exhibit a broadside radiation pattern. Fig. 15(a) and Fig. 15(b) show the simulated gain pattern, which changes with θ from 0° to 360° both on the $\phi{=}0^\circ$ (E Plane) and $\phi{=}90^\circ$ (H plane). The nature of the radiation pattern in the E-plane is directed in a broadside direction. The radiation plot in Fig. 15(a) is plotted for the antenna without the insertion of the EBG array in the antenna elements. Whereas, the radiation plot in Fig. 15(b) is plotted for the antenna with the insertion of EBG array. The radiation with EBG shows an improved copolarized pattern due to a reduction in mutual coupling. Due to the symmetry property of the antenna at the other port exhibits similar radiation patterns.



Figs. 15. (a) Radiation pattern without EBG (b) Radiation pattern with EBG

For the validation of the results, a comparison of the proposed design results and previous design found in literature has been done and findings have been tabulated in Table II. The value of δ_0 is calculated from the lowermost operating frequency to incase of the multiband antenna. As seen from the comparison in Table II, the proposed design offers high isolation and compact design compared to the conventional design and other designs reported in the literature. The meander line structure gives a complete solution for both the design of compact patch antenna element and compact EBG structures providing a compact high isolation antenna array. The design process is simple, generalized and it is easily possible for an antenna designer to replicate the design of the proposed antenna array for any operating frequency for a given application.

TABLE II
COMPARISON OF THE PROPOSED DESIGN RESULTS

WITH PREVIOUS DESIGNS						
References	Size of antenna array(λ ₀)	Design process	Isolation level in dB			
Conventional design [23]	$0.73\lambda_0 \times 0.40\lambda_0$	Simple	32			
[25]	$1.41\lambda_0 \times 0.67\lambda_0$	Complex	50			
[26]	$0.73\lambda_0 \times 0.40\lambda_0$	Complex	30			
[27]	$0.48\lambda_0 \times 0.36\lambda_0$	Complex	30			
Proposed design	$0.40\lambda_0 \times 0.2\lambda_0$	Simple	52			

V. Conclusion

A compact MIMO antenna array for 2.4 GHz band is designed and tested against various parameters for the certainty of its performance in a MIMO environment.

The introduction of a novel meander line structure results in a compact antenna array. The proposed antenna array has the advantages of lower cost, ease in manufacture, compact size, and high isolation.

Consequently, the proposed design is a good candidate for compact wireless devices working in a MIMO environment and it outperforms its counterparts.

References

- Arny Adila Salwa Ali and Sharlene Thiagarajah, A Review on MIMO Antennas Employing Diversity Techniques, *Proc. ICEE I Conf.*, pp. 388-391, 2007.
- [2] Hari Shankar Singh, Mayank Agarwal, Gaurav Kumar Pandey and Manoj Kumar Meshram, A Quad-Band Compact Diversity Antenna for GPS L1/WiFi/LTE2500/WiMAX/HIPERLAN1 Applications, *IEEE Antennas and Wireless Propagation Letters*, Volume 13, January 2014, Pages 429-252.
- [3] Beegum S. Femina and Sanjeev K. Mishra, Compact WLAN Band-notched Printed Ultrawideband MIMO Antenna with Polarization Diversity, Progress In Electromagnetics Research C, Volume 61, January 2016, Pages 149–159.
- [4] Yashika Sharma, Debdeep Sarkar, Kushmanda Saurav and Kumar Srivastava, Three Element MIMO Antenna System with Pattern and Polarization Diversity for WLAN Applications, *IEEE Antennas and Wireless Propagation Letters*, Volume 16, Novenber 2016, Pages 1163-1166.
- [5] Zicheng Niu, Hou Zhang, Qiang Chen and Tao Zhong, Isolation Enhancement for 1 _ 3 Closely Spaced E-Plane Patch Antenna Array Using Defect Ground Structure and Metal-Vias, *IEEE Access*, Volume 7, August 2019, Pages 119375-119383.

 $Copyright © 2020 \ Praise \ Worthy \ Prize \ S.r.l. \ - All \ rights \ reserved$

- [6] Juin Acharjee, Kaushik Mandal and Sujit Kumar Mandal, Reduction of Mutual Coupling and Cross- Polarization of a MIMO/Diversity Antenna using a String of H-Shaped DGS, International Journal of Electronics and Communications, Volume97, December 2018, Pages 110-119.
- [7] Mohammadmahdi F, Javad P, Mohammad A, Mourad N, Abdel S and Tayeb D, Mutual Coupling Reduction in Millimeter-Wave MIMO Antenna Array Using a Metamaterial Polarization-Rotator Wall, *IEEE Antennas and Wireless Propagation Letters*, Volume 16, June 2017, Pages 2324–2327.
- [8] Robert Mark, Neha Rajak, Kaushik Mandal and Soma Das, Metamaterial based superstrate towards the isolation and gain enhancement of MIMO antenna for WLAN application, International Journal of Electronics and Communications, Volume 100, February 2019, Pages 144-152.
- [9] Amjad Iqbal, Omar Saraereh, Arbab Ahmad and Shahid Bashir, Mutual Coupling Reduction Using F-Shaped Stubs in UWB-MIMO Antenna, *IEEE Access*, Volume 6, Feb. 2018, Pages 2755-2759
- [10] Mohannad Obaid Katie, Mohd Faizal Jamlos, Abdulrahman Shueai Mohsen Alqadami and Mohd Aminudin Jamlos, Isolation Enhancement of Compact Dual-Wideband MIMO Antenna Using Flag-Shaped Stub, Microwave and Optical Technology Letters, Volume 59, May 2017, Pages 1028-1032.
- [11] Rakesh N. Tiwari, Prabhakar Singh and Binod K. Kanaujia, A compact UWB MIMO antenna with neutralization line for WLAN/ISM/mobile applications, Int J RF Microw Comput Aided Eng, Volume 29, July 2019, Pages 1-9.
- [12] Hari S. Singh, Bhaskara reddy Meruva, Gaurav K. Pandey, Pradutt K. Bharti, and Manoj K. Meshram, Low Mutual Coupling Between MIMO Antennas By Using Two Folded Shorting Strips, Progress In Electromagnetics Research B, Volume 53, January 2013, Pages 205–221.
- [13] Nagendra kushwaha1 and Raj Kumar, Study of Different Shape Electromagnetic Band Gap (EBG) Structures for Single and Dualband Applications, Journal of Microwaves, Optoelectronics and Electromagnetic Applications, Volume 13, June2014, Pages 16-30.
- [14] Mohammad Naderi, Ferdows B. Zarrabi, Fereshteh Sadat Jafari and Speideh Ebrahimi, Fractal EBG Structure for shielding and reducing the mutual coupling in microstrip patch antenna array, *International Journal of Electronics and Communications*, Volume 93, September 2018, Pages261-267.
- [15] Girish Kumar and K.P.Ray, *Broadband Microstrip Antennas* (Artech House, 2003, pp. 205-248).
- [16] Takeshi Fukusako and Toshihide Nakano, A compact patch antenna using artificial ground structure with high permittivity substrate, IEEE-APS Topical Conference on Antennas and Propagation in Wireless Communications, pp.7-11 Sept. 2015.
- [17] F. Jolani and A. M. Dadgarpour, Compact M-slot Folded Patch antenna for WLAN, *Progress In Electromagnetics Research Letters*, Volume 3, January 2008, Pages 35–42.
- [18] Nataraj, D., Karunakar, G., Compact Printed Elliptical Microstrip Patch with Defected Ground Structure (DGS) for Wireless Applications, (2018) International Journal on Communications Antenna and Propagation (IRECAP), 8 (3), pp. 271-276. doi: https://doi.org/10.15866/irecap.v8i3.12858
- [19] Ryouhei Hosono, Ning Guan, Hiroiku Tayama and Hirotaka Furuya, An Equivalent Circuit Model for Meander-line Monopole Antenna Attached to Metallic Plate, *Proceedings of ISAP2012*, Japan, pp.1421-1424, 2012.
- [20] Qian Li, Alexandros P. Feresidis, Marina Mavridou and Peter S. Hall, Miniaturized Double-Layer EBG Structures for Broadband Mutual Coupling Reduction Between UWB Monopoles, *IEEE transactions on Antennas and Propagation*, Volume 63, March 2015, Pages 1168-1171.
- [21] K.Vasu Babu, B.Anuradha and Chandra Bhushana Rao, Reduction of Mutual coupling by desegregated with EBG Structure for Microstrip Antenna Array Radar Applications, Int. Conf. Signal Processing, Communication, Power and Embedded System, pp.1-3, 2016.
- [22] Alaa H. Radhi, Nur Ab Aziz, R. Nilavalan and H. S. Al-Raweshidy, Mutual Coupling Reduction Between Two PIFA Using Uni-Planar Fractal Based EBG for MIMO Application,

- Int. Conf., Loughborough Antennas & Propagation, pp.1-5, 2016.
- [23] M. B. Kadu and Dr. Neela Rayavarapu, Design of EBG Structure for Mutual Coupling Reduction in Patch Antenna Array, Int. Conf. Advances in Communication and Computing Technology, February 2018.
- [24] Yoshitaka Toyota, Arif Ege Engin, Tae Hong Kim and Kazuhide Uriu, Stopband Prediction with Dispersion Diagram for Electromagnetic Bandgap Structures in Printed Circuit Boards, Proc. Int. Symposium on Electromagnetric Compability. pp. 807-811 2006
- [25] Sumantra Chaudhuri, Rakhesh Singh Kshetrimayu and Ramesh Kumar Sonkar, High inter-port isolation dual circularly polarized slot antenna with split-ring resonator based novel metasurface, *International Journal of Electronics and Communications*, May 2019. Pages 146-156.
- [26] Kang Ding, Cheng Gao, Dexin Qu and Qin Yin, Compact Broadband MIMO Antenna with Parasitic Strip, IEEE Antennas and Wireless Propagation Letters, Volume 16, December 2016, Pages 1468–1471.
- [27] Murtala Aminu-Baba1, Mohammad Kamal A. Rahim, Farid Zubir1, Adamu Y. Iliyasu1, Mohd Fairus, Mohd Yusoff, K. I. Jahun and Osman Ayop, Compact Patch MIMO Antenna antennas With Low Mutual coupling For WLAN Applications, *Journal of electrical Engineeering*, Volume 18, January 2019, Pages 43-46.
- [28] Hadj Sadok, M., Lamhene, Y., Berkani, S., Baudrand, H., Comparison Between Several EBG 3 D Structures to Improve Antenna Performances of Two Patches, (2020) International Journal on Communications Antenna and Propagation (IRECAP), 10 (1), pp. 31-36. doi: https://doi.org/10.15866/irecap.v10i1.16471
- [29] Kumar, K., Pavani, M., Design of a Compact Rectangular Patch Antenna Using Defected Ground Structure, (2017) International Journal on Communications Antenna and Propagation (IRECAP), 7 (4), pp. 282-289. doi: https://doi.org/10.15866/irecap.v7i4.12389
- [30] Konkyana, V., Sudhakar, A., Design and Analysis of Dual Notch Band Ultra-Wide Band Antenna Using Complementary Split Ring Resonator for Wireless Applications, (2019) *International Journal on Engineering Applications (IREA)*, 7 (3), pp. 72-80. doi:https://doi.org/10.15866/irea.v7i3.16906

Authors' information

¹Symbiosis International (Deemed University), Lavale, Pune, India.

²Symbiosis Institute of Technology, Symbiosis International University, Symbiosis International (Deemed University), Lavale, Pune, India.



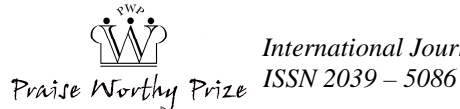
Mahesh B. Kadu is currently assistant professor in Electronics and Telecommunication Department of Amrutvahini COE, Sangamner, MS, India. He is PhD research scholar at Symbiosis International (Deemed University), Lavale, Pune, India since 2015.



Dr. Neela Rayavarapu is currently head Electronics and Telecommunication department and professor in Symbiosis Institute of Technology, Symbiosis International (Deemed University), Lavale, Pune, India.She is a registered PhD guide with Electronics and Telecommunication Department, Symbiosis Institute of Technology, Symbiosis International

 $(Deemed\ University),\ Lavale,\ Pune,\ India.$

Copyright © 2020 Praise Worthy Prize S.r.l. - All rights reserved



Network Lifetime Evaluation in Heterogeneous WSN with Different Node Placement Distributions

Yousef Jaradat¹, Mohammad Masoud², Dema Zeidan³

Abstract – In this paper, the effect of different node placement strategies on maximizing the lifetime of heterogeneous wireless sensor network is investigated. Normal, exponential, and uniform node placement distributions are utilized. Maximum likelihood estimation technique and the locations of nodes with uniform distribution are utilized to estimate the defining parameters of the normal and the exponential distributions. Stable Election Protocol (SEP) and LEACH protocols are used to evaluate the performance of different node location distributions in terms of stability and instability periods, network lifetime and throughput. It has been noticed that different node distributions have almost the same stable and unstable regions in SEP protocol with the same heterogeneity parameters. Moreover, an improvement of 25% in stability region is noticed in SEP protocol with uniform and normal distributions compared to LEACH protocol with the same heterogeneity parameters. Likewise, an improvement of 30% is noticed in stability region of the exponential distribution compared to LEACH protocol with the same heterogeneity parameters. It has been also shown that normal distribution has a slightly larger throughput compared to the uniform and exponential distributions. Copyright © 2020 Praise Worthy Prize S.r.l. - All rights reserved.

Keywords: Wireless Sensors Networks (WSN), SEP, MLE, Heterogeneous WSN

Nomenclature

E_{normal}	Energy in a normal node
$E_{advance}$	Energy in an advance node
E_{net}	Net energy in the heterogeneous network
E_o	Initial energy storage of a node
E_{elec}	Energy consumed by the RF circuitry per
	bit
E_{TX}	Total energy consumed by the TX
$E_{TX\text{-}elec}$	Energy consumed by the TX for <i>k</i> bits
E_{TX-amp}	Energy consumed by the TX amplifier
E_{RX}	Total energy consumed by the receiver
$E_{RX\text{-}elec}$	Energy consumed by the receiver circuitry
n	Total number of nodes in the network
m	A percentage of advance nodes
α	% of extra energy in the advance nodes
μ	Mean of the nodes location
k	Number of bits in a packet
\mathcal{E}_{fs}	Free space amplification model
\mathcal{E}_{mp}	Multipath amplification model
d_o	Threshold distance to switch between free
	space and multipath models
HO-WSN	Homogeneous WSN
HE-WSN	Heterogeneous WSN
SEP	Stable Election Protocol
LEACH	Low Energy Adaptive Clustering
	Hierarchy
CH	Cluster Head

I. Introduction

Wireless Sensor Network (WSN) is a network of small battery-powered sensor nodes [1]. Typical sensor nodes are deployed randomly and uniformly in a target field. The purpose of sensor nodes is to sense the region in which they have been deployed. Moreover, the sensed data is processed locally and transmitted to centralized processing node usually called the sink or the Base Station (BS). Data communication is one of the major functions done by a sensor node. Usually, data communication consumes a huge amount of energy compared to other tasks done by a sensor node [2].

However, the design of WSN communication protocols and applications should be energy-aware and efficient in order to extend the life span of the network since the replacement of energy sources in these nodes are hard and sometimes impossible once they have deployed. WSNs are used everywhere these days. They can be used in industry, agriculture, cities, homes, mines, commerce, military, and a collection of monitoring applications [3], [22], [23]. WSN nodes are deployed usually in large-scale depending on the application of interest [4].

Clustering algorithms are used intensively in routing data to the sink node [5] [18]-[21]. The importance of clustering algorithms in WSNs stems from the fact that they are energy efficient and as a result prolonging the lifetime of the network by balancing energy expenditure across network sensor nodes. The basic operation of

Member Node

MN

clustering protocols is to divide sensor nodes into clusters. Every cluster consists of a number of Member Nodes (MN) and a Cluster Head (CH). MNs send their data to their corresponding CH, which, in turns aggregates, compresses and transmits data to the BS directly or through multi-hop approach [6]. The formation of clusters and the election process of CH are done continuously in protocol rounds. All the nodes become CHs in different rounds to balance energies among them in order to prevent quick nodes' death. An epoch is defined as the sequence of rounds in which all the network nodes serve as CHs. In this way, energy expenditure is distributed equally among different epochs and as a result, network lifetime is prolonged. Low Energy Adaptive Clustering Hierarchy (LEACH) [7] and Stable Election Protocol (SEP) [8] are typical examples of clustering algorithms. Two types of WSNs are usually studied: Homogeneous and heterogeneous. homogeneous WSN (HO-WSN), sensor nodes are identical in their structure, sensors, computation, and energy [9]. In heterogeneous WSN (HE-WSN), nodes have different capabilities, structure, computation, and energy [8]. In this paper, heterogeneity is limited to the energy source. A percentage of nodes (m) are supplied with more energy than other ones. Nodes with more energy than others are referred to as advanced nodes; other nodes are referred to as normal nodes. In many research studies, nodes' locations are distributed uniformly in HO-WSN or HE-WSN [10], [11]. No location is preferred than another. All the locations in the network field are likely to have a sensor node. In some network settings, nodes are distributed according to other distributions. This mainly depends on the application of WSN, terrain of the field and the required quality of service. In this paper, normal and exponential node distributions a long with the uniform distribution are used to study the impact of different node distributions on energy expenditure, network lifetime of HE-WSNs.

The rest of the paper is organized as the follows. Related work is overviewed in Section II. Models and assumptions are described in Section III. Section IV provides simulation settings and results. Finally, this research is concluded in Section V.

II. Related Work

A number of research studies have been conducted regarding node deployment strategies in WSN environment. The authors in [12] have studied maximization of WSN lifetime per unit cost; this metric is defined as the network lifespan divided by the number of nodes in the network. The authors in [13] have formulated a nonlinear optimization problem in order to determine the optimal nodes' distributions for efficient energy utilization. The authors in [14] have showed that in tough-terrain fields the probabilistic distribution of nodes has performed better than the uniform distribution in terms of intrusion detection, network lifetime, and routing protocol stability. In [15] the authors have proved

mathematically that normal distribution of sensor nodes improves intrusion detection probability for a target field.

The authors in [16] have carried out a comparative simulation-based study for node deployment strategies using mixed, uniform and normal distributions. Their findings have indicated that normal placement of nodes outperforms other node placement strategies in terms of average hop count, intrusion detection and protocol control bits count. On the other hand, mixed node distribution has showed better results in reducing end-toend packet delay compared to other distributions. In [17], the author has showed that energy efficient routing protocols for maximizing the lifetime of WSN are improved utilizing node distributions following normal, Poisson, Chi-squared and uniform distributions. The authors in [18] have proposed a novel Harmony Memory Search based Energy Efficient Clustering (HMS-EEC) technique to improve the energy utilization in WSN network. In this scheme, CH is elected based on the distance and the delay time of the nodes. HMS-EEC results have showed a great improvement compared to other clustering techniques in terms of network lifetime and stability region. In [19], the authors have proposed two energy-efficient techniques for data transmission between CHs and the BS and the energy consumed during this operation. In the first scheme, CHs send their data to the BS through a middle sensor, namely, anchor.

In the other scheme, CHs send their data through multiple anchors. Their simulation experiments have showed a huge improvement in energy utilization in WSN. In [20], the authors have studied the impact of different node distributions on energy consumption in WSN. It has been shown that normal placement distribution outperforms uniform and exponential node distribution in terms of energy expenditure and throughput. In this work, the authors extend the work done in [20] by applying different node distributions in HE-WSN settings.

III. WSN Settings and Assumptions

The following models are assumed in this paper. The energy model is the same one used in [10].

III.1. SEP: Heterogeneous-Aware Clustering Protocol

Stable Election Protocol (SEP) [8] is a well-known clustering algorithm used specifically for HE-WSN.

Heterogeneity in energy capabilities introduces the problem of speed death of the network. The basic operation of the SEP protocol is to utilize the heterogeneity in energy storage of sensor nodes in order to prolong the lifetime of the WSN. In SEP, sensor nodes are divided into two categories: advanced and normal nodes. The advanced nodes represent a fraction (m) of the total number of nodes that have more energy (α) than the other normal nodes. If a normal node has a basic energy storage of E_o then an advance node will have $(1+\alpha)E_o$. The total energy in the HE-WSN is given by:

$$E_{net} = m \times n \times E_{advance} + (1 - m)n \times E_{normal}$$

$$= m \times n \times E_o \times (1 + \alpha)$$

$$+ (1 - m)n \times E_o = n \times E_o (1 + \alpha)$$
(1)

SEP utilizes the advanced nodes as CHs more than normal nodes in the same extended epoch compared to an epoch in HO-WSN. SEP divides a protocol extended epoch into h sub-epochs. Normal nodes are elected once in a protocol extended epoch while advanced nodes are elected h times. In this way, network energy expenditure is distributed efficiently by the nodes and the network lifetime is extended.

III.2. Node Distributions Parameters Estimation

This study utilizes three different node distributions in a network field, namely, uniform, normal, and exponential. The problem with distributions besides the uniform distribution is the particular distribution defining parameters. A solution to this problem is to utilize the Maximum Likelihood Estimation (MLE) technique. In this approach, nodes' locations are generated by the uniform distribution as all the information required by the distribution is provided, the information include the number of nodes and the dimensions of the network area. MLE utilizes the location information of the nodes provided by the uniform distribution and estimates the necessary parameters for the other two distributions.

Table I shows the necessary defining parameters required by the normal and exponential distributions. [18] provides a complete derivation of these parameters.

 x_i represents a random variable of node's positions.

III.3. Node Energy Communication Model

The main energy source of a sensor node is the battery. A node with more energy lives more compared to a node with less energy. HE-WSN lifetime depends mostly on the nodes' energies and the communication protocol used. A typical first order communication model used in HE-WSN is provided by Fig. 1 [20].

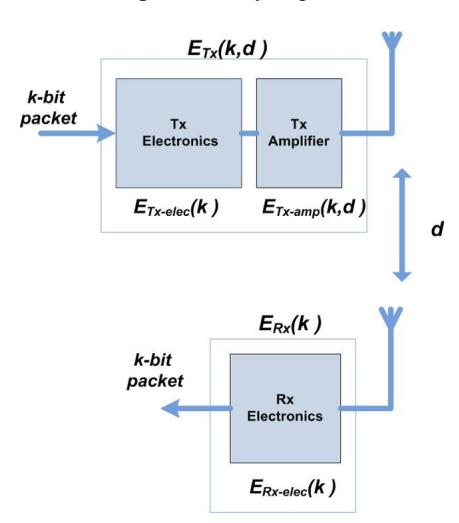


Fig. 1. Node communication model

Copyright © 2020 Praise Worthy Prize S.r.l. - All rights reserved

TABLE I
ESTIMATED DISTRIBUTION PARAMETERS

Distribution	Parameter 1	Parameter 2
Normal	$\mu = x = \frac{1}{n} \sum_{i=1}^{n} x_i$	$\sigma^2 = \frac{1}{n} \sum_{i=1}^{n} (x_i - x)^2$
Expoenential	$\lambda = \frac{n}{\sum_{i=1}^{n} x_i}$	- -

Fig. 1 shows a typical transceiver deployed in a sensor node. The transmitter side (TX) on one node communicates with the receiver side (RX) on the other node. The consumed energy depends on the distance between the two nodes (d) and the size of the transmitted data packet (k). Energy expended by the transmitter to processes and sense k-bit packet is given by:

$$E_{TX}(k,d) = E_{TX} - elec(k) + E_{TX} - amp(k,d)$$
 (2)

$$E_{TX} - elec(k) = k \times E_{elec} \tag{3}$$

$$E_{TX} - amp(k, d) = \begin{cases} k \, \varepsilon_{fS} d^2, & \text{if } d < d_0 \\ k \, \varepsilon_{mp} d^4, & \text{if } d \ge d_0 \end{cases}$$
 (4)

where E_{elec} represents the energy expended by RF circuit in joules/bit for operating the RX or the TX circuits of the model. ε_{fs} and ε_{mp} represent the free-space and multiple-path amplification models. d_0 represents the threshold distance by which a node toggles between the free-space and multiple-path models. d_0 is computed using the formula $d_0 = \sqrt{\varepsilon_{fs}/\varepsilon_{mp}}$ [7]. On receiving a k-bit packet, a node will expend:

$$E_{RX}(k) = E_{RX} - elec(k) = k \times E_{elec}$$
 (5)

Local computation of *s* signals in a CH with k-bit length will consume:

$$E_{DA-tot} = s \times k \times E_{DA} \tag{6}$$

where E_{DA} represents the energy dissipated by aggregating one bit per signal.

IV. Performance Evaluation

In this section, the performance measure metrics will be explained, and then network settings and simulation results are analyzed.

IV.1. Performance Metrics

In this section, the metrics used to evaluate the performance of HE-WSN with different node distributions are defined. These metrics are also used in [8]:

 Stability and Instability Periods: Stability period or region represents the time interval until the death of the first node, while the instability period (unstable region) represents the time interval from the death of the first node to the death of the last node;

- Network lifetime: represents the time interval from the start operation of the WSN to the death of the last node;
- Network throughput: represents the total number of data packets reached the BS from the network CHs.

IV.2. Simulation Settings

Clustered HE-WSN is simulated in a region with dimensions $100~\text{m}\times100~\text{m}$. Nodes are distributed according to three distributions, uniform, normal, and exponential.

The total number of nodes is 100. Nodes come into two flavors, normal and advanced. MLE techniques are used to compute the defining parameters of the normal and exponential distributions by utilizing the locations information of the uniformly distributed network nodes as shown above. MATLAB software is used to program the SEP protocol with the corresponding node distributions and network settings. Table II shows the parameter settings used in the simulation.

IV.3. Simulation Results

Fig. 2 shows the number of alive nodes in LEACH based scenario for two cases.

The first case is the plain case in which m=0 and $\alpha=0$, the second one is when m=0.2 and $\alpha=3$. It is known that LEACH protocol is used in HO-WSN and it is heterogeneous-oblivious protocol. In the first case, node distributions have no great effect on the stability region since the time it has taken for the First Node to Die (FND) is almost the same.

In the second case, LEACH takes advantage of the presence of advanced nodes as the FND for all the node distributions increased significantly (longer stable region). The Network Lifetime (NLT) is also increased as the round of the Last Node to Die (LND) is also increased. Fig. 3 shows a comparison of SEP protocol for different node distributions. The simulation is done for two scenarios.

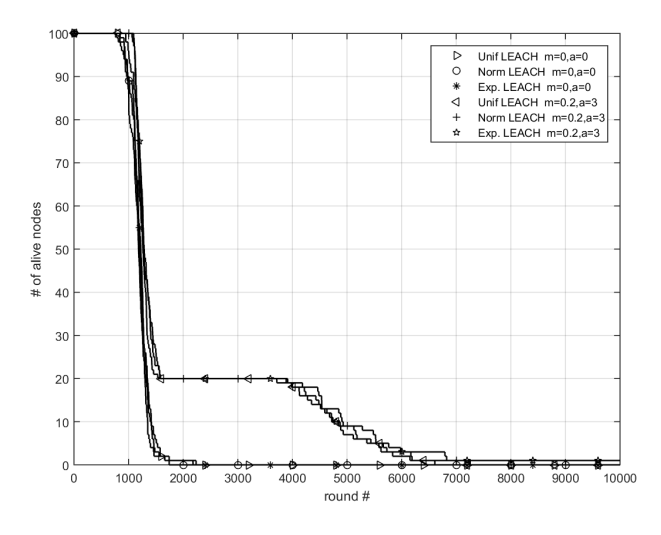


Fig. 2. No. of alive nodes using LEACH protocol

TABLE II
NETWORK PARAMETERS SETTINGS

Parameter	Value
Node energy	0.5 J
E_{elec}	50 nJ/bit
EDA	5 pJ/bit
\mathcal{E}_{fs}	10 pJ/bit/m ²
$arepsilon_{mp}$	0.0013 pJ/bit/m ⁴
\vec{k}	4000 bits
Number of nodes (N)	100
% of cluster heads (P)	0.1
Rounds	8 k and 10 k

In the first scenario, the heterogeneity factors are m=0.2 and $\alpha=1$. In the second scenario, heterogeneity factors are m=0.2 and $\alpha=3$. It is noticed that the node distributions have small effect in extending the stability region of the HE-WSN. Uniform node distribution has the longest stable region compared to the other distributions. In the second scenario, more energy is pumped into the advanced nodes, and as a result, the stability region has increased for all the node distributions with advantage of the uniform node distribution. Figs. 4 compare the performance of SEP to LEACH with the same heterogeneity factors m and α and LEACH where the extra energy of the advanced nodes is distributed uniformly over all WSN nodes; in this case it is referred to as FAIR protocol. In all the cases of different node distributions, SEP take full advantage of the extra advanced nodes energies. The stable region in uniform and normal cases has increased by 25% and the exponential case by 30% compared to the LEACH with the same heterogeneity factors. The unstable region in SEP is shorter compared to the LEACH for all the node distributions. Figs. 5 show the network throughput received by the BS over the course of the network lifetime. It can be seen clearly that the SEP protocol throughput is significantly larger than LEACH in all the cases of different node distributions as shown in subfigures 5(a)-(c). This is because SEP will guarantee more CHs in more rounds compared to the LEACH protocol.

This implies more data reports will be send to the BS. In subfigure 5(d), the network throughput for different node distribution using SEP protocol is shown.

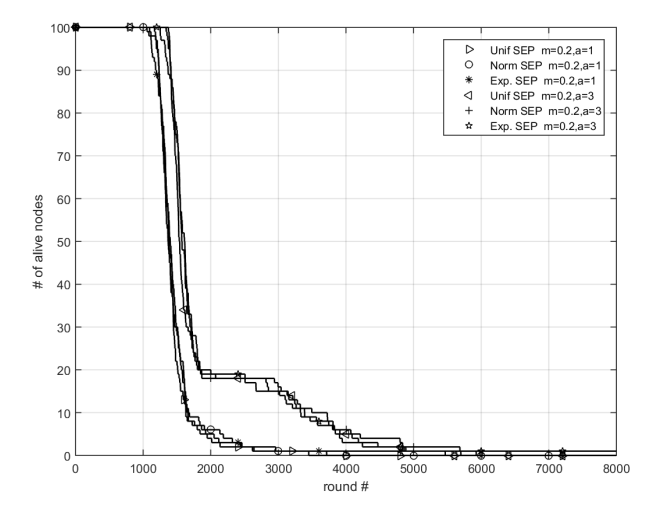
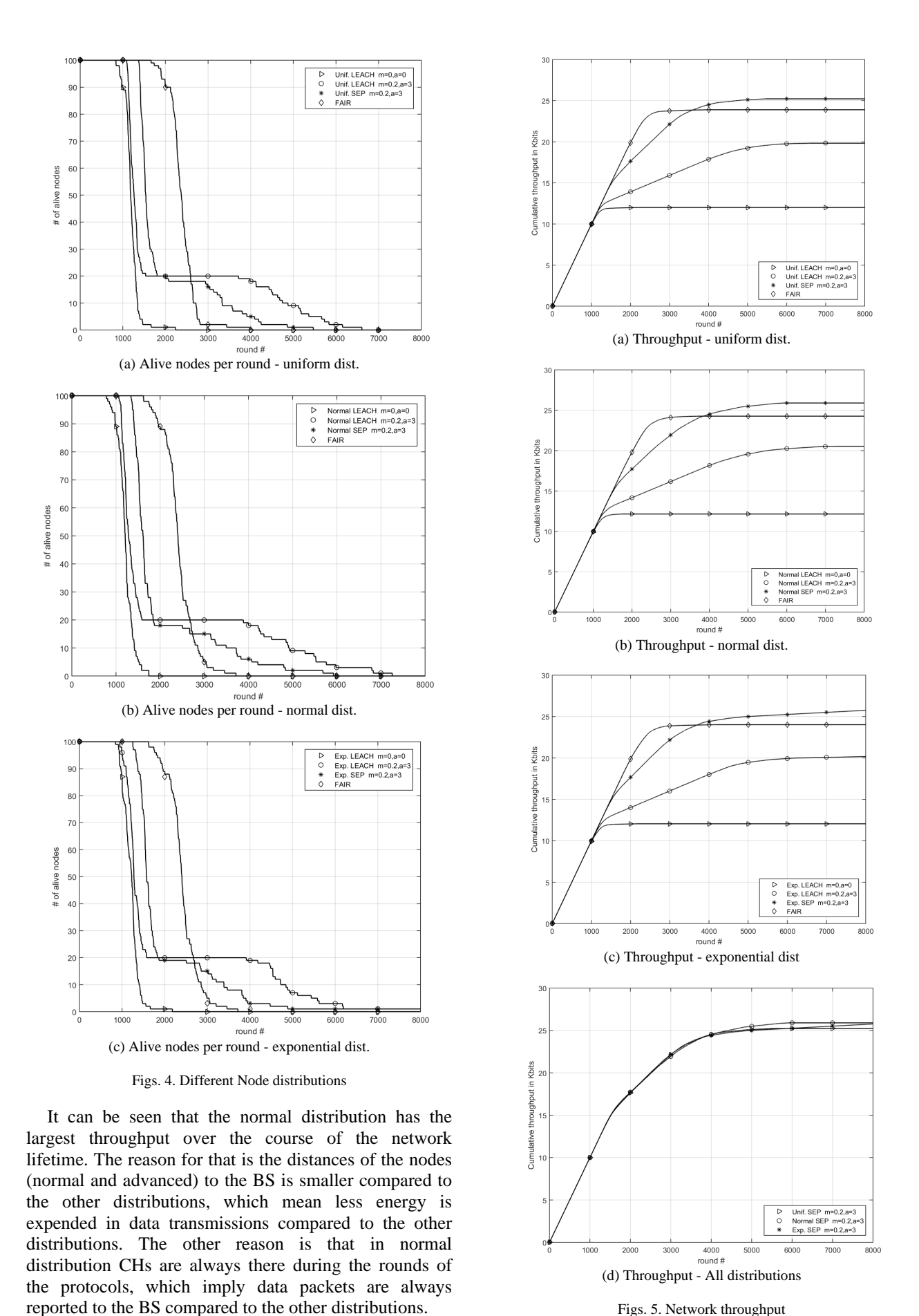


Fig. 3. No. of alive nodes using SEP protocol

Copyright © 2020 Praise Worthy Prize S.r.l. - All rights reserved



Figs. 5. Network throughput

Copyright © 2020 Praise Worthy Prize S.r.l. - All rights reserved

V. Conclusion

In this paper, the impact of different node distributions on the lifetime of heterogeneous WSN is studied. Three different node distributions are used: uniform, normal and exponential. The parameters of the normal and exponential distributions are computed using the maximum likelihood estimation principle. SEP and LEACH protocols are utilized in this study. SEP protocol is used in HE-WSN while LEACH protocol is used mainly in HO-WSN. Stability and instability periods along with the network lifetime are utilized as metrics for evaluating the performance of SEP and LEACH in HE-WSN. It has been noticed that node distributions have small effect on the stability regions of heterogeneousaware (SEP) protocol and heterogeneous-oblivious (LEACH) protocol. In all the different node distributions, SEP protocol outperforms LEACH with the same heterogeneity factors in terms of stability and unstable regions. In throughput analysis, normal distribution shows slightly greater number of data reports compared to the uniform and exponential distributions. In future study, the impact of different node distributions on threedimensional network settings will be investigated a long with the optimal BS location for minimum energy consumption and maximum network lifetime.

Acknowledgements

This research is funded by a research project at Al-Zaytoonah University of Jordan titled "Miniature Distributed Architecture for Massive Data Processing".

References

- [1] H. Barani, Y. Jaradat, H. Huang, Z. Li, and S. Misra. Effect of sink location and redundancy on multi-sink wireless sensor networks: a capacity and delay analysis. *IET Communications* 12, no. 8 (2018):941-947.
- [2] Y. Wang, P. Shi, K. Li, and Z. Chen. An energy efficient medium access control protocol for target tracking based on dynamic convey tree collaboration in wireless sensor networks. *International Journal of Communication Systems* 25, no. 9 (2012): 1139-1159.
- [3] I. F. Akyildiz, W. Su, Y. Sankarasubramaniam, and E. Cayirci. A survey on sensor networks. *IEEE communications magazine* 40, no. 8 (2002): 102-114.
- [4] D. Bhattacharyya, T. Kim, and S. Pal. A comparative study of wireless sensor networks and their routing protocols. *Sensors* 10, no. 12 (2010): 10506-10523.
- [5] M. Masoud, Y. Jaradat, D. Zaidan, and I. Jannoud. To Cluster or Not to Cluster: A Hybrid Clustering Protocol for WSN. In 2019 IEEE Jordan International Joint Conference on Electrical Engineering and Information Technology (JEEIT), pp. 678-682. IEEE, 2019.
- [6] Singh, Sunil Kumar, Prabhat Kumar, and Jyoti Prakash Singh. A survey on successors of LEACH protocol. *IEEE Access* 5 (2017): 4298-4328.
- [7] W. R. Heinzelman, A. Chandrakasan, and H. Balakrishnan. Energy efficient communication protocol for wireless microsensor networks. In System sciences, 2000. Proceedings of the 33rd annual Hawaii international conference, pp. 10-pp. IEEE, 2000.
- [8] G. Smaragdakis, I. Matta, and A. Bestavros. SEP: A stable election protocol for clustered heterogeneous wireless sensor networks. Boston University Computer Science Department,

- 2004.
- [9] Y. Jaradat, M. Masoud, I. Jannoud, T. Abu-Sharar, and A. Zerek. Performance Analysis of Homogeneous LEACH Protocol in Realistic Noisy WSN. In 2019 19th International Conference on Sciences and Techniques of Automatic Control and Computer Engineering (STA), pp. 590-594. IEEE, 2019.
- [10] Y. Jaradat, M. Masoud, and I. Jannoud. A Mathematical Framework of Optimal Number of Clusters in 3D Noise-prone WSN Environment. *IEEE Sensors Journal* (2018).
- [11] H. Barani, Y. Jaradat, H. Huang, Z. Li, and S. Misra. The effect of popularity rule on capacity and delay in multi-sink WSNs. In 2017 IEEE Wireless Communications and Networking Conference (WCNC), pp. 1-6. IEEE, 2017.
- [12] Y. Chen, C. Chuah, and Q. Zhao, Sensor placement for maximizing lifetime per unit cost in wireless sensor networks, *IEEE Military Communications Conference*, MILCOM 2005, October 2005, pp. 1097-1102.
- [13] G. Deepak and B. Beferull-Lozano, Power-efficient Sensor Placement and Transmission Structure for Data Gathering under Distortion Constraints, ACM Transactions on Sensor Networks (TOSN), Vol. 2, Issue 2, May 2006, pp. 155 – 181.
- [14] S. H. Al-Sharaeh, et.al, Multi-Dimensional Poisson Distribution Heuristic for Maximum Lifetime Routing in Wireless Sensor Network, World Applied Sciences Journal 5 (2): 119-131, 2008 ISSN 1818-4952.
- [15] W. F. Yun Wang and D. P. Agrawal, Gaussian versus Uniform Distribution for Intrusion Detection in Wireless Sensor Networks, *IEEE Transactions on Parallel And Distributed Systems*, Vol. 24, No. 2, February 2013.
- [16] A. E. Omar Said, Optimizing Sensors Distribution for Enhancing WSN Intrusion Detection Probability in Euclidian's Space, International Journal of Computer Applications (0975 – 8887) Volume 105 – No. 15, November 2014.
- [17] F. M. Osman and S. H. Al-Sharaeh, Hetrogeneous Multi-Deployment Strategy Effect on Maximizing the Lifetime Routing in Wireless Sensor Network, *Middle-East Journal of Scientific Research* 13 (6): 749-759, 2013 ISSN 1990-9233
- [18] Narmadha, C., Marichamy, P., Narayanan, A., An Energy Efficient Clustering Algorithm Using Harmony Memory Search for Wireless Sensor Network, (2018) *International Review on Modelling and Simulations (IREMOS)*, 11 (5), pp. 325-332. doi: https://doi.org/10.15866/iremos.v11i5.13584
- [19] Bani Yassein, M., Khamayseh, Y., Hmeidi, I., Al-Dubai, A., Al-Maolegi, M., A New Energy-Efficient Hybrid and Clustering Routing for Wireless Sensor Networks, (2017) *International Journal on Communications Antenna and Propagation (IRECAP)*, 7 (3), pp. 176-187. doi: https://doi.org/10.15866/irecap.v7i3.11484
- [20] Y. Jaradat, M. Masoud, I. Jannoud, and D. Zaidan. The Impact of Nodes Distribution on Energy Consumption in WSN. In 2019 IEEE Jordan International Joint Conference on Electrical Engineering and Information Technology (JEEIT), pp. 590-595. IEEE, 2019.
- [21] Mesleh, A., Battery Power Clustering Using Ant Colony Optimization, (2018) International Journal on Communications Antenna and Propagation (IRECAP), 8 (1), pp. 62-70. doi: https://doi.org/10.15866/irecap.v8i1.13838
- [22] Ezzedine, T., Miladi, M., Bouallegue, R., A Performance Comparison of Energy Efficient MAC Protocols for Wireless Sensor Networks, (2018) *International Journal on Engineering Applications (IREA)*, 6 (1), pp. 9-20. doi: https://doi.org/10.15866/irea.v6i1.15141
- [23] Vahabi, M., Ghazvini, M., Rasid, M., Abdullah, R., Traffic Aware Data Collection MAC Protocol for Wireless Sensor Networks, (2018) *International Journal on Engineering Applications (IREA)*, 6 (1), pp. 21-28. doi: https://doi.org/10.15866/irea.v6i1.15142

Authors' information

Electrical Engineering/Communications and Computer, Faculty of Engineering and Technology, Al-Zaytoonah University of Jordan, P.O.Box 130 Amman 11733 Jordan.



Yousef M. Jaradat is an associate professor in computer and communications engineering at Al-Zaytoonah University of Jordan. He received his B.S. in electrical and computer engineering from Jordan University of Science and Technology, Jordan, in 2000, and his Ph.D. in electrical and computer engineering from New Mexico State University, Las Cruces, New Mexico, USA, in

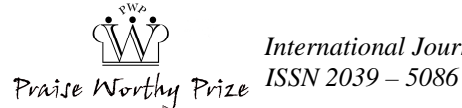
2012. His research includes work in the capacity of wireless networks, Obstacles analysis in network areas, and simulation of wireless networks.

E-mail: <u>v.jaradat@zuj.edu.jo</u>



Mohammad Z. Masoud is an associate professor in computer and communications engineering at Al-Zaytoonah University of Jordan. His research includes work in the design and measurement of computer network and their applications, P2P networks, routing protocols and ad hoc networks.

Dema Zeidan is a LAB engineer at the department of electrical engineering at Al-Zaytoonah University of Jordan. She has a master degree in computer engineering from the University of Jordan. Here research interests are: computer networks, artificial intelligence, embedded systems and electronics.



A Comparative Study of Wireless Sensor Network Using Cooperative Protocol

Raed S. M. Daraghma

Abstract – In this paper, a novel dispensed energy-efficient clustering strategy for heterogeneous wireless sensor network with fresh cooperative protocol is suggested and assessed. The clusterheads are chosen by a likelihood issued from the ratio between cooperative energy picks and both Channel State Knowledge (CSK) and Residual Energy Knowledge (REK) consideration of node and the average energy of the network. Matching energy dissipation of Bluetooth low energy, ZigBee and ANT protocols are supplied, in which a particular scope low power wireless sensor node periodically transmits a data packet to base station. Various tests are carried out to test the performance of the CC 2520, CC 2540 and CC 2570 modules. The average network lifetime, the throughput and the packet size calculations are described. It is supposed that the differentiation offered in this paper would interest implementation engineers in choosing a proper protocol. Copyright © 2020 Praise Worthy Prize S.r.l. - All rights reserved.

Keywords: Wireless Sensor Network, ZigBee, ANT, Energy Efficient Clustering

I. Introduction

Sensor networks consist of hundreds to thousands sensing nodes. It is eligible to produce these nodes as inexpensive and energy-efficient as conceivable and base on their massive figures to get raise form outcomes.

Network protocols should be prepared to attain error allowance in the existence of single node disability while decreasing energy dissipation of the network. Since the fixed wireless channel bandwidth should be participated through all the sensors in the network, routing protocols should be fit to make domestic cooperation in order to decrease bandwidth demands. The noticed data in the network should be sent to the monitor fusion, where the termination employee can reach the data. There are numerous probable patterns for sensor networks.

Wireless sensor networks are utilized for a diversity of functions like detection, localization and routing targets of intension [1]-[21]. A precise estimate of the source position can be gained by employing the energy information's of the sensors [1]. Clustering [2], [3] is one of the succeeded methods applied for improving the lifetime of WSN where the target zone is sectioned into sub areas, called clusters. Every cluster has a Cluster Head (CH), which is in charge of data gathering from sensor nodes within its cluster and transmission to the BS charge of data gathering from sensor nodes within its cluster and transmission to the BS. In [4], a new protocol that aims to enhance the network lifetime by reducing the per node energy consumption and to maintain balance between energy consumption and energy disparity is proposed. In [5], the challenges and the limitations of WSNs in the agriculture domain are explored and several power reduction and agricultural management techniques for long term monitoring are highlighted. These approaches may also increase the number of opportunities for processing Internet of Things (IOT) data. The choice of CHs and CH to subscriber ratio is significant, when to spin the current CH and by whom is another interest. LEACH Protocol, a clustering formed protocol that reduces energy wasting in sensor networks, has been progressed [6], [7]. LEACH exceeds traditional clustering algorithms by employing fit clusters and revolving cluster heads, allowing the energy demands of the device to be dispensed through all the sensors.

Almost of the systematic conclusions for LEACHtype, platforms are gained, supposing that the nodes in the network are provided with the identical amount of energy as in the case of homogenous sensor networks. Since the lifetime of sensor networks is ended, there is a requirement to stimulate the sensor network by inserting more nodes. They will be supplied with more energy than the nodes that are formerly employed, causing heterogeneity in the network in terms of node energy. In [8], a multi hop protocol for WPANs, a cost function computed relying on residual energy of sensor nodes and their location from BS has been designed. In [9], proposed a modified energy efficient protocol has been proposed. It joins the scheme of clustering and multi hop communication. In [10], novel clustering protocol called EE heterogeneous LEACH protocol has been presented.

The aim of this paper is to foster the CH chosen scheme. CH is chosen in each cluster based on the best channel and residual energy. In [11], a novel clustering established b protocol for heterogeneous WSNs has been presented. The proposed protocol upgrades energy efficiency of the network and expands the network lifetime. In [12], two energy-efficient techniques that

focus on the data transmission between CHs and the BS and the energy consumed during this operation have been proposed. In the first proposed technique, the CHs deliver data to the BS indirectly via one regular sensor, namely anchor. On the other hand, CHs in the second technique send data to the BS via multiple regular sensors. By virtue of the proposed mechanism, a new data transmission approach between different objects, including anchors, CHs and BSs that affect the energy efficiency is investigated. Intensive simulation experiments show that the proposed mechanisms are more energy-efficient. In [13], a novel approach for health monitoring system has been proposed. The new approach depends on a smart health network, where patients are classified into a set of clusters, based on their health status. This approach helps managing communications between patients' sensors and the monitoring center, and reduce power consumption by allowing patients with critical health status to transmit continually their health parameters, and allowing patients with less critical and noncritical health status to transmit continually their health parameters. For the experiments, OualNet V5.2 simulator has been used, using standard health parameters. Simulations results show that the proposed approach outperforms the non-classified based health monitoring system in terms of reducing energy consumption in transmit mode by 30% and in receive mode by 30%. In addition, simulation results show an improvement of average Jitter by 13%, and an average end-to-end delay by 9.6%. In [14], a new time-divisionmultiple-access model is proposed in order to timeslot efficiently the operation of the sensor nodes and the dedicated radio frequency sources to overcome the interference problems, and in order to improve the energy efficiency of the network system. Based on the proposed time-division-multiple-access model, an algorithm is developed for fair allocation of energy harvesting and information transmission timing. This work is validated through numerical comparison. The simulation results reveal that the proposed wireless information and the power transfer system outperform an existing state-ofthe-art wireless information and power transfer system, regardless of the distance of the sensor nodes to the dedicated radio frequency sources and the sink node. In [15], various range-based localization techniques used in wireless sensor networks are reviewed. It presents a mathematical model for determining sensor locations Received Signal Strength Indicator on measurements and it studies the energy consumption of the proposed localization technique. The localization technique under consideration uses Trilateration in order to find initial estimates of the coordinates of the sensor nodes. It then it applies Recursive Least Square Estimation in order to refine the estimates and account for the noise accompanying the RSSI measurements.

The paper is coordinated as follows. In Section II, the comparative study is depicted. In Section III, the hardware and simulation is presented. In Section IV, the proposed protocol is explained. Simulation results are

presented in Section V. This paper is ended with concluding comments in Section VI.

II. Comparative Study

II.1. ZigBee Technology

ZigBee is a criterion- established technology for observation and remoting. It has been formed to back up low data rate, low power dissipation, more powerful, less costly, more effective, guarantee, and has lower delayed, energy competence with efficient wireless lattice platform. ZigBee 802.15 can be applied in any controlling and observing implementation that needs a wireless lattice. ZigBee supplies self-controlled, multihop, and credible mesh networking with extended battery lifetime [16]. It employs the cancellation impact technique in CSMACA and pre-sets a prior specific time slot for a constant bandwidth communications duty in order to evade concurrence and interference when sending data. MAC layer arranges a fully assured data transmit technique, and each packet transmitted by the receiver must stay for affirmation. ZigBee link technology is shown in Figure 1. The CC2520 is TI's second descent ZigBee/IEEE 802.15.4 Radio Frequency transceiver for the 2.4-GHz unaccredited ISM series. This plate allows manufacturing category implementations by presenting state-of-the-art noise impunity, wonderful link budget, procedure up to 125and low-voltage procedure.

Besides, the CC2520 supplies comprehensive equipment backup for packet treatment, data storing, burst sending, data encryption, data authentication, pure channel assessment, connection fineness significance as shown in Figure 2.



Light Network

Fig. 1. ZigBee light link technology

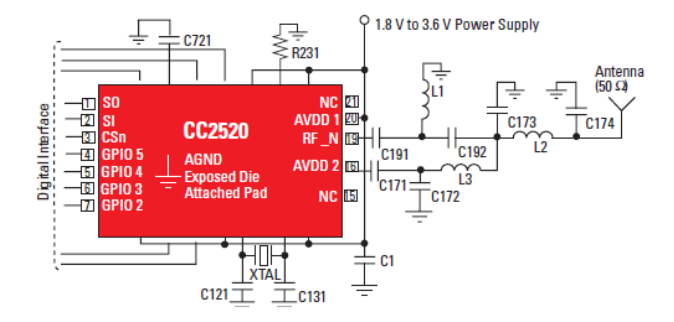


Fig. 2. CC 2520 application circuit

Copyright © 2020 Praise Worthy Prize S.r.l. - All rights reserved

II.2. Bluetooth Technology

The CC2540 is an expense-efficient, low power, real framework -On-Chip settlement for single form. The CC2540 joins a 1-Mbps Gaussian Frequency Shift Frequency (GFSK) radio frequency transceiver, showing excellent domain through the contest with a marginal rich 8051 MCU core. This extremely incorporated and low-cost, connected with TI's Bluetooth low energy stack, shows real one-chip incorporated resolution as shown in Figure 3.

II.3. ANT Technology

ANT supplies an easy, low- expense and very-low resolution for short-distance wireless communication in peer-to-peer, and more sophisticated network topologies. It is proposed to work utilizing lowcost, low power microcontrollers, and transceivers working in the 2.4 GHz ISM series. The ANT WSN protocol has been planned for accessibility and capacity, effecting in very-low power dissipation, maximized battery life. ANT is a perfect technique for workable networks because of this ingrained potential to boost ad hoc correlation of thousands of nodes [18]. ANT allows a system to spend utmost of its time in a very-low power sleep process, wake up rapidly, send for the lowest likely time, and soon come back to a very-low power sleep process. The CC2570 is ANT Radio Frequency network processors that perform the simple to employ, energyfunctional ANT protocol. The CC2570 can be linked to a host MCU over a UART or SPI sequent connect and arrives through a set of API requisitions. The plurality of the ANT protocol is constructed into the CC2570, containing the ANT-FS file system operation as shown in Figure 4.

III. System Model

In this research, the wireless energy consumption type is specified in Figure 5. In order to send m-bit message to a distance *x*:

$$E_{Tx}(m,x) = \begin{cases} mE_{elec} + m\varepsilon_{fs}x^2, & x < x_0 \\ mE_{elec} + m\varepsilon_{mp}d^4, & x \ge x_0 \end{cases}$$
(1)

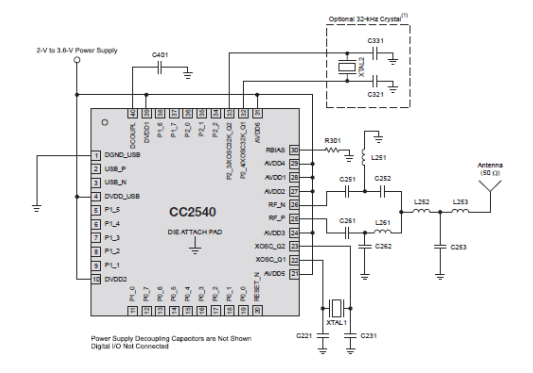


Fig. 3. CC 2540 application circuit

35 34 33 00000 0 CND GND 29 AVDD4 2 28 AVDD1 GND 27 AVDD2 TxD/SOUT 26 RF N CC257X RxD/SIN 25 RF_P BR2/SCLK 24 AVDD3 BR1/SFLOW 23 XOSC_Q2 8 BR3/FAST SPI 9 22 XOSC 01 DVDD2 40 21 AVDD5

Fig. 4. CC 2570 application circuit

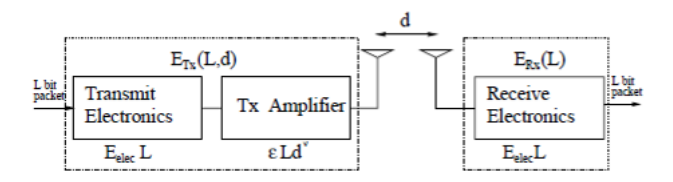


Fig. 5. Wireless Energy consumption type

By using the Table I, the transmitting energy and the energy required for the amplifier circuit can be found respectively, as shown in equations (2) and (3):

$$E_{Tr} = \frac{P_t}{R_b} \tag{2}$$

$$\varepsilon_{mp} = \frac{P_r}{R_b G_t G_r h_t^2 h_r^2} \tag{3}$$

where P_r represents the receiver sensitivity, G_t clarifies the transmitter gain, G_r illustrates receiver gain, λ states the carrier wavelength, h_b , h_r represent transmitter and receiver antennas height respectively.

IV. Proposed Protocol

LEACH is a repeated algorithm and every reduplicate in the algorithm is named as 'round'. In LEACH, during the formed period, every sensor node produces an arbitrary figure between 0 and 1. If this arbitrary figure is lower than a fixed amount, the threshold rate T(s), then the sensor node turns into a CH for that round. The threshold rate is selected as:

$$T(s) = \begin{cases} \frac{p_{opt}}{1 - p_{opt}} \left(r \operatorname{mod} \left(\frac{1}{p_{opt}} \right) \right), & \text{if } s \in G \\ 0, & \text{otherwise} \end{cases}$$
 (4)

Copyright © 2020 Praise Worthy Prize S.r.l. - All rights reserved

 $\begin{tabular}{l} TABLE\ I \\ Comparison\ Of\ The\ ANT,\ Bluetooth\ And\ ZigBee \\ \end{tabular}$

COMPARIS	ON OF THE AIN.	I, BLUETOUTH ANI	ZIGDEE
Transceiver	ANT	Bluetooth	ZigBee
Chipset	CC 2520	CC 2540	CC 2570
Rx sensitivity	-85.8 dBm	-93 dBm	-98 dBm
TX Power	4 dBm	4 dBm	4 dBm
BR	250 kb/s	250 kb/s	250 kb/s
Size of the packet	4000 bit	4000 bit	4000 bit
Area of simulation	100×100	100×100	100×100
Initial energy of node	0.05 J	0.05 J	0.05 J
ETX-Amp	$0.01 \times 10^{-6} \text{ J/b}$	$0.01 \times 10^{-6} \text{ J/b}$	$0.01 \times 10^{-6} \text{ J/b}$
ε multi-path	2.17×10^{-15} J/b/m ⁴	3.95×10 ⁻¹⁶ J/b/m ⁴	$1.25 \times 10^{-16} \text{ J/b/m}^4$
Range (meters)	1-100 m	1-10 m	1-100 m
Frequency band	2.4 GHz	2.4 GHz	2.4 GHz
IEEE Specification	802.15.4	802.15.1	802.15.4
E_{DA}	5 nJ	5 nJ	5 nJ
N_0	-40 dBm	-40 dBm	-40 dBm
BER	10^{-3}	10^{-3}	10 ⁻³
η	1	1	1
α	2	2	2
$P_{ m max}$	0.2	0.2	0.2
Number of node	100	100	100
Type of modulation	BPSK	BPSK	BPSK
E_c	2×10^{-4}	2×10 ⁻⁴	2×10^{-4}
E_{cs}	2×10^{-4}	2×10^{-4}	2×10^{-4}
E_{es}	10^{-4}	10^{-4}	10-4

In this work, a new threshold rate is developed, as shown below:

$$T(s) = \begin{cases} \frac{p_i}{1 - p_i} \left(r \operatorname{mod}\left(\frac{1}{p_i}\right) \right), & \text{if } s \in G \\ 0, & \text{otherwise} \end{cases}$$
 (5)

$$p_i = \frac{p_{opt} E_{cop}}{E_{av}} \tag{6}$$

where formula (6) is the probability of cooperative nodes, E_{cop} is the cooperative energy and will be calculated as shown in equation (9), and E^{av} represents the average energy of network. The source and the relay are chosen as below:

- BS initially, transmit demand to transmit (DTT) packet, if the clear to transmit (CTT) packet is truly received by BS and if assistant prepared to transmit (ATT) packet is collected then BS will get in the cooperative phase, and receives packets transmitted from source and relay sensor nodes without errors. Else, it will receive a data packet from the source node in non-cooperative process. It is supposed that the transmission power of control packets such as DTT, ATT and CTT is specified;
- All the sensor nodes in the network monitor for DTT, CTT and ATT transmit by BS, when the sensor node receives the DTT packet, it will assess the variance of the channel;
- 3. After relay node has picked the channel variance between source and the relay, then the transmission P_1 and P_2 can be computed according to expression

- (8). Then ATT packet attached with the value P_1 will be released
- 4. Source node will be awaiting the ATT packet after sending the CTT packet. If it receives the ATT packet, then the cooperative connection of source and relay node is formed. Otherwise, the source node will send the data to the BS.

The power P_2 can be given in term of P_1 as:

$$P_{2} = f(P_{1}) = \frac{BN_{0}^{2}\sigma^{2}_{sr}P_{1}}{\left(\zeta b^{2}P_{1}^{2}\sigma^{2}_{sd}\sigma^{2}_{sr}\sigma^{2}_{rd}\log_{2}M + -A^{2}N_{0}^{2}\sigma^{2}_{rd}\right)}$$
(7)

$$P_2 = \frac{p_1}{cp_1^2 - D}$$

$$E_{coon} = E_{coin1} \times E_{coin2} \tag{8}$$

where:

$$E_{coin1} = E_{co1} - P_1 \times D_{op} - E_{es} - E_{cs} - E_c$$

$$D_{op} = packet \ size \ / \ R_b$$

and:

$$E_{coin2} = E_{co2} - P_2 \times D_{op} - E_{es} - E_{cs} - E_c \label{eq:ecoin2}$$

where E_{co1} , E_{co2} are the most two energies in each cluster gathers both CSK and REK into consideration to extend the network lifetime while encountering the average BER demand, D_{op} is the time of the power data, R_b is the data rate.

V. Simulation Results

The behavior of the submitted protocol is assessed using MATLAB for heterogeneous networks. In the system, 100 sensor nodes are arbitrarily placed in a 100 m×100m area where the base station is suited at the middle. The submitted algorithm is matched with ZigBee, Bluetooth, and ANT protocols related to dead and alive sensor nodes per round, energy dissipation of the network, and thorough throughput. The whole figure of rounds utilized in the study is 2000. Network type variables are outlined in Table I, where E_c represents the transmitting energy for information packet, E_{cs} illustrates the energy dissipation of a control packet, E_{es} illustrates the receiving and computing energy dissipation of the information packet. Here, the whole sensor nodes have several amounts of initial energies. The initial energies are orderly dispensed on [0.5, 1]. Various workouts are assumed, the rate stability periods are studied, and the outcomes are exhibited in Figures 6, 7 and 8.

Copyright © 2020 Praise Worthy Prize S.r.l. - All rights reserved

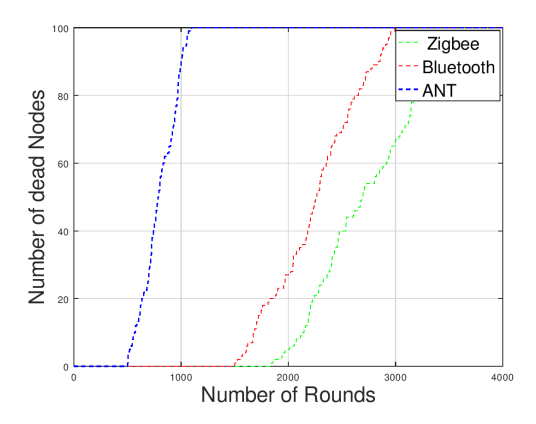


Fig. 6. Number of dead nodes per round

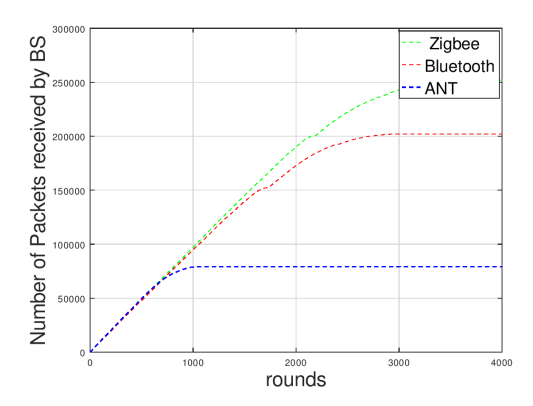


Fig. 7. Throughput

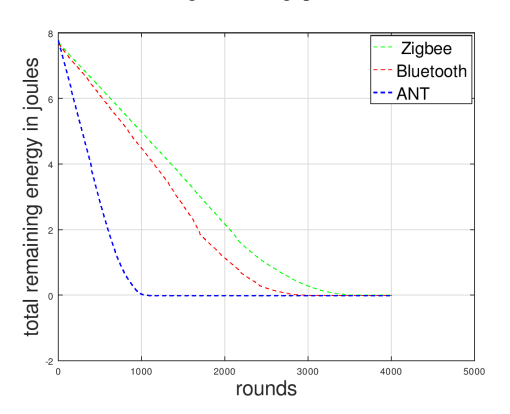


Fig. 8. Energy Consumption

Figure 6 represents the average figure of dead sensor nodes per round, showing stability time of the network. The death of the first sensor node happens at the round 503 in ANT whereas the death of the first sensor node happens at round 1500 and 1829 in Bluetooth and ZigBee, respectively. The death of the last sensor node happens at round 1100 in ANT protocol whereas the death of the last node occurs at round 2993 and 3598 in Bluetooth and ZigBee, respectively. Hence, the stability and the network lifetime for ZigBee protocol perform better when matched to other protocols. Figure 7 displays the successful packet received by base station. ZigBee protocol attains higher throughput than Bluetooth and ANT protocols. The total packet received by base station has been 79255 in ANT whereas the total packets

received by the base station have been 202058 and 252057 in Bluetooth and ZigBee, respectively. Therefore, ZigBee protocol has a better throughput than other protocols. Figure 8 shows the total remaining energy over time. The whole energy in the network is 7.5 J. The primary energy of the network is dissipated at the round 503 in the ANT protocol whereas the primary energy of the network is dissipated at round 1500 and 1829 for Bluetooth and ZigBee protocols respectively. In Figure 9, the packet size of the data with respect to the successful packet received to the base station (throughput) is simulated. As shown in this figure, the throughput does not attain less than about 200000 bit/s (new unit) for ZigBee protocol, not less than about 150000 bit/s for Bluetooth and not less than about 50000bit/s (new unit) for ANT protocol. Anywise, the throughput can be remarkably reduced when the number of packet size increases for each of the three protocols. In Figure 10, the packet size of the data with respect to the first dead nodes is simulated. As can be seen, the first dead node for the three protocols deceases when the number of packet size increases. However, the first dead node does not reach more than about 2000 round for ZigBee protocol, not more than about 1800 round for Bluetooth, and not more than about 600 round for ANT protocol. In Figure 11, the packet size of the data is simulated with respect to the last dead nodes; it can be seen that the last dead node for the three protocols deceases when the number of packet size increases. However, the first dead node does not reach more than about 3800 round for ZigBee protocol, not more than about 3400 round for Bluetooth and not more than about 1300 round for ANT protocol.

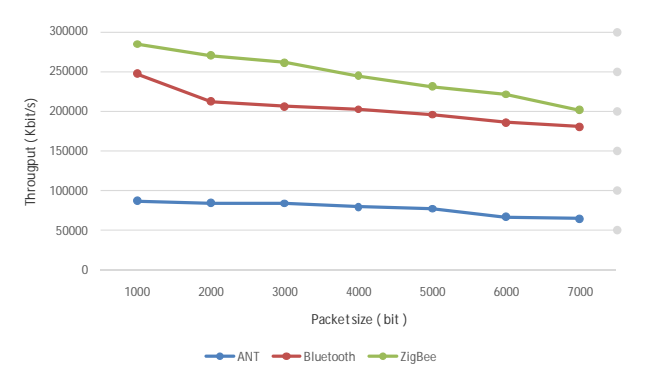


Fig. 9. Comparison of the Throughput versus the packet size

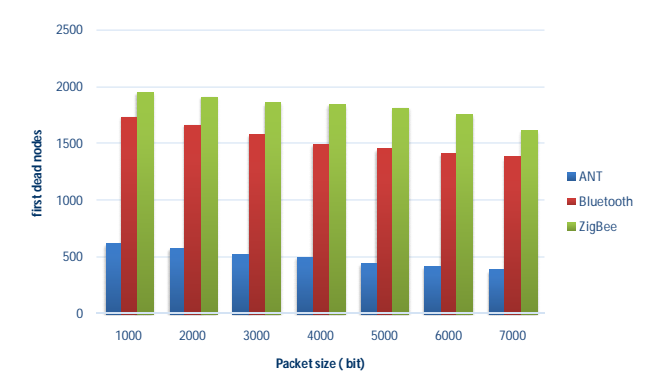


Fig. 10. Comparison of the first dead node versus the packet size $\,$

Copyright © 2020 Praise Worthy Prize S.r.l. - All rights reserved

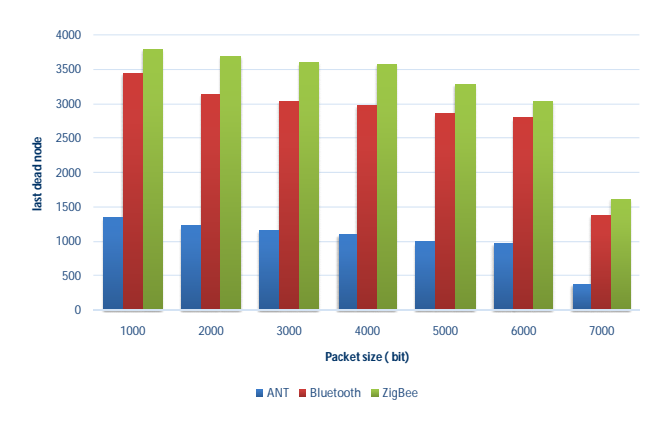


Fig. 11. Comparison of the last dead node versus the packet size

VI. Conclusion

In this paper, a novel cooperative algorithm is suggested to route data in WSNs. The major concentration has been to improve cluster head chosen method. In the submitted protocol, cluster heads are chosen in every cluster by a probability formed on the ratio between cooperative energy of sensor node and the average energy of the network. In this paper, the lifetime, the throughput, the energy consumption, the packet size, and the bit error rate for the ANT, ZigBee and Bluetooth protocols have been investigated. It has been discovered that ZigBee protocol has achieved the most prolong lifetime, throughput and lowest energy dissipation, coming after Bluetooth and ANT. The result shows that the throughput decreases with the increasing of the packets size and bit error rate. Furthermore, the ZigBee, ANT and Bluetooth protocols technologies have been also examined, jointly with the common overview of the technology that helps the users in considering the needed elements when selecting the technology while permitting the vendors and the manufacturer of different Protocols in wireless sensor network devices to formulate the needful refinements in the fields with shortages.

Acknowledgements

We would say to thank for that support our research. My university: Palestine Technical University Kadoorei.

References

- [1] Vinery Kumar, Sanjeev Jain and Sudarshan Tiwari, Energy Efficient Clustering Algorithm in Wireless Sensor Networks A survey, *IJCSI International Journal of Computer Science Issues*, Vol.8, Issue 5, No 2, September 2011.
- [2] Prabhat Kumar and M.P.Singh, A New Clustering Protocol Based on Energy Band for Wireless Sensor Network, *International Journal of Information Technology and Knowledge Management*, Volume 3, January –June 2010, ISSN: 0973-4414.
- [3] Donghoon Lee, Kaliappan, V.K; Duckwon Chung; Dugki Min, An energy efficient dynamic routing scheme for clustered sensor network using a ubiquitous robot Research, *Innovation and Vision* for the Future, 2008.RIVF 2008. IEEE International Conference, 2008, page(s): 198-203.
- [4] G. Kumar, S. Chinara, Development of Energy Efficient Wireless Sensor Networks Protocol for Precision Agriculture, *Journal of*

- Basic and Applied Engineering Research, Vol. 2, No. 5, pp. 360-36, 2015.
- [5] H. Jawad, R. Nordin, S. Gharghan, Energy-Efficient Wireless Sensor Networks for Precision Agriculture: A Review, *Sensors*, 2017.
- [6] W. B. Heinzelman, A. P. Chandrakasan and H. Balakrishnan, An application-specific protocol architecture for wireless microsensor networks, in *IEEE Transactions on Wireless Communications*, vol. 1, no. 4, pp. 660-670, Oct. 2002. doi: 10.1109/TWC.2002.804190
- [7] Panghal Amanjeet, Mittal Nitin, Singh D.P.& Chauhan R.S. (2010) Improved Leach communication protocol for WSN, National Conference on Computational Instrumentation CSIO Chandigarh, India, 177-181.
- [8] N. At, H. Senel, R. daraghma Multi hop Efficient Protocol for ZigeBee, Bluetooth Low energy and ANT Sensor Nodes, *Journal* of Computer, Vol. 13, No. 4, pp. 471-479 2018.
- [9] Raed S.M. Daraghma Maximizing the Lifetime of Multi hop Routing Protocol Using Gateway for Wireless Sesnor Network, *International Journal of Computer and Network Technology*, Vol. 5, No. 1, 2017.
- [10] Nuray. AT. Daraghma. SM, a New Energy Efficient Clusteringbased Protocol for Heterogenous Wireless Sensor Networks, J. Electr Electron Syst. Volume 4. Issue 2. 2015.
- [11] Nuray. AT. Daraghma. SM, Improved Cluster Head Selection For Energy Efficiency In Wirelesss Sensor Networks, *International Journal of Modern Enginnering Research (IJMER)*. Volume 6. Issue 5. pp. 2249-6645, 2016.
- [12] Bani Yassein, M., Khamayseh, Y., Hmeidi, I., Al-Dubai, A., Al-Maolegi, M., A New Energy-Efficient Hybrid and Clustering Routing for Wireless Sensor Networks, (2017) *International Journal on Communications Antenna and Propagation (IRECAP)*, 7 (3), pp. 176-187. doi: https://doi.org/10.15866/irecap.v7i3.11484
- [13] Bani Yassein, M., Hamdan, M., Shehadeh, H., Mrayan, L., A Novel Approach for Health Monitoring System Using Wireless Sensor Network, (2017) International Journal on Communications Antenna and Propagation (IRECAP), 7 (4), pp. 271-281. doi: https://doi.org/10.15866/irecap.v7i4.11311
- [14] Olatinwo, S., Joubert, T., Maximizing the Throughput and Fairness of a Water Quality Monitoring Wireless Sensor Network System, (2018) International Journal on Communications Antenna and Propagation (IRECAP), 8 (6), pp. 448-460. doi: https://doi.org/10.15866/irecap.v8i6.15031
- [15] Takruri, M., Ismail, S., Awad, M., Al-Hattab, M., Hamad, N., A Comparative Study of Energy Consumption Required for Localization in Wireless Sensor Networks, (2019) *International Journal on Communications Antenna and Propagation (IRECAP)*, 9 (4), pp. 301-310. doi: https://doi.org/10.15866/irecap.v9i4.17158
- [16] Aamir Shaikh and Siraj Pathan, Research on Wireless Sensor Network Technology, *International Journal of Information and Education Technology*, Vol. 2, No. 5, October 2012.
- [17] Omojokun G. A Survey of ZigBee Wireless Sensor Network Technology: Topology, Applications and Challenges, International Journal of Computer Applications, Vol. 130, No. 9, 2015.
- [18] Buratti C, Conti A, Dardari D, Verdone R. An overview on wireless sensor networks technology and evolution. Sensors (Basel). 2009;9(9):6869-6896. doi:10.3390/s90906869
- [19] Vahabi, M., Ghazvini, M., Rasid, M., Abdullah, R., Traffic Aware Data Collection MAC Protocol for Wireless Sensor Networks, (2018) *International Journal on Engineering Applications (IREA)*, 6 (1), pp. 21-28. doi: https://doi.org/10.15866/irea.v6i1.15142
- [20] Ezzedine, T., Miladi, M., Bouallegue, R., A Performance Comparison of Energy Efficient MAC Protocols for Wireless Sensor Networks, (2018) *International Journal on Engineering Applications (IREA)*, 6 (1), pp. 9-20. doi: https://doi.org/10.15866/irea.v6i1.15141
- [21] Narmadha, C., Marichamy, P., Narayanan, A., An Energy Efficient Clustering Algorithm Using Harmony Memory Search

Copyright © 2020 Praise Worthy Prize S.r.l. - All rights reserved

for Wireless Sensor Network, (2018) International Review on Modelling and Simulations (IREMOS), 11 (5), pp. 325-332.doi:https://doi.org/10.15866/iremos.v11i5.13584

Authors' information

Department of Electrical and Electronics Engineering, Palestine Technical University Kadoorie, Palestine.



Raed S. M. Daraghma was born in 1977 in Palestine, he received his master degree from Jordan science and technology in electrical and communication engineering, Jordan in 2010, he got his P.H.D degree from Anadolu University, turkey in 2016. He has published number of papers and journals. He has engaged in educational work many years manly teaches

digital communication, mobile, digital communication networks etc... at Palestine technical university PTUK. His mainly research areas include wireless sensor network, signal processing, MIMO radar and electromagnetic waves.

E-mail: R.daraghmeh@ptuk.edu.ps



Detecting the Online Shopping Factors Using the Arab Tweets on Media Technology

M. B. Yassein, O. Alomari

Abstract – With the popularization of the internet and media technology and the rapid adaption to the development of information technology, the online shopping has been accepted by millions of customers as a new model of shopping. It has been applied to different domains such as electronics, books and clothing marketing. Thus, it has led to the growth of hundreds of online shopping sites around the world and has created competitive electronic commerce. This paper analyzes the influencing factors on consumers of online shopping in the Arab world using Arabic tweets. Several classification algorithms have been used, such as support vector machine, naive Bayes, random forest, voting classifier and decision tree in Python and Weka. The results show that around 51% of users say that the online shopping is better than the traditional one based on the tweets in dataset. In addition, it has been found out that the random forest is the best algorithm in Python compared to other ones with an accuracy of 93.7% in 0.4 test size. Copyright © 2020 Praise Worthy Prize S.r.l. - All rights reserved.

Keywords: Machine Learning, Online Shopping, Data Mining Tools, Hold-Out Method, Influencing Factors, Media Technology

Nomenclature

MNB Multinomial Naïve Bayes
DT Decision Tree
SVM Support Vector Machine

RF Random forest VC Voting classifier

I. Introduction

The development of information technology, media technology and the internet network has provided internet users with a huge number of online services. One of them is the online shopping, which has become an important shopping model that has given the consumers the ability to shop smartly anytime and anywhere over the internet. The concept of e-shopping has spread widely among internet users around the world because it allows them to explore different alternatives and choose the best ones in shorter time and with fewer efforts than traditional shopping. It also provides the ability to compare products, prices, and trade-offs between stores [1], [2]. Among the top companies around the world, 95 percent of them has established their own websites, 30 percent of these companies perform online commercial activities over their websites [3]. M. H. Moshrefjavadi et al. in [4] have examined some factors that influence the online shopping behavior of consumers. The results have indicated that non-delivery risk and financial risk have a negative effect on consumers' behavior, so they have concluded that e-sellers should make their websites safer and they should assure consumers about product delivery. The number of social media users is increased and the size of the data is huge. Therefore, the data need some preprocessing techniques and many machine learning algorithms to extract useful information in order to use it in many tasks and fields. In this study, the collected data have included 7065 out of 9573 tweets from Arabic customers' reactions to online shopping from YouTube and Twitter. Then, the influencing factors on consumers of online shopping in the Arab world have been analyzed. Several classification algorithms, such as SVM, MNB, RF, VC and DT have been evaluated in Python and Weka with different test sizes (0.1, 0.2, 0.3, 0.4 and 0.5).

The remainder of this paper is organized as follows. In section II, the previous related works are discussed. Section III contains an overview of Arabic language structure. Section IV shows the proposed system. In section V, the experimental results are presented. Section VI provides a conclusion and future works that can be done.

II. Related Work

Ahmeda et al. in [3] have collected the dataset about products and customers from the most popular online shopping websites and then they have classified them using the most popular machine learning classifiers in order to provide a recommender system that gives a personalized recommendation to the customers. The decision table of eleven classifiers provides a high accuracy up to 87.13% and the low accuracy is 36.30%.

Therefore, this result can help the various online shops to build a perfect recommender system.

This helps customers to find their needs from the represented products on online shopping website using decision table of eleven classifiers. Kumar et al. in [5] have studied the factors that affect the online shopping behavior of consumers and they have found out that the non-delivery risk and financial risk negatively effect on the online shopping.

Therefore, the dealers should make their websites secure from a financial perspective and guarantee the delivery of their products to the customers.

Therefore, the attitude variables make a fundamental contribution in online shopping. This will make a positive effect on attitude toward online shopping. Jiang et al. in [6] have studied the factors affecting the consumers' buying behavior towards online shopping and the research result that provided stakeholders in managerial implications.

In addition, they have provided feedback and certain understandings to the stockholders to apply and improve different trade manners in order to raise customers' intention to shop online. The research has showed that creativity in a specific domain significantly effect on customers' buying intention.

Therefore, the dealers may develop new technologies or features that make their online stores attractive and easier to use which will impulse the customers to shop online. Lim et al. in [7] have studied the factors influencing online shopping behavior. The research results show that three out of five hypotheses are true.

The first one, the connection between the online shopping and purchase intention, has showed the strongest relationship and purchase intention for university students affected by perception friends, media, and families. Nisar et al. in [8] have studied the factors that determine e-satisfaction and consumer spending in e-commerce retailing. The results show that the customer satisfaction is a core factor in both online and offline shopping.

Therefore, the e-dealers always aim to improve eservices quality, provide wide products ranges, and frequently updating customer expectations to increase consumer spending. Monsuwé et al. in [9] have studied the factors that drive consumers to shop online. The results show that the attention to shop online and the attitude about online shopping are not affected only by usefulness, ease of use, and enjoyment but are also affected by external factors such as trust in online shopping, product advantage and previous experience in online shopping. Chang et al. in [10] have analyzed experimental research on online shopping. Based on this study, two reference models have been derived. It has been found out that many important variables have not been fully investigated. The effort has been put into a comprehension of the dynamics of the adoption of online shopping in order to develop online transactions, attract customers to buy online, and move to society more heavily involved in e-commerce.

III. Arabic Language Challenges

In this work, many challenges have been faced while using the Arabic language since it is like an encyclopedia of words.

- One word in Arabic may be changed if only one or two alphabets have been added to its stem, i.e. بنكسه,
- 2. Most of the users have repeated the letter more than once to put emphasis on the meaning of the word that expresses their feelings, such as that means being very tired;
- Negation words, which are used to give the opposite meaning of the verb such as نجب شرداً نـل, that means "I didn't study hard".

IV. Methodology

The proposed system works on Arabic reviews from YouTube and Twitter. This system divides the Arabic reviews into three categories: positive, negative and neutral. Preprocessing steps have been applied to the collected Arabic tweets in order to make the data more useful and understandable. A set of classification algorithms has been used in this system, such as SVM, MNB, RF, VC and DT in both Weka and Python with different test sizes (0.1, 0.2, 0.3, 0.4 and 0.5). These algorithms' results are compared in terms of accuracy, precision, recall, and f1-scoe metrics. Figure 1 shows the proposed system design.

IV.1. Collect Dataset

It is difficult to collect data in social media since its language is informal, irregular, unstructured and multilingual [5].

The data have been taken from Twitter and to get that data, it is fundamental to have a Twitter account that allows accessing the Twitter application manager and creating a key that has been treated with the Java code that includes twitter 4J library. The code collected all the reviews by using keywords such as" ليصنت مديج "يداروا ثامة والأواثار المجاوية والمادة والمادة

These tweets have been saved in excel format with their classification label.

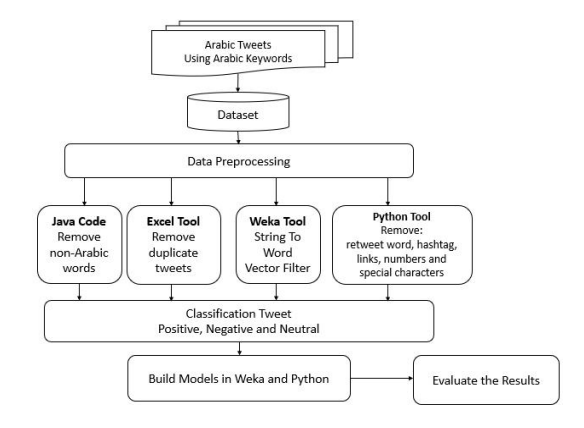


Fig. 1. Methodology Architecture

Copyright © 2020 Praise Worthy Prize S.r.l. - All rights reserved

However, the YouTube and Twitter tweets have not been clean because there have been many reviews that are not related to this research. Therefore, only 7065 reviews out of 9573 tweets have been useful.

IV.2. Labelling Dataset

Each review in the dataset has been categorized manually into one of three classes; positive, negative or neutral.

The number of each category is shown in Fig. 2.

- Positive review: Any customer review that supports online shopping services from all the aspects, or shows a good experiment with online shopping, has been expressed by 1. The number of the positive examples is 3581 tweets. An example of this category نصخ سبك مذقي ىي رجته ضيفخت تبسب 10 اجدته عيوج بلع ":is
- Negative review: Any customer review that does not support online shopping and prefers shopping in the store, or shows a bad experiment with online shopping has been expressed by 0. The number of the negative examples is 493 tweets. An example of this اسـولارأ نقط قسلا يف دييسـولا هيـواز هكـي " :category is :"ثاعبطب
- Neutral review: It is not a positive or a negative review; it is an advice or a question. It has been expressed by 2. The number of the neutral examples is 2990 tweets. An example of this category is: " هود ريبك لا كفس د خصب ك لاب لغشت لا ظنفد ه ."نهًاكه بلأ

IV.3. Preprocessing Steps

After collecting the data, they have been preprocessed since they have not been clean and have contained many useless or not understandable things [11]. In this paper, the pre-processing has been done in two steps. The first one is using Java code and Excel tool in order to remove the tweets duplicates and to remove anything in the dataset except Arabic words. The second step has been done in Weka tool [12] and python. In Weka, each

word in the text has been converted into a vector using StringToWordVector filter [13], [14].

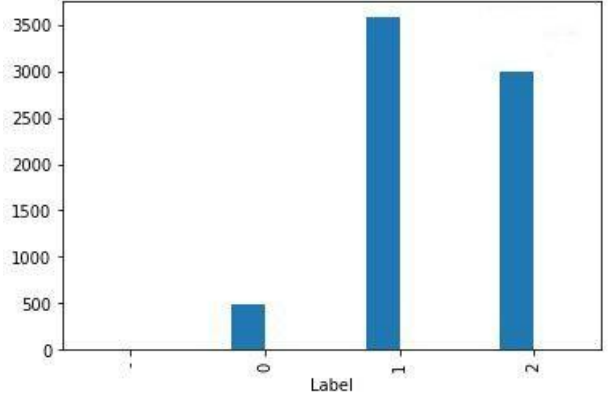


Fig. 2. Number of each category in dataset

Copyright © 2020 Praise Worthy Prize S.r.l. - All rights reserved

In Python, the retweet word (RT), twitter user mentions, hashtags, links, special chars, and numbers have been removed. The preprocessing in Weka is implemented using StringToWordVector filter. The aim of this filter is to transform the text word to numeric values that represent the frequency of the words in the text [13], [14], and contains many techniques, such as:

- The tokenization means to divide the text into set of words based on space and it is applied using many algorithms, such as WordTokenizer [15], [16] that is found in this filter;
- The stop words list means that set of words that occur frequently, not useful and it is applied using many algorithms, such as Rainbow technique. [15], [16] that is found in this filter;
- The stemming means to return the word to the base and it is applied using many algorithms, such as snowball stemmers [15], [16] that are found in this filter.

IV.4. Extract Features

After preprocessing process, the features have been extracted and fed into all the machine-learning algorithms. Because the machine learning algorithms cannot deal with the text directly, it should be converted to numbers using different techniques. In this paper, a CountVectorizer technique in Python has been used. It counts the word in each tweet in dataset, so the algorithms can deal with the text based on the count of each word in each tweet or sentence [17].

IV.5. Classification Algorithms

Classification is one of the most important steps in text mining algorithms, machine learning and natural language processing (NLP) [18]. In addition, it is used in different applications and tools in many fields such as marketing, and online shopping... etc. Its goal is to make the predefined classes ready for a text document [18].

Text classification can be done in two steps: the first one is building a machine-learning model (classifier model). This step can be accomplished after the dataset preparation, which is named as a training dataset that contains a set of reviews and every comment related to a specific label [18]. The second step is testing the dataset.

This one is accomplished by testing the classifier model that has been built previously based on an unseen dataset. Many of the classification algorithms can be applied by using several software tools that are online sources and can be easily downloaded such as WEKA, and Python.

In this paper, many of the classification algorithms implemented in WEKA and Python tools with test sizes (0.1, 0.2, 0.3, 0.4 and 0.5) have been used, such as Multinomial Naïve Bayes (NB), voting classifier, Support Vector Machine (SVM), Decision Tree (DT) and random forest. Next, there is a detailed explanation for each one of these algorithms:

- MNB classifier: The most widely commonly used to build a sentiment analysis model is Naïve Bayes with different types. In this paper, Multinomial NB has been used. MNB is a supervised method that needs to have a learning dataset before starting to work. It is also considered as a simple probabilistic algorithm since it is designed based on the Bayesian probability method [19]. This type of NB deals with the discrete values not numerical values like sport, social or economic categories and valid or invalid categories [19]-[21]. For sentiment analysis application, the method has been first used to determine the probability of a word appearance in a document. Then, the classifier has been built to classify the tweets based on its relevance, appropriate labelling [19]-[21]. In this paper, the parameters in Python are alpha with value 1.0, fit prior with True and class prior (number of class) with None. In Weka, the parameters are batch size equal to 100 and numDecimalPlaces equal to 2;
- DT classifier: A decision tree is a flowchart tree structure. Every inner node (non-leaf node) represents a test on an attribute, each branch in the tree represents a result of the test, and every leaf node represents a class label [22]-[24]. Given a record X, where the related class label is anonymous, the attribute values of the record are tested against the decision tree. The path is traced from the root to the leaf node, which holds the class prediction for that record. Then decision trees can be easily converted to classification rules [23]-[25]. In this paper, the parameters in Python are criterion is gini index, splitter is best and the min_samples_split is equal to 2. In Weka, the parameters type is J48, and the batch size is equal to 100;
- SVM classifier: The SVM is a kind of supervised machine-learning algorithm, which means that the class label is known. It is widely used in problems that relate to the linear and the nonlinear data classification [24], [26]-[28], [34], [35]. The SVM works as the follows. It represents the points from dataset in space and tries to find and search the longest distance hyperplane that separates the data into two classes. The longest distance is called Maximum Marginal Hyperplane (MMH) [24], [26]-[28]. In this paper, the parameters in Python have the kernel type of linear, and the probability is equal to True. In Weka, the parameters have kernel type of polykernel with exponent equal to 1, and the batch size is equal to 100;
- RF classifier: RF is a type of machine learning algorithm in which the class label is known to each object in the dataset. The ensemble classifier is a classifier that combines multi-classifier in it in order to enhance the overall accuracy [29]. The RF is ensemble classifier that combines decision tree algorithm. The pros of RF are not sensitive to the overfitting that the decision tree algorithm is produced and it can handle a massive dimensionality

- of data [29], [30]. In this paper, the parameters in Python are the n_estimators equal to 100, the criterion is gini index and the min_samples_split is equal to 2. In Weka, numIterations are 100, bagSizePercent is equal to 100 and the batch size is equal to 100;
- VC classifier: The Voting classifier is an ensemble classifier that is used to improve the accuracy of the prediction process [31], [32]. The base classifiers that are included in it can be the same type or combined between several types, such as MNB, DT, RF, and SVM in same time [31]. The basic concept of the voting classifier is each base classifier predicting the test dataset, and the Voting taking the prediction of each classifier by using the majority voting the discrete label or average technique for the continuous label based on the class label type [31], [32]. In this paper, four classifiers have been implemented. They have been used combining between them in Weka tool and Python in the voting classifier. The parameters in Python are: voting type is hard type and the base classifier is combined the RF, NB, DT, and SVM. The parameters of this classifier in Weka are: base classifier is combined the RF, NB, DT, and SVM, combinationRule: Majority Voting and the batch size is equal 100.

V. Results and Discussion

In this paper, the system has used 7065 Arabic YouTube and twitter customer reviews regarding online shopping. Firstly, the preprocessing on the dataset has been applied in different tools like Java, Excel, Weka and Python. Many classifiers were applied, such as SVM, NB, RF, DT and voting classifier. After that, the models have been checked by using a Hold-out technique that has been implemented in Weka and Python tools in order to split the data into training and testing based on several sizes that are 0.1, 0.2, 0.3, 0.4 and 0.5. In the next part, it will be shown in detail how every classifier has performed when it has been applied to the dataset. Different metrics have been considered in order to evaluate the results, which are accuracy, precision, f1score and recall. These metrics results have been calculated based on the below equations [33]:

$$Accuracy = (TP + TN)/(TP + TN + FP + FN)$$
 (1)

$$Precision = TP / (TP + FP)$$
 (2)

$$Recall = TP / (TP + FN)$$
 (3)

$$F1-score = \frac{(2 \times Precision \times Recall)}{(Precision + Recall)} \tag{4}$$

where TP: True positives; for correctly predicted event values, FP: False positives; for incorrectly predicted

event values, *TN*: True negatives; for correctly predicted no-event values, *FN*: False Negatives; for incorrectly predicted no-event values. Table I and Table II show the results for all the algorithms in different test sizes whether Python or Weka. Based on these tables, the best algorithm is the RF in test size 0.4, which shows an accuracy of 93.7%.

TABLE I

PYTHON RESULTS						
Test size	Metric	SVM	DT	NB	RF	Voting
						classifier
	Accuracy	73.62	93.1	71.4	93.03	86.19
0.1	Precision	75	93	71	93	88
0.1	Recall	74	93	70	93	86
	F1-Score	72	93	69	93	86
	Accuracy	74.92	92.9	71.3	92.97	86.92
0.2	Precision	76	93	71	93	89
0.2	Recall	75	93	71	93	87
	F1-Score	73	93	70	93	87
	Accuracy	74.44	92.8	71.02	93.12	86.67
0.3	Precision	75	93	71	93	89
0.3	Recall	74	93	71	93	87
	F1-Score	72	93	69	93	86
	Accuracy	74.44	93.2	71.97	93.7	86.64
0.4	Precision	75	94	72	94	89
0.4	Recall	74	93	72	94	87
	F1-Score	73	93	70	94	86
	Accuracy	74.91	94.2	71.3	93.54	87.4
0.5	Precision	75	94	71	94	89
0.5	Recall	75	94	71	94	87
	F1-Score	74	94	69	94	87

TABLE II WEKA RESULTS

Test size	Metric	SVM	DT	NB	RF	Voting classifier
	Accuracy	79.89	78.75	76.49	82.29	82.86
0.1	Precision	78.3	78.6	75.9	82.2	82.5
0.1	Recall	79.9	78.8	76.5	82.3	82.9
	F1-Score	78.5	76.7	75.7	80.2	81.1
	Accuracy	80.89	77.49	76.43	81.46	82.52
0.2	Precision	79.3	77.4	75.8	80.5	81.9
0.2	Recall	80.9	77.5	76.4	81.5	82.5
	F1-Score	79.5	75.7	75.7	79.6	80.9
	Accuracy	79.6	77.3	76.69	81.1	82.11
0.3	Precision	78.2	77.8	75.8	79.9	81.6
0.3	Recall	79.6	77.3	76.7	81.	82.1
	F1-Score	78.3	75.3	75.9	79.1	80.4
	Accuracy	80.25	76.5	76.68	81.56	82.20
0.4	Precision	79.3	76.6	76	80.7	82.2
0.4	Recall	80.3	76.5	76.7	81.6	82.2
	F1-Score	79.2	74.3	75.8	79.6	80.6
	Accuracy	80.5	76.36	75.68	80.92	82.13
0.5	Precision	79.5	78.1	75	79.9	81.9
0.3	Recall	80.5	76.4	75.7	80.9	82.1
	F1-Score	79.4	74.9	74.7	79	80.5

VI. Conclusion

In this paper, the influencing factors on consumers of online shopping and media technology in the Arab world have been analyzed using Arabic tweets. Then, several classification algorithms, such as SVM, MNB, RF, VC and DT in Python and Weka were used. The collected data from YouTube and twitter reviews have been categorized into three classes; Positive expressed as 1, Negative expressed as 0 and neutral expressed as 2. After

preprocessing, these algorithms have been applied on the dataset. The results have shown that the Random Forest algorithm in the Python has achieved the best accuracy with 93.7% in 0.4 test size when compared to other classifiers. However, the VC has given the best results in Weka tool with 82.86 % accuracy in 0.1 test size.

Therefore, the random forest is the best algorithm whether in Weka or Python and in different test sizes.

Finally, the most affective factors on online shopping in the Arab World have been found to be trust in online shopping, non-delivery risk, financial risk, and how people look to online shopping. Therefore, the stakeholders should assure consumers about the delivery of their products and make their websites safer. The results show that around 51% of users has said that online shopping is better than the traditional one and around 49% has said that traditional shopping is better than the online shopping, which is based on tweets in dataset. In future work, the dataset size will be increased and more machine-learning algorithms in addition to deep learning algorithms will be applied. In addition, natural language processing tool, such as Madamira, has been used to extract features like part of speech tagging and named entity recognition.

References

- [1] M. H. Moshrefjavadi, H. R. Dolatabadi, M. Nourbakhsh, A. Poursaeedi, A. Asadollahi, An Analysis of Factors Affecting on Online Shopping Behavior of Consumers, *International Journal of Marketing Studies*, Volume 4, (Issue 5), October 2012.
- [2] P. Chandra and J. Chen, Taming the Amazon, Proceedings of the Tenth International Conference on Information and Communication Technologies and Development - ICTDX 19, 2019
- [3] R. A. E.-D. Ahmeda, M. E. Shehaba, S. Morsya, N. Mekawiea, Performance Study of Classification Algorithms for Consumer Online Shopping Attitudes and Behavior Using Data Mining, 2015 Fifth International Conference on Communication Systems and Network Technologies, 2015.
- [4] Y.-P. Chiu, S.-K. Lo, A.-Y. Hsieh, and Y. Hwang, Exploring why people spend more time shopping online than in offline stores, *Computers in Human Behavior*, Volume 95, 2019, Pages 24–30.
- [5] A. Kumar, M. Saini, P. Hans, Factors influencing online shopping behavior of university students, *International Journal of System Assurance Engineering and Management*, Volume 10, (Issue 4), September 2019, *Pages* 861–865.
- [6] P. Jiang, D. B. Jones, An Exploratory Study of Factors Affecting Consumer International Online Shopping Behavior, *Encyclopedia of E-Commerce Development, Implementation, and Management*, 2016, Pages 1627–1642.
- [7] Y. J. Lim, A. Osman, S. N. Salahuddin, A. R. Romle, S. Abdullah, Factors Influencing Online Shopping Behavior: The Mediating Role of Purchase Intention, *Procedia Economics and Finance*, Volume 35, 2016, Pages 401–410.
- [8] T. M. Nisar, G. Prabhakar, What factors determine e-satisfaction and consumer spending in e-commerce retailing?, *Journal of Retailing and Consumer Services*, Volume 9, 2017, Pages 135– 144
- [9] T. P. Y. Monsuwé, B. G. Dellaert, and K. D. Ruyter, What drives consumers to shop online? A literature review, International Journal of Service Industry Management, Volume 15, (Issue 1), 2004, Pages 102–121.
- [10] M. Chang, W. Cheung, and V. Lai, Literature derived reference models for the adoption of online shopping, *Information & Management*, Volume 42, (Issue 4), 2005, Pages. 543–559.
- [11] A. Ayedh, G. TAN, K. Alwesabi and H. Rajeh, The Effect of

Copyright © 2020 Praise Worthy Prize S.r.l. - All rights reserved

- Preprocessing on Arabic Document Categorization, *Algorithms*, Volume 9, (Issue 2), 2016, Pages 1-27.
- [12] https://www.cs.waikato.ac.nz/ml/weka/.
- [13] Umadevi, Sentiment Analysis Using Weka, *International Journal of Engineering Trends and Technology (IJETT)*, Volume 18, (Issue 4), 2014, Pages 181-183.
- [14] P. Han, D. Wang, Q. Zhao, The research on Chinese document clustering based on WEKA, 2011 International Conference on Machine Learning and Cybernetics, 2011.
- [15] Saravanan, R.A., Rajesh Babu, M. Enhanced text mining approach based on ontology for clustering research project selection. *J Ambient Intell Human Comput* (2017). doi: https://doi.org/10.1007/s12652-017-0637-7
- [16] https://wekatutorial.com/.
- [17] A. Kulkarni and A. Shivananda, Converting Text to Features, Natural Language Processing Recipes, 2019, Pages 67-96.
- [18] M. Allahyari, S, Pouriyeh, M. Assefi, S. Safaei, E. D. Trippe, J. B. Gutierrez, K. Kochut, A Brief Survey of Text Mining: Classification, Clustering and Extraction Techniques, arXiv:1707.02919 [cs], July 2017.
- [19] R. Al-khurayji, A. Sameh, An Effective Arabic Text Classification Approach Based on Kernel Naive Bayes Classifier, *International Journal of Artificial Intelligence & Applications*, Volume 8, (Issue 6), 2017, Pages 01-10.
- [20] S. Bachhety, S. Dhingra, R. Jain, N. Jain, Improved Multinomial Naïve Bayes Approach for Sentiment Analysis on Social Media, Social Science Research Network, Rochester, NY, SSRN Scholarly Paper ID 3363601, 2018.
- [21] A. A. Farisi, Y. Sibaroni, S. A. Faraby, Sentiment analysis on hotel reviews using Multinomial Naïve Bayes classifier, *J. Phys.: Conf. Ser.*, Volume 1192, 2019.
- [22] G. Tsoumakas, I. Katakis, Multi-Label Classification, International Journal of Data Warehousing and Mining, Volume 3, (Issue 4), 2007, Pages 1-13.
- [23] Y. K. Qawqzeh, M. M. Otoom, F. Al-Fayez, I. Almarashdeh, G. Jaradat, A Proposed Decision Tree Classifier for Atherosclerosis Prediction and Classification, *International Journal of Computer Science and Network Security*, Volume 19, (Issue 12), 2019.
- [24] S. Sahoo, A. Subudhi, M. Dash, S. Sabut, Automatic Classification of Cardiac Arrhythmias Based on Hybrid Features and Decision Tree Algorithm, *IJAC*, Volume 17, (Issue 2), 2020, Pages 1-11.
- [25] R. Duwairi, R. Marji, N. Sha'ban, S. Rushaidat, Sentiment Analysis in Arabic tweets, 2014 5th International Conference on Information and Communication Systems (ICICS), 2014.
- [26] S. Tong, D. Koller, Support Vector Machine Active Learning with Applications to Text Classification, JMLR, 2001, Pages 45-66.
- [27] D. Sculley, G. Wachman, Relaxed online SVMs for spam filtering, Proceedings of the 30th annual international ACM SIGIR conference on Research and development in information retrieval - SIGIR '07, 2007.
- [28] R. D. Howsalya Devi, A. Bai, N. Nagarajan, A novel hybrid approach for diagnosing diabetes mellitus using farthest first and support vector machine algorithms, *Obesity Medicine*, Volume 17, 2020.
- [29] M. Pal, Random forest classifier for remote sensing classification, International *Journal of Remote Sensing* Volume 26, (Issue 1), 2005, Pages 217-222.
- [30] N. Arora, P. D. Kaur, A Bolasso based consistent feature selection enabled random forest classification algorithm: An application to credit risk assessment, *Applied Soft Computing*, Volume 86, 2020.
- [31] J. Matoušek and D. Tihelka, Glottal Closure Instant Detection from Speech Signal Using Voting Classifier and Recursive Feature Elimination, *Interspeech* 2018, 2018.
- [32] D. Mungra, A. Agrawal, and A. Thakkar, A Voting-Based Sentiment Classification Model, in *Intelligent Communication*, Control and Devices, Singapore, 2020, Pages 551–558.
- [33] B. Chen, X. Chen and W. Xing, "Twitter Archeology" of learning analytics and knowledge conferences, Proceedings of the Fifth International Conference on Learning Analytics And Knowledge -LAK '15, 2015.
- [34] Moloi, K., Jordaan, J., Hamam, Y., The Development of a High Impedance Fault Diagnostic Scheme on Power Distribution Network, (2020) International Review of Electrical Engineering

- (IREE), 15 (1), pp. 69-79. doi: https://doi.org/10.15866/iree.v15i1.17074
- [35] Marrugo Cardenas, N., Amaya Hurtado, D., Ramos Sandoval, O., Comparison of Multi-Class Methods of Features Extraction and Classification to Recognize EEGs Related with the Imagination of Two Vowels, (2018) International Journal on Communications Antenna and Propagation (IRECAP), 8 (5), pp. 398-405. doi: https://doi.org/10.15866/irecap.v8i5.12709

Authors' information

Jordan University of Science and Technology.



Professor Muneer Masadeh Bani Yassein received his PhD degrees in Computer Science from the University of Glasgow, U.K., in 2007, He is currently professor in the Department of Computer science at Jordan University of Science and Technology (JUST), Muneer served as Chairman of the department of Computer science from 2008 to 2010, as Vice Dean of the

Faculty of Computer and Information Technology from 2010 to 2012, 2013-2014 and 2018 to present. Muneer is currently conducting research in Mobile Ad hoc Networks, Wireless sensors Networks, Cloud Computing, simulation and modelling, Internet of Things, Bani Yassein has published over 170 technical papers in well reputed international journals and conferences. During his career, he has supervised more than 70 graduate and undergraduate students. Professor Bani Yassein is member of IEEE and he is a member of the technical programs of several journals and conferences.



Omar Osama Alomari received his bachelor degrees in Computer Information Systems from the Jordan University of science and technology (JUST), Jordan, in 2016, He is currently MSc. student in the department of Computer science at (JUST).

International Journal on Communications Antenna and Propagation (IRECAP)

Aims and scope

The *International Journal on Communications Antenna and Propagation (IRECAP)* is a peer-reviewed journal that publishes original theoretical and applied papers on all aspects of Communications, Antenna, Propagation and networking technologies. The topics to be covered include but are not limited to:

Communications and Information theory, multimedia signal processing, communication QoS and performance modelling, cross-layer design and optimization, communication software and services, protocol and algorithms for communications, communication network security, cognitive radio communications and networking, hardware architecture for communications and networking, emerging communication technology and standards, communications layers, internet protocols, internet telephony and VoIP, fading channel, mobile systems, services and applications, indoor communications and WLAN; superhighways, interworking and broadband VPN, spread spectrum communication.

Wireless communications and networking, coding for wireless systems, multiuser and multiple access schemes, mobile and portable communications systems, real-time transmission over wireless channels, optical wireless communications, resource allocation over wireless networks, security, authentication, and cryptography for wireless networks, signal processing techniques and tools, wireless traffic and routing, ultra wide-band systems, wireless sensor networks, wireless system architectures and applications, wireless ad-hoc and sensor networking, cooperative communications and networking, bio-inspired wireless communications systems, broadband wireless access, broadband networking and protocols, internet services, systems and applications, P2P communications and networking, satellite and space communications, vehicular networks, emerging wireless communication technology and standards.

Antenna analysis and design, antenna measurement control and testing, smart reconfigurable and adaptive antennas and multiple antenna systems for spatial, polarization, pattern and other diversity applications, novel materials for enhanced performance,

Propagation, interaction of electromagnetic waves with discrete and continuous media, radio astronomy and propagation and radiation aspects of terrestrial and spacebased communications, theoretical and computational methods of predicting propagation and sensing, propagation and sensing measurements in all media, interaction of electromagnetic waves with biological tissue, characterization of propagation media and applications of propagation, multipath interference, channel modeling and propagation.

Instructions for submitting a paper

The journal publishes invited tutorials or critical reviews; original scientific research papers (regular papers), letters to the Editor and research notes which should also be original presenting proposals for a new research, reporting on research in progress or discussing the latest scientific results in advanced fields; short communications and discussions, book reviews, reports from meetings and special issues describing research on all aspects of Communications, Antenna, Propagation and networking technologies.

All papers will be subjected to a fast editorial process.

Any paper will be published within two months from the submitted date, if it has been accepted.

Papers must be correctly formatted, in order to be published.

An Author guidelines template file can be found at the following web address:

www.praiseworthyprize.org/jsm/?journal=irecap

Manuscripts should be sent on-line or via e-mail as attachment in .doc and .pdf formats to:

editorialstaff@praiseworthyprize.com

Abstracting and Indexing Information:

Academic Search Complete - EBSCO Information Services Cambridge Scientific Abstracts - CSA/CIG Elsevier Bibliographic Database SCOPUS Index Copernicus - IC Journal Master List 2018: ICV 122.62

Autorizzazione del Tribunale di Napoli n. 17 del 22/03/2011

Praise Worthy Prize

